L-Università ta' Malta
Faculty of Engineering

MASTER OF SCIENCE IN ENGINEERING DISSERTATION

Characterisation of Hydrogen Engine Combustion and Mitigation of Knock in Dual-Fuel Operations

ANDREW FENECH

Supervised by:

PROF. ING. MARIO FARRUGIA

Co-supervised by:

DR. KENNETH SCERRI AND DR. JEAN-PAUL MOLLICONE

A dissertation submitted in partial fulfilment of the requirements for the degree of Master of Science in Engineering

by the

Faculty of Engineering

October 2025

L-Università ta' Malta

FACULTY/INSTITUTE/CENTRE/SCHOOL Faculty of Engineering

DECLARATIONS BY POSTGRADUATE STUDENTS

(a) Authenticity of Dissertation

I hereby declare that I am the legitimate author of this Dissertation and that it is my original work.

No portion of this work has been submitted in support of an application for another degree or qualification of this or any other university or institution of higher education.

I hold the University of Malta harmless against any third party claims with regard to copyright violation, breach of confidentiality, defamation and any other third party right infringement.

(b) Research Code of Practice and Ethics Review Procedures

I declare that I have abided by the University's Research Ethics Review Procedures. Research Ethics & Data Protection form code ENG-2025-00012.

As a Master's student, as per Regulation 77 of the General Regulations for University Postgraduate Awards 2021, I accept that should my dissertation be awarded a Grade A, it will be made publicly available on the University of Malta Institutional Repository.

Copyright Notice

GOVERNMENT
OF MALTA

The research work disclosed in this publication is partially funded by the Endeavour II Scholarships Scheme. The project is co-funded by the ESF+ 2021-2027

Co-funded by
the European Union

To my beloved parents

Abstract

Over the past decades, significant efforts have been focused on reducing fossil fuel dependency by promoting sustainable energy sources. Recently, major corporations have shifted their attention to H_2 as a fuel for internal combustion engines, as the development of H_2 fuel cells has not progressed as rapidly as expected. H_2, with its higher calorific value and carbon-free molecular composition, offers a promising clean fuel alternative. However, the limited H_2 infrastructure necessitates the continued development of dual-fuel combustion. This dissertation focuses on H_2 combustion characterisation and improving the performance of existing dual-fuel engines by leveraging the thermodynamic properties of fuels.

H_2 combustion characterisation was performed utilising in-cylinder pressure measurements obtained through experimental testing. These in-cylinder pressure measurements were processed using LabVIEW software to analyse key combustion parameters such as the rate of heat release and combustion duration. These parameters were subsequently compared to those obtained from conventional fuels. Accurate determination of the air-fuel ratio during lean operation is critical. This was achieved through simultaneous and separate measurements of fuel and airflow rates. To address the pulsating airflow, a critical flow orifice was designed and incorporated into the setup based on choked flow theory, which depends solely on upstream conditions. The major highlight of this combustion characterisation investigation is the high brake thermal efficiency of 23% achieved by H_2 under $\lambda 3$ mixture, compared to the 21% obtained with stoichiometric petrol testing at wide open throttle.

A cryogenic setup was developed specifically for liquid natural gas injection to enhance combustion and mitigate engine knock in dual-fuel engines. However, due to safety constraints, experimentation with liquid natural gas was substituted with injections of liquid nitrogen and liquid propane. This approach aims to reduce intake air temperatures, thereby mitigating engine knock. Temperature measurements during liquid nitrogen injection revealed a reduction of approximately 45 °C at a 60% substitution ratio with vapour propane. Liquid propane injection resulted in temperature reductions of 4 °C and 7 °C at 60% and 70% substitution ratios, respectively. Across all substitution ratios and intake conditions tested, the use of liquid dual-fuel injection consistently decreased the maximum amplitude of pressure oscillations, indicating improved knock resistance.

Acknowledgments

I am truly grateful to all individuals who have supported and contributed to the successful completion of my project and thesis.

First and foremost, I wish to express my sincere appreciation to my supervisor, Prof. Ing. Mario Farrugia, for his consistent guidance and invaluable advice throughout this journey. His extensive expertise and enthusiasm in the field have been instrumental in achieving the objectives of this dissertation and expanding my understanding of diverse engineering concepts. The insightful discussions and constructive feedback provided by Prof. Farrugia will undoubtedly remain influential in both my personal growth and professional engineering development.

Further thanks go to Dr. Kenneth Scerri and Dr. Jean Paul Mollicone for their invaluable support throughout this project. Their assistance during consultations, constructive feedback and guidance in addressing writing challenges were instrumental in refining my work.

Additionally, I would like to express my sincere appreciation to all the staff in the engineering department, with particular thanks to Mr. Andrew Briffa, the Thermodynamics Laboratory Technician, for his invaluable assistance with engine testing and practical support throughout this dissertation. The in-depth discussions and guidance he provided on project-related matters and other engineering tasks are greatly appreciated and will be fondly remembered.

I also wish to extend my sincere gratitude to the Systems Engineer, Ing. Jean Paul Azzopardi for his assistance and encouragement throughout the course of this thesis.

The funding of this dissertation was partially provided through project Liquid State Dual fuel injection (LSDi), which is financed by Xjenza Malta through the FUSION: R&I Research Excellence Program and the Endeavour II Scholarship program.

Last but not least, I am deeply thankful to my family, loved ones, and close friends. Their constant support and encouragement have helped me reach this important milestone in my engineering studies. Their advice and motivation have meant a great deal to me throughout this journey.

Table of Content

List of Figures

List of Tables

Nomenclature

ABDC	After Bottom Dead Centre
AFR	Air Fuel Ratio
ATDC	After Top Dead Centre
BDC	Bottom Dead Centre
BTDC	Before Top Dead Centre
CA	Crank Angle
CC	Cubic Centimetre
CI	Compression Ignition
CNG	Compressed Natural Gas
COV	Coefficient Of Variation
CR	Compression Ratio
DFE	Dual-Fuel Engine
DI	Direct Injection
DOI	Duration Of Injection
ECU	Engine Control Unit
EOC	End Of Combustion
FMEP	Friction Mean Effective Pressure
GDI	Gasoline Direct Injection
HHV	High Heating Value
HRR	Heat Release Rate
ISO	International Organisation of Standardisation
LFE	Laminar Flow Element
LHV	Lower Heating Value

LSDi	Liquid State Dual injection
MAF	Mass Airflow
MAP	Manifold Absolute Pressure
MAPO	Maximum Amplitude Pressure Oscillation
MBT	Maximum Brake Torque
MFB	Mass Fraction Burned
NOx	Nitrogen Oxides
PFI	Port Fuel Injection
RON	Research Octane Number
RPM	Revolutions Per Minute
SI	Spark Ignition
SOC	Start Of Combustion
SOI	Start Of Injection
SR	Substitution Ratio
TDC	Top Dead Centre

Glossary of Symbols

a	Crank radius	m
A	Area	m^2
c_p	Specific heat capacity at constant pressure	J/(kg·K)
c_v	Specific heat capacity at constant volume	J/(kg·K)
c_x	The coefficient variable	/
d	Diameter	m
F	Friction	N
h	Enthalpy	J
H	Calorific value	J/kg
k	Heat transfer coefficient	W/(m²·K)
L	Connecting rod	m
m	Mass	kg
n	Polytropic index	/
p	Pressure	Pa
q''	Heat flux	W/m^2
S	Speed	m/s
T	Temperature	K
V	Volume	m^3
W	Work	J
w	Velocity	m/s
x_B	The bore of a variable	/
x_b	The blow-by gases of a variable	/
x_c	The compression effect of a variable	/
x_{cyl}	The cylinder of a variable	/

x_D	The drag of a variable	/
x_f	The final state of a variable	/
x_h	The heat transfer coefficient effect on a variable	/
x_i	The initial state of a variable	/
x_0	The initial state of a variable	/
x_p	The piston of a variable	/
x_r	The reference of a variable	/
x_s	The displacement of a variable	/
x_t	The throat variable	/
x_{tf}	The state at the end of combustion of a variable	/
x_{ti}	The state during ignition of a variable	/
x’	The combustion effect on a variable	/
x’’	The combined effect of combustion and heat loss of a variable	/
$\dot{x}$	The time derivative of a variable	/
τ	Torque	Nm
$\emptyset$	Equivalence Ratio $\left(\frac{Stoichiometric\ AFR}{actual\ AFR}\right)$	/
λ	Lambda $\left(\frac{Actual\ AFR}{Stoichiometric\ AFR}\right)$	/
ρ	Density	kg/m^3

Chapter 1. Introduction

1.1 Clean Mobility and Climate Change

Nearly 14 million new electric cars were registered globally in 2023, bringing their total number on the roads to 40 million [1]. Electric car sales in 2023 exceeded 2022 figures by 3.5 million, marking a 35% year-on-year increase. Such sales are 6 times higher than that found in 2018, just five years prior. In 2023, over 250,000 new electric vehicles were registered each week, surpassing the entire annual total from 2013, a decade earlier [1]. During this transitional period, hybrid vehicles have been instrumental in the automotive industry by combining traditional internal combustion engine technology with emerging electric propulsion systems. This integration not only served to familiarise consumers with the new developing technology but also provided the assurance of conventional powertrain reliability through the use of traditional fuels simultaneously [2]. Furthermore, hybrids address concerns about limited electric vehicle infrastructure, especially in developing markets, ensuring that drivers are not left stranded during the ongoing expansion of charging networks.

Despite such rapid growth in electric car sales worldwide, companies are still investing in alternative technologies to promote zero emission transportation by utilising the lightest, most basic and commonly found element in the universe, hydrogen (H_2). However, H_2 is not a primary energy source, meaning it must be produced from other energy sources. Therefore, its production is dependent upon various energy inputs, including renewable sources (green H_2) and non-renewable sources (blue and grey H_2). This is due to the fact that H_2 does not naturally exist in nature in usable form and must be extracted or produced through various methods [3]. The giant automotive companies BMW and Toyota have been collaborating since 2013 on fuel cell drive systems and Toyota have provided the individual fuel cells for the iX5 H_2 vehicles which is planned to be launched in 2028 [4]. Although H_2 technology is presently being accelerated due to multiple companies of various industry sectors and research entities, huge investments still must occur in the infrastructure to support this transition. During this change, one cannot ignore the gravity of climate change effects that are reaching the physical environments, ecosystems and humanity in general. Various scientists are stressing about the current environmental situation and suggest that other alternative available

technologies must be employed immediately to mitigate the negative effects on the environment. An alternative solution is to make use of cleaner fossil fuels such as natural gas. So far in the last century, human development was highly dependent on fossil fuels resulting in large increase in pollution on such a scale that Earth is no longer withstanding causing repercussions. These negative effects are present in multiple forms, mostly predominant in climate change [5].

Presently, there is a 47% likelihood that the global temperature averaged over the entire five-year 2024-2028 period will exceed 1.5°C above the pre-industrial era, according to the World Meteorological Organisation in the Global Annual to Decadal Update [6]. Such likelihood will certainly not be mitigated without large reduction in emissions. Long-lived gases remain in the atmosphere for decades to millennia, whereas short-lived gases and soot persist for less than a year. Given that CO_2 is a long-lived gas [6], emissions released today will contribute to global climate change for centuries, making prompt mitigation essential to avoid costly delays. In contrast, short-lived agents such as sulphur compounds dissipate within a year and thus do not pose the same long-term delay impacts. Therefore, regulating current emissions is vital to effectively mitigate global warming in the coming decades.

1.2 Opportunities for Dual-Fuel Engines

On March 29, 2024, the U.S. Environmental Protection Agency (EPA) issued its final rule [7], "Greenhouse Gas Emissions Standards for Heavy-Duty Vehicles – Phase 3," which establishes stricter emissions standards for heavy-duty vehicles, starting with the 2027 model year. These regulations will apply to a range of heavy-duty vocational vehicles, including delivery trucks, garbage trucks, utility vehicles, buses, and tractors, aiming to significantly cut greenhouse gas emissions. The proposed standards do not require any specific technology, allowing manufacturers flexibility in choosing compatible solutions. EPA expects fleets to incorporate a variety of technologies, such as advanced transmissions, enhanced aerodynamics, improved engines, battery-electric and H_2 fuel cell powertrains. Many of the technologies that were crucial in meeting Phase 2 Greenhouse Gas (GHG) standards are expected to remain important, particularly for reducing emissions in heavy-duty vehicles with internal combustion engines.

Other available strategies that can help reduce emissions and comply with the stated Phase 3 GHG standards include, enhanced exhaust treatment, particulate filters and the use of alternative fuels. Although Compressed Natural Gas (CNG) is not typically categorised as an alternative fuel, it is recognised as a cleaner fuel used across multiple sectors. It is commonly used in various industries specifically in regions with abundant fuel gas resources, such as coal mines or industrial processes that generate waste gases during refining [8].

The economics of converting diesel engines to dual-fuel operation benefit from the combination of affordable fuel and the efficiency, reliability, and widespread availability of diesel engines as prime movers. Most importantly, these engines provide the flexibility to operate solely on diesel fuel, which can be useful in instances where the substitute fuel is scarce or during transitional stages. Similar to the crucial role hybrid vehicles played during the development of electric powertrains, dual-fuel engines are expected to serve as a transitional technology by combining traditional fuels with H_2 until significant advancements in H_2 infrastructure are achieved. Dual-fuel technology has recently gained popularity in the automotive sector, as it was previously more commonly applied in electric power generation and rarely used in smaller engines within the transport sector [8]. In this sector, vehicles which perform routine tasks such as delivery vans and buses, do not usually require high amounts of power but prefer high reliability, low operational costs and low specific-fuel consumption. Additionally, these vehicles have ample space for tank replacement and a setup for centralised refuelling infrastructure [9].

1.3 Current Fuels Used in Dual-Fuel Engines

A study was performed by the International Energy Agency on the emission of gigatonnes of carbon dioxide between the time period of 2019 and 2022 [1]. The corresponding results are shown in Figure 1-1 where the power sector seems to be responsible for the highest production of carbon dioxide. Not long ago, precisely on the 24th April 2017, the 1992 Dellimara 1 plant was switched off and put on cold standby [10]. Simultaneously, on the same day, ElectroGas marked the launch of the new Dellimara 4 gas-fired combined cycle gas turbine plant along with the associated Liquid Natural Gas (LNG) supply and regasification facilities. In addition to the gas turbines,

natural gas is also supplied to eight Wartsila diesel engines located at Malta's power station, comprising of four single-fuel, spark-ignited units and four dual-fuel units [11].

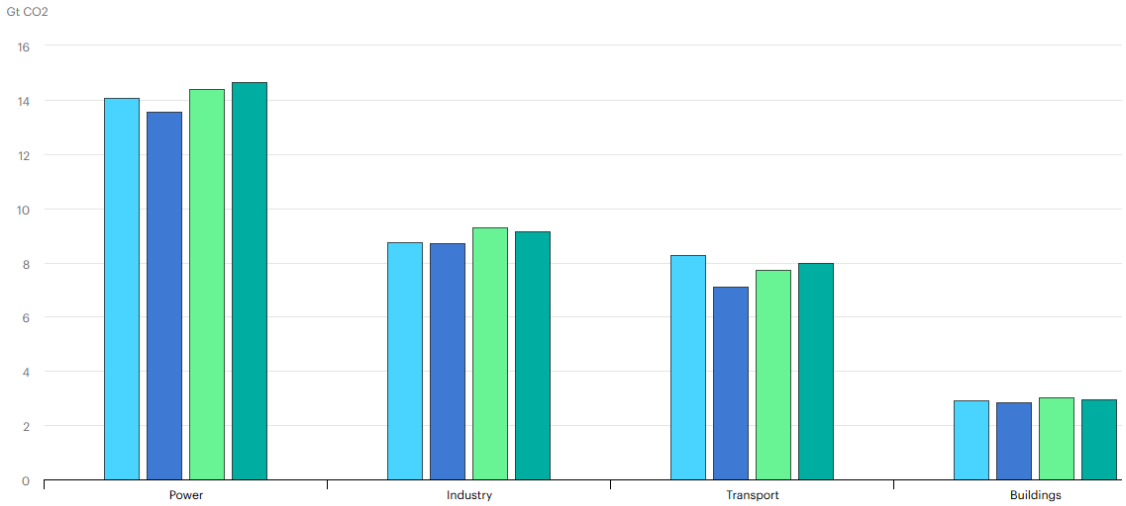

Figure 1-1: Global CO2 emissions by sector, 2019-2022 [1].

Among the candidates of alternative fuels currently, biofuels, Liquefied Petroleum Gas (LPG) and LNG are the potential ones. When compared to biofuels, the availability and economic aspects of LNG and LPG make them more realistic solutions. Although natural gas is derived from fossil sources, it can also be produced from renewable sources such as biomass which is a cost-effective process. Most importantly, through the utilisation of natural gas, engine emissions can be highly controlled in comparison with traditional fuels [12]. However, internal combustion engines can suffer from knock when specific engine parameters such as injection or spark timing are not properly set for certain fuels [13]. This phenomenon can have detrimental effects on engines if not properly mitigated.

When considering the transportation sector, both forms of the natural gas; LNG and CNG were found to be useful. However, due to its lower cost when compared to traditional fuels, CNG gained high popularity in the automobile industry. On the other hand, LNG is mainly used for electricity production and transportation. When compared to CNG, LNG provides higher safety, easier transportation and storage capacity. Additionally, LNG is cleaner than oil and coal, which has led to its widespread recognition in the global market [15]. Hence, LNG is a promising alternative fuel to diesel powered vehicles and is capable to compensate for some severe drawbacks of natural gas-powered vehicles. For instance, a higher range (up to 700-1000 km) is expected from LNG fuelled trucks due to its higher energy density. On the contrary, the

cost of an LNG fuel tank and the engine is approximately double the price of a diesel operated system [16]. However, due to its liquefaction attribute, the volume of LNG reduces by a factor of 600 making it the most preferred mode for transportation. In fact, LNG trade is growing at twice the annual rate of piped natural gas and now represents 10% of global natural gas consumption.

1.4 Dissertation Objectives

With increasing interest in H_2 as a fuel for extending the use of internal combustion engines, investigating H_2 combustion is essential for optimising performance. This H_2 investigation would allow a smoother transition of this fuel in dual-fuel engines. While H_2 can be used as the sole fuel in SI engines, to meet evolving demands (i.e. transitioning to H_2) methane blended with H_2 in dual-fuel engines may be necessary. However, blending H_2 in methane worsens the Wobbe index resulting in higher knock levels. [17] [18] Therefore, in preparation for higher H_2 concentrations in methane gas, knock mitigation through LNG injection was proposed to mitigate knocking in dual-fuel engines. However, for safety reasons procurement of LNG was impossible and instead liquid nitrogen and liquid propane were used.

Research Hypothesis:

Liquid injection (liquid natural gas or liquid propane) in dual-fuel engines can effectively mitigate knock propensity induced by elevated Wobbe index mixtures from H_2-enriched gas grid fuel, while H_2 combustion characteristics provide foundational data for future H_2 integration in dual-fuel systems.

Research Questions:

How does liquid propane injection influence knock intensity and combustion phasing in a dual-fuel diesel-propane engine compared to gaseous propane?

How do H_2 combustion characteristics differ from conventional fuels, particularly regarding the burn duration and efficiency?

This dissertation mainly consists of two separate investigations which were conducted on separate and distinct setups.

The H_2 combustion characterisation was carried out on the J.A.P. 6 single cylinder engine where the main investigations were:

- Enhance the accuracy of the calculated air-to-fuel ratio for the J.A.P. 6 engine during H_2 testing.
- Development of a 0D model to understand the interaction of spark timing with CA50 location
- Perform combustion characterisation analysis through in-cylinder pressure measurements during H_2 operation.

The implementation of the liquid state knock mitigation technique was performed on the existing Peugeot dual-fuel setup. For this setup, the planned investigations were to:

- Develop a cryogenic setup with appropriate apparatus to perform the liquid state knock mitigation technique.
- Install the cryogenic setup onto the dual-fuel setup and test it with Liquid Nitrogen (LN_2).
- Perform dual fuel tests with liquid propane injection and deduce the reduction in knock intensity by calculating the Maximum Amplitude Pressure Oscillation (MAPO) in the measured in-cylinder pressure.

Moreover, although distinct investigations were carried out on separate setups, H_2 combustion characterisation was explored to support its future implementation in dual-fuel engines for enhanced flexibility. Meanwhile, cryogenic liquid injection was investigated as a means to reduce knock which remains a limiting factor in existing dual-fuel engines and must be addressed until H_2 is fully integrated into these systems.

1.5 Dissertation Structure

This dissertation consists of 8 chapters, divided as follows:

- Chapter 1 – The introduction of the dissertation is described, and the aims and objectives are listed accordingly.

- Chapter 2 – The literature review initially explores the opportunities, challenges and research gaps associated with dual-fuel engines. This is followed by an overview of dual-fuel engines, examining different types of fuels. Key operational parameters for both spark and compression ignition engines are identified, with a thorough explanation of the H_2 combustion process. Additionally, the combustion abnormalities and the corresponding solutions are discussed.

- Chapter 3 – Several analytical methods for combustion characterisation were identified, discussed and listed. In some cases, different analytical methods were used simultaneously, and the results obtained were compared accordingly.

- Chapter 4 – The methodology outlining the H_2 experimental procedure is described in detail. All experiments and preliminary work conducted on the J.A.P. 6 engine is systematically presented and explained. Additionally, the test matrix comprising of 12 test points is presented. Finally, the steps involved in the development of the zero-dimensional model are described and its results are discussed.

- Chapter 5 - All the preparations and experimentations done on the Peugeot 2.0 litre dual-fuel setup are detailed in this chapter. Subsequently, the components and configuration of the cryogenic setup for liquid state dual injection are described. Finally, the knock signal is calibrated with the MAPO to enable direct comparison between vapour and liquid propane testing.

- Chapter 6 – This chapter involves the presentation and discussion of the different combustion characteristics obtained from the post processing of in-cylinder

measurements during testing. Comparison with traditional fuels was performed where differences were highlighted and compared to literature.

- Chapter 7 – The significant MAPO results obtained from vapour and liquid propane testing are discussed and compared. Temperature reductions observed during LN_2 and liquid propane injection are compared and analysed. Relative literature is referenced to compare experimental behaviour and results during engine knock operation.

- Chapter 8 – A summary of the results obtained from each investigation is presented, with the corresponding conclusions are highlighted. The significance of the integrated approach adopted in this study is discussed, along with a listing of limitations and suggestions for future work.

The block diagram illustrates how the diesel-propane and H_2 investigations - detailed in the chapters - converge toward the overarching aim of this thesis.

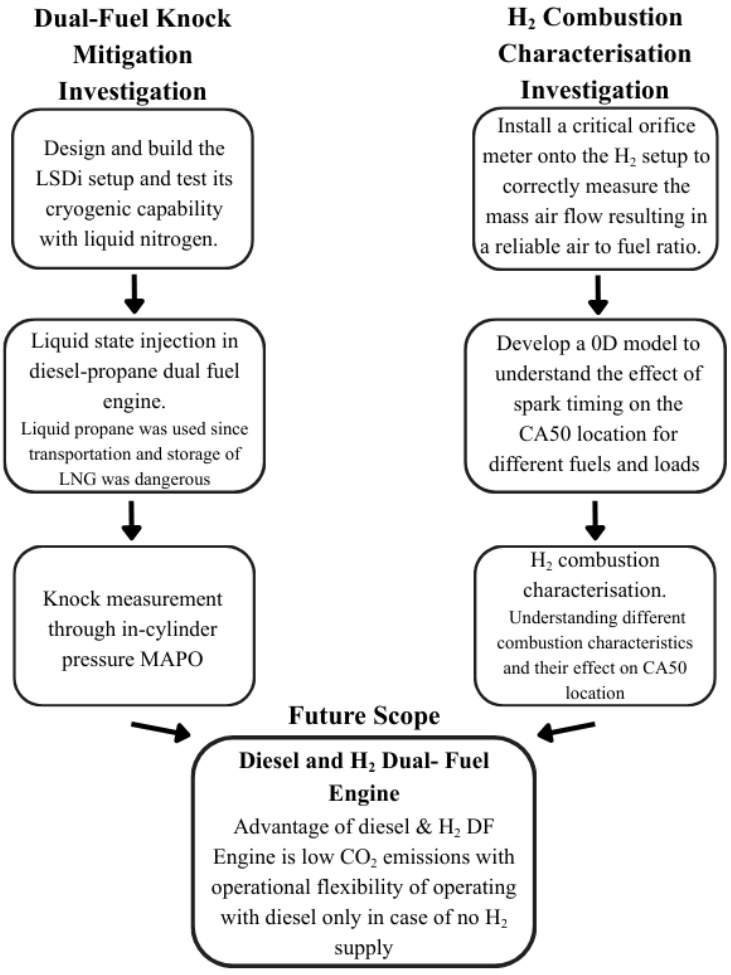

Chapter 2. Literature Review

This literature review primarily aims to provide a concise overview of dual-fuel engine applications to highlight their significance. Given that the two investigations were conducted using different fuels and distinct engine types, the fundamental differences between Spark Ignition (SI) and Compression Ignition (CI) engines are outlined. Subsequently, the combustion process in dual-fuel engines is reviewed, followed by an examination of the drawbacks, particularly knocking, its associated challenges and the existing mitigation strategies. In the context of H_2 combustion, the primary focus was to highlight the importance of proper spark timing for optimum performance in SI engines and to determine the optimal spark timing for H_2-fuelled internal combustion engines. Additionally, other relevant combustion parameters were investigated to enable comparative analysis with the experimental results presented in this dissertation.

2.1 Overview of the Dual-Fuel Engine

A dual-fuel engine is a type of internal combustion engine where the primary fuel, typically natural gas, is mixed homogenously with air in the cylinder, resembling the process in spark-ignition engines [19] while combustion is initiated through a process similar to that of CI engines. Dual-Fuel Engines (DFE) are compatible with a wide range of gaseous fuels including propane, CNG, low BTU wood gas, and H_2 gas as well as LPG [20]. However, unlike a spark-ignition engine, a small quantity of diesel fuel referred to as the pilot, is injected at a point near the Top Dead Centre (TDC) during the compression stroke to initiate combustion [21]. The diesel pilot undergoes rapid pre-flame reactions and ignites due to the heat generated from compression similar to that of a conventional diesel engine, igniting the rest of the air-fuel mixture in the rest of the cylinder. Like the SI engine, the bulk of the energy in a DFE is produced by the combustion of a relatively homogenous preformed mixture of air and the primary fuel in the cylinder [19].

DFEs are rarely equipped with throttles for power control, instead, power output is regulated by adjusting the concentration of natural gas in the premixed charge. Since DFE rely on the CI of a diesel pilot, they share certain characteristics with diesel engines, while also possessing unique advantages and limitations. Despite these distinctions, DFEs more closely resemble diesel engines than spark-ignition engines. Numerous

researchers agree that DFEs achieve optimal performance at moderate-to-high loads, often matching or exceeding the fuel conversion efficiency of pure diesel engines under these conditions [19].

It seems that, to date, there are limited examples of engines especially engineered and developed solely for dual-fuel operation. The conversion of conventional diesel engines to dual-fuel operation requires minimal modifications, significantly lowering capital, operational, and maintenance costs [22]. Additionally, converted diesel engines are capable of retaining their operational lifespan, and in some instances may even outlast conventional diesel engines [23]. The specific energy or fuel consumption is frequently reduced, or at worst, remains comparable to that of a diesel engine under similar load conditions. The engine's power output and speed ranges are largely preserved, closely resembling those of standard diesel operation. Turbocharged DFEs continue to deliver effective power across the entire operational range while maintaining high safety standards. Emissions performance is generally enhanced when compared to diesel engines, particularly in reducing challenging pollutants such as Nitrogen Oxides (NOx) and particulates [8].

A key consideration for converted engines is whether they need to retain the ability to deliver full diesel load output when required, or if they are destined exclusively for dedicated dual-fuel application, with diesel functioning as a temporary backup in the event of a disruption to dual-fuel operation. As a result, conversion kits are typically not designed to be universal or generic. Instead, they are tailored to specific diesel engine models and fuel gas types with a knowledge of the expected operating conditions [8]. During the conversion, the main components and systems altered are the fuel injection system, the fuel gas system and control system [24].

In general, the conversion of a diesel engine to dual-fuel operation should preserve the following key features:

- Major modifications to the engine should be minimised, while still maintaining the ability to operate as a diesel engine. Some reduction in engine output may be necessary [24].

- Peak cylinder pressures should remain within the acceptable limits for diesel operation. Ideally, the size of the liquid fuel pilot should be adjustable relative to the gaseous fuel, depending on factors such as load, speed, and other operating conditions [25].

- The safety of operation with gaseous fuels must remain a top priority, ensuring that the diesel engine can idle safely. Additionally, fail-safe mechanisms and overspeed controls must remain to function properly in the dual-fuel mode [8].

2.2 Fuel Types for Dual-Fuel Engines

The majority of gaseous fuel can be utilised to varying levels of effectiveness in dual-fuel engines. This is primarily achieved by injecting and igniting a sufficient quantity of liquid diesel fuel, which acts as a pilot to initiate combustion. The proportion of fuel energy provided by the gaseous fuel in place of the traditional liquid fuel is referred to as Substitution Ratio (SR). Increasing efforts are focused on maximising the substitution of diesel with more cost-effective gaseous fuels, while maintaining acceptable standards of emissions while not compromising the engine performance. The gaseous fuels suitable for dual-fuel operations include those that are naturally in a gaseous state under ambient conditions. Additionally, the gaseous fuels most in interest are those which have the highest heating value [8]. The use of low heating value fuel mixtures in engines is often less favourable due to the significant additional expenses associated with fuel compression, which is necessary to meet the operational requirements of the engines. Such fuel gases hold significant potential as energy sources, but a substantial portion remains unutilised due to various technical, economic and environmental challenges. Furthermore, dual-fuel operation allows flexibility in the type and composition of gaseous fuel used. It also enables adjustments to the fuel's proportion and injection characteristics, ensuring optimised performance. Table 2-1 [26] shows the relative values of the specific energy storage for a number of common fuels.

*Table 2-1: Lower heating values of different fuels **[26]**.*

Fuels	Lower Heating Value (MJ/kg)
Gasoline	42.4
Diesel fuel	42.5
Methanol	19.7
Ethanol	26.8
Hydrogen (gas)	119.9
Methane	50.0

As seen in Table 2-1, methane which is often the primary component of natural gas, has the second highest calorific value. Natural gas is a mixture of paraffinic hydrocarbons such as methane, ethane, propane and butane [27]. The composition of natural gas varies considerably from source to source which alters its properties [28]. Increased concentrations of higher hydrocarbons enhance the volumetric energy content, while increased levels of inert gases diminish it. However, excessive concentrations of higher hydrocarbons will reduce the Research Octane Number (RON) which may lead to excessive knock. Conversely, large concentrations of inert gases can create excessively lean mixtures, reduce power output and possibly cause rough operation if the mixture is already lean. To address the effects of gas composition on energy delivery, the gas industry has defined a parameter known as the Wobbe number [28]. This index decreases when H_2 is blended with natural gas, which, similarly to the RON, can lead to higher knock levels. Given that there are approximately three million kilometres of natural gas pipelines, blending small amounts of H_2 into the natural gas grid is feasible, thereby reducing the capital costs of H_2 projects [17] [18]. Common examples and fuels derived from natural gas are LPG, CNG, LNG [27]. These fuels often exhibit significant variability in their chemical composition and energy properties, which influences their performance in a dual-fuel system.

2.2.1 LNG comparison with CNG and LPG

CNG and LPG are frequently confused with LNG, though their properties differ significantly, especially under similar temperature and pressure conditions. As the name suggests, CNG primarily consists of methane in its gaseous form, typically comprising 80–90% of the mixture. It is colourless, non-toxic, non-carcinogenic, flammable, and lighter than air. Due to its low energy density, natural gas is compressed to a pressure of 200–250 bar for storage [27]. It is the gaseous by product of petroleum and is the first component separated during the distillation process [29]. The combustion of CNG releases less nitrogen oxide, hydrocarbon, and carbon monoxide emissions compared to diesel. CNG achieves a substantial reduction in particulate emissions compared to diesel, producing significantly less soot [30].

LPG is an abundant, high-octane, clean, and environmentally friendly fuel. It is produced through the fractionation of natural gas and the refining of crude oil. Consisting primarily of propane and butane, LPG remains in a gaseous state under normal atmospheric conditions but can be easily liquefied by applying moderate pressure or reducing the temperature below negative 42°C (i.e. < -42). This property makes the fuel highly versatile and ideal for various applications, as it can be easily condensed, stored, packaged, and used. Upon releasing the pressure, the liquid expands to approximately 250 times its original volume as gas, hence significant amounts of energy can be stored and transported compactly [27].

When natural gas is cooled down to negative 161°C it is converted to LNG [31]. The density of LNG is 435 kg/m³, significantly higher than the 175 kg/m³ of CNG at 200 bar. As a result, an LNG-powered vehicle can travel approximately 1.4 times further than a CNG-powered vehicle with the same fuel tank capacity. However, to match the range of a diesel-powered vehicle, the LNG fuel tank must be approximately 1.7 times larger than the diesel tank [8]. According to a report done by Sutton [32] and a publication by Litzke et al. [33], LNG can directly substitute the diesel fuel for heavy duty vehicle applications and is the most viable option for long range use. The authors emphasised how the amount of LNG stored in cryogenic tanks greatly exceeds that of a CNG system. Due to the cryogenic volume compression of a factor of 600, LNG is highly convenient to transport bulk quantities. Unlike oil spills, LNG would not cause environmental contamination since if spilled on water it would float on top and vaporise

rapidly. LNG, when vaporised would only burn in concentrations of between 5% and 15% mixed in the air [31]. Table 2-2 shows a comparison of physical and chemical properties of LNG with diesel, gasoline and LPG.

*Table 2-2: Comparison of physical and chemical properties of LNG with diesel, gasoline and LPG **[27]**.*

Properties	LNG	Diesel	CNG	LPG
Auto Ignition Point (°C)	540	316	540	454-450
Flash Point (°C)	-187	60	N/A	-104
Boiling Point (°C)	-160	204	-160	-42
Flammable Range (%)	5-15	N/A	5-15	2.1-9.5
Stored Pressure	Atmospheric	Atmospheric	Pressurised	Pressurised

2.2.2 Storage requirements

The primary disadvantage of gaseous fuelled vehicles lies in the weight and bulk of their storage containers. For an equivalent driving range, a CNG storage tank is significantly larger, heavier, and more expensive compared to a gasoline tank. This disparity is due to the need for high-pressure containment, often at 200–250 bar [34], to store CNG efficiently to achieve sufficient energy density for practical driving ranges. When using CNG, vehicle designers must balance driving range, tank cost, available vehicle space, additional weight, and overall fuel cost. The fuel cost itself is influenced by the storage pressure level, with higher pressures typically increasing storage efficiency but also raising costs and complexity. These trade-offs often make CNG more suitable for applications where refuelling infrastructure is readily available and where weight and space constraints are less critical [35]. Several companies [36] [37] are also offering various types of storage vessels varying in sizes and materials to accommodate client needs. The introduced aluminium tanks wrapped with fiberglass or carbon [36] weighs one half to one tenth as much as the conventional steel tanks with only slightly higher costs [35].

From the investigations carried out by DeLuchi et al. [38] between a baseline gasoline vehicle of 35 mpg and a CNG vehicle, the CNG vehicle was 15% more thermally

efficient and 6.5% heavier than the gasoline vehicle. Additionally, it is important to appreciate that the volume of natural gas storage is a function of range and pressure. Moreover, storage volume at 4500 PSI (≈320 bar) uses about 25% less trunk space than storage at 3000 PSI (≈207 bar) [38]. Additionally, the storage volume does not decrease significantly above 4500 PSI due to non-ideal gas behaviour at high pressure [35]. DeLuchi et al. [38] also highlighted the indirect effect of range on acceleration and operating cost due to the additional weight of the storage system, where the authors commented that the doubling of the range typically would result in 5-8% decrease in efficiency and performance.

2.3 Operating Parameters and Advantages of Dual-Fuel Engines

Like other automotive fuels, natural gas generates power in an internal combustion engine through the process of combustion and the subsequent expansion of gases within the combustion chamber. Consequently, engine performance is significantly influenced by both the engine's design and the combustion properties of the fuel used [35]. For dual-fuel engines, the number of operating and design variables is typically greater than those influencing the performance of conventional diesel or SI engines. Consequently, the potential for power generation and the corresponding levels of exhaust emissions in engines operating on various gaseous fuels in dual-fuel mode are largely dependent on how effectively the following design and operational variables are managed [8].

Fuel type- The composition and properties such as its heating value, physical and chemical properties and their corresponding variations with temperature and pressure. The values of the effective flammability limits and burning rates of the fuel are critical especially during the high temperatures and pressures occurring at the end of compression and the onset of the combustion process.

Combustion parameters- The temperatures and pressures of intake and exhaust gases are influenced by the equivalence ratio values utilised. Their corresponding variations impose different knock limits which alter the operating window. One also needs to consider the type of pilot fuel employed, its relative size, timing and injection characteristics.

Exhaust and air intake systems- The volumetric efficiency, turbo charging and the degree of Exhaust Gas Recirculation (EGR) applied.

Engine Design - The engine Compression Ratio (CR), stroke, bore, combustion chamber shape and engine speed range.

The performance of gas-fuelled dual-fuel engines offers several advantages compared to conventional premixed spark-ignition gas engines [8]. Dual-fuel engines can utilise a broader range of gaseous fuels while being less prone to knocking. This is largely due to the use of lean fuel mixtures and controlled pilot ignition, which enhances combustion stability and safety. Additionally, dual-fuel engines exhibit reduced cyclic variability, particularly under light loads, mainly due to the consistent and reliable ignition provided by the diesel pilot fuel.

The robust construction of diesel-derived dual-fuel engines allows them to better withstand high loads and potential knock events, while maintaining low heat losses. Good cogeneration potential, known as combined heat and power which refers to the engine's ability to produce both mechanical and useful thermal energy, is also inherited through the diesel engine. Kabeyi et al. [39] refers to cogeneration as an efficiency strategy aimed at reducing fuel consumption for each unit of energy produced. Unlike spark-ignition engines and similar to traditional diesel engines, power output in dual-fuel engines is primarily regulated by adjusting the fuel mixture concentration (quality control) and maintaining a quasi- constant airflow [40] rather than throttling which adjusts the quantity of intake air (quantity control). This quality control allows operation over a broader range of air-fuel equivalence ratios and turbocharging levels [8].Throttling results in a considerable loss of torque due to the energy required for the pumping loop. As a result, diesel and dual-fuel engines can maintain higher thermal efficiency compared to SI engines [40].

Since dual-fuel engines retain the high CRs and torque typical of diesel engines it would require smaller adjustments in pilot fuel injection timing in comparison to the substantial ignition timing changes needed in SI engines. Additionally, SI gas engines require an adequate and uninterrupted gas supply [41]. Particularly for methane applications in conventional SI engines, spark timing must be carefully controlled and optimised for satisfactory and efficient operation, particularly during lean engine operation. Thus, the

quality of the gaseous fuel utilised such as its octane rating, would have significant effects on the limitations of the engine configuration. However, in dual-fuel engines that utilise pilot diesel injection, this requirement for timing adjustments is reduced, even with a constant injection timing [23]. The implementation of this reliable and positive ignition method significantly mitigates engine cyclic variation, leading to smoother operation. It also provides several key advantages in engine performance, including the ability to operate on a broad range of fuels as outlined in Section 2.2.

Due to the required continuous change in spark timing with varying load and fuel mixture, SI gas engines have been preferred to be used in stationary applications, characterised by large, multi-cylinder configurations. In fact as previously mentioned, one half of the Dellimara phase 3 power plant in Malta [10], consisting of eight 16.6 MW Wärtsilä 50SG gas engines, ignite the gas and air mixture with a spark plug [42]. However, the rest of the engines were preferred to be dual-fuel operated. This dual-fuel capability provides fuel flexibility, operational continuity, and reliability, allowing the plant to maintain power generation without interruption regardless of fluctuations or issues in natural gas supply [11]. The SI engines tend to operate at lower speeds and exhibit lower efficiency, primarily due to their susceptibility to knocking, especially when fuelled with certain gaseous fuels like raw or unprocessed natural gas. This tendency limits their performance and makes them less suitable for dynamic or high-demand applications. As a result, SI gas engines have increasingly been replaced by dual-fuel engines [8].

2.4 Dual-Fuel Combustion Process

In order to highlight the difference and complexities of combustion of a DFE, first the combustion process of a SI and CI engine is briefly explained.

2.4.1 Combustion in a SI engine

For a SI engine, Figure 2-1 developed by Weaver et al. [28] depicts well the combustion sequence inside an internal combustion engine. Such engines are typically supplied with almost a homogenous air-fuel mixtures [43] where combustion of these mixtures in a SI engine do not fully utilise all the fuel present. A homogeneous mixture can be achieved by injecting the fuel during the intake stroke, as this facilitates an ideal condition for uniform dispersion of fuel droplets to evaporate and mix with air due to air turbulences

[43] [44]. It is understood that as the lambda (λ = ratio of actual Air Fuel Ratio (AFR) to stoichiometric AFR) coefficient increases, a greater proportion of the fuel in the mixture will be burned. In very lean mixtures, layering of the mixture in the combustion chamber takes place using Direct Injection (DI) where rich mixtures are formed around the spark plug and gradually leaner in areas further away from the electrode, eventually reaching the air at the walls of the combustion chamber. However, it is also known that petrol and air mixtures with a λ value greater than 1.4 cannot be ignited by a spark [43].

After the initial spark, a spark delay takes place during which a flame kernel (early stage of flame initiation [45]) created by the spark expands to a significant size. Subsequently, the flame front propagates through the combustion chamber. The rate of this propagation is influenced by the flame speed, which depends on factors such as the air-fuel ratio, turbulence level and temperature. As the volume of hot burned gases increases behind the flame front, it exerts pressure on the cooler unburned charge outwards. This results in an overall increase in cylinder pressure, which raises the temperature of the unburned charge through compression heating. Finally, during the late combustion phase, any remaining components of the unburned mixture are consumed as the piston descends [28].

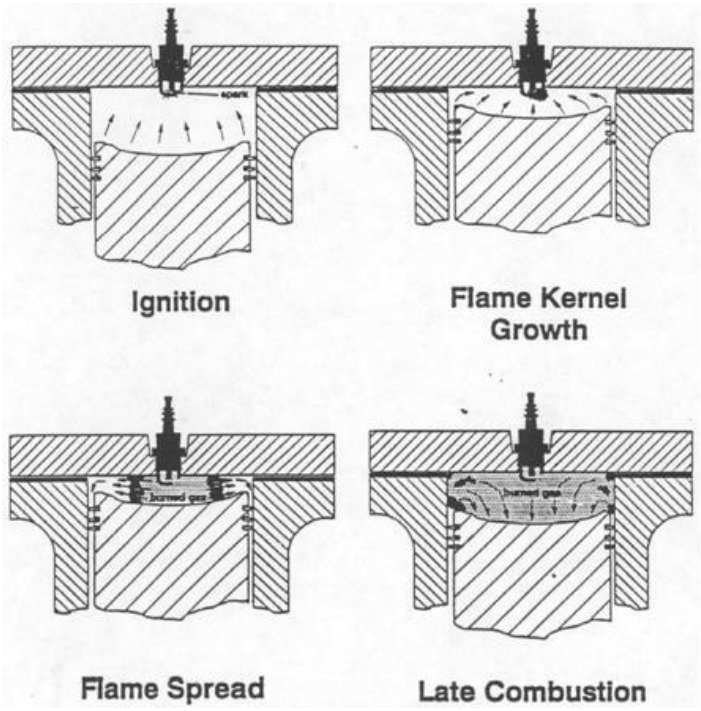

Figure 2-1: Normal combustion sequence in a spark-ignition engine [28].

Fuel in SI engines can be delivered in two different configurations, Port Fuel Injection (PFI) and Direct Fuel Injection (DFI). Although commonly PFI was being used in SI ignition engines, Gasoline Direct Injection (GDI) is lately being implemented [46]. Mitsubishi was the first manufacturer globally to implement GDI engines in the mass-produced Carisma model, which operated through the utilisation of stratified mixtures. This combustion technique helps to reduce fuel consumption, particularly at lower engine speeds and power levels. Stratified mixtures are formed when injection timing is retarded during the compression stroke just before ignition, preventing the formation of a uniformly distributed mixture within the combustion chamber due to lack of time [43] [44]. Thus, the position of the injector must be mounted in such a way to direct the injected fuel towards the electrodes of the spark plug. With such a configuration, the stratified mixture would result to have a high concentration near the spark plug electrodes and gradually changes to a leaner concentration as it approaches the walls of the combustion chamber. As a result, the average lambda (λ) value factor for a stratified charge in this configuration falls outside the acceptable flammability range.

2.4.2 Combustion in a CI engine

The combustion formation in a diesel engine is characterised by a heterogeneous mixture formation followed by auto-ignition. The air reaches pressures of 500-800 kPa and temperatures of 750-900 K during the compression stroke [40]. Just before the TDC, the diesel fuel is injected into the cylinder with high pressures in order to have the ability to penetrate far into the combustion chamber [47]. Due to the high temperatures created, auto ignition of diesel is induced. This injection technique is referred to as “high pressure late direct injection” [40]. The fuel is atomised into fine droplets at the injector nozzle and must undergo evaporation prior to achieving an effective mixing, thereby resulting in a heterogeneous mixture. Similar to a stratified mixture, in a heterogeneous mixture the lambda value varies from pure air to pure fuel near the spray core [40]. Brown et. al [48] uses a photograph of granite to illustrate the difference between a stratified mixture and a heterogeneous mixture, emphasizing that unlike stratified mixtures, the constituents in a heterogeneous mixture do not necessarily form distinct layers. A typical diesel-spray is illustrated in the Figure 2-2, which is characterised by two main distinct zones: a core region and an upstream jet or spray.

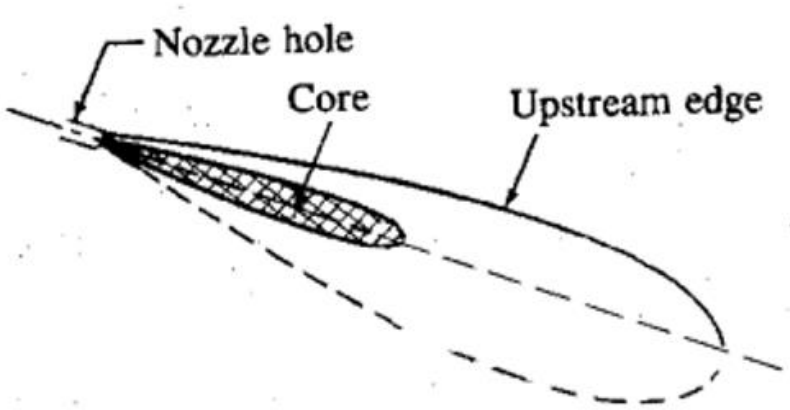

Figure 2-2: Fuel spray injection in a diesel engine [40].

The primary challenge is to ensure an effective mixing of fuel and air within the engine in a limited timeframe, specifically at a designated crank angle near TDC. This is made possible through DI of fuel, coupled with rapid evaporation which facilitates this process [40]. In addition, mixing rates can be enhanced by employing swirl and optimising the bowl-in-piston combustion chambers, thereby affecting the rate of chemical energy release [49].

The combustion process in diesel engines is commonly described using two complementary frameworks: the four-stage model and the two-phase flame model. The four stages of combustion is described in Figure 2-3 [50], where the pressure is represented on the vertical axis and crank angle in degrees on the horizontal axis. The negative angles are used to indicate angles of crank before the piston reaches TDC. From this figure one can observe the following phases: A-B – period of delay in ignition (start of fuel injection), B-C – premixed combustion (all the fuel has been injected causing a rapid increase in pressure), C-D – Main combustion (the fuel is burned, generating power), D-E – Late combustion (pressure decreases due to less combustion occurring) [47] [50].

Complementing this, since the combustion process commences shortly after the Start Of Injection (SOI) of the fuel, the process can also be described by focusing on two main flame phases. The first phase is referred to as the "premixed flame" phase, which denotes the period from the moment when the fuel is injected until ignition takes place. During this phase, the fuel combines with air and ignites spontaneously. Auto ignition is largely influenced by temperature and is less sensitive to changes of cylinder pressure at the end of the compression stroke [40].

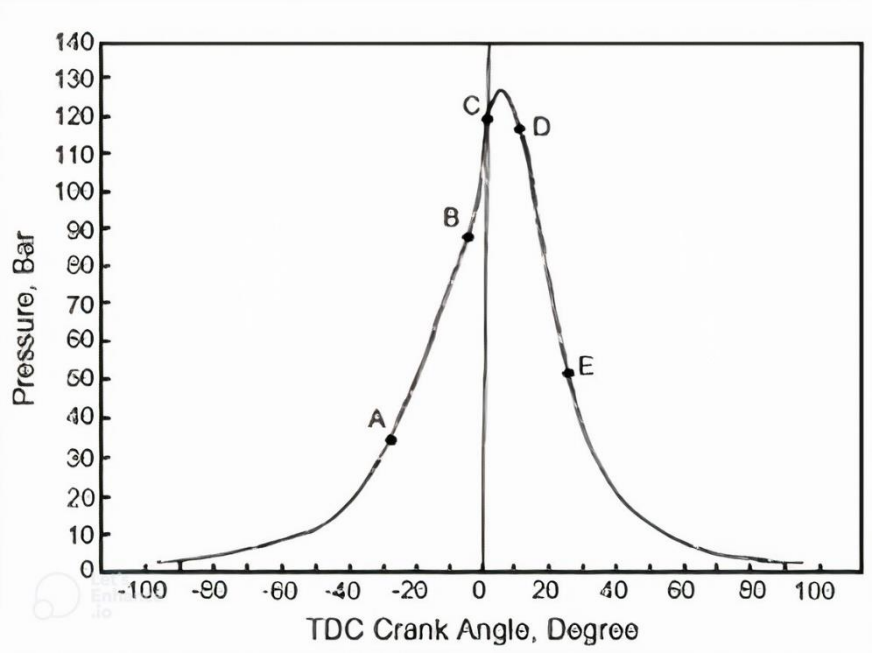

Figure 2-3: Stages of combustion process in diesel-only engine [75].

The second phase is known as the "diffusion flame" phase. This phase may overlap with part of the injection period but occurs after the premixed air-fuel mixture. The diffusion flame burns at a slower rate than the premixed flame and is the main cause for most of the pressure rise that generates work as well as being a significant contributor to NOx formation. In cases of significantly advance timing only, the "pre-mixed flame" phase plays a role in the increase in pressure [40]. In addition, the temperature and pressure of the intake air effect the mixture burning rate which further impacts on the peak of the diffusion flame [49]. Predominantly during lean engine operation, when the intake air temperature is reduced the combustion characteristics are drastically affected. Such behaviour is explained from the increase in the heterogeneity of the fuel-air ratios found in the combustion chamber leading to narrowing of the effective lower flammability limit [41].

2.4.3 Combustion in a dual-fuel engine

As mentioned in Section 2.1, it is well established that for combustion to take place in a conventional dual-fuel engine, a specific amount of liquid fuel (pilot fuel) must be injected into a homogeneous mixture of pre-mixed air and gas near TDC [8]. This dual-fuel combustion process is better explained in Figure 2-4 [51] where a mixture of the two combustion methods employed in a CI and SI are highlighted.

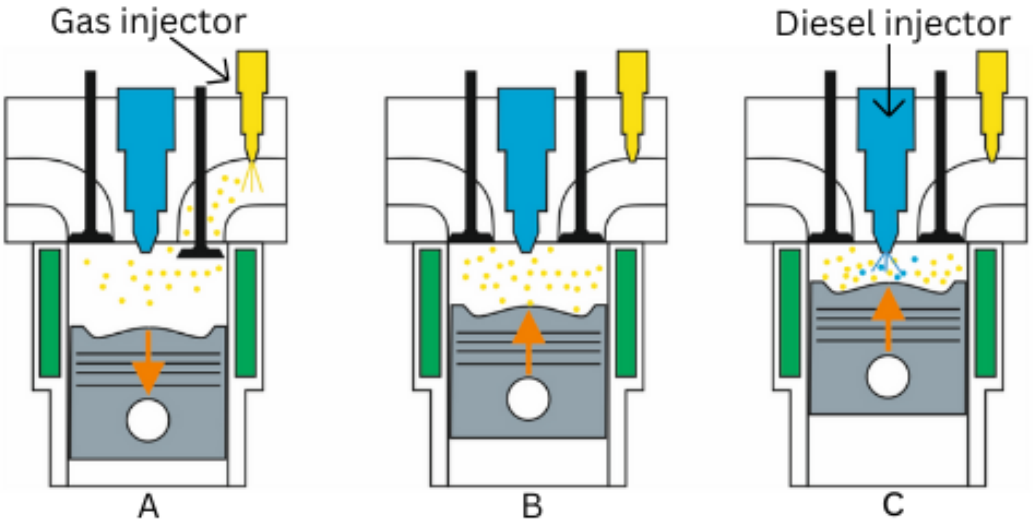

Figure 2-4: A diagram consisting of three instances which depict the combustion of DFEs employing a mixture of CI and SI combustion methods [51].

During the intake stroke, the gaseous fuel is introduced into the intake system and drawn into the cylinder through the intake port and thoroughly mixed with the incoming air charge, as depicted in (A). This homogeneous air-fuel mixture is subsequently compressed during the compression stroke, as illustrated in (B), following a process analogous to that observed in a conventional SI engine. However, unlike spark-ignited systems, combustion in this dual-fuel configuration is initiated by a small pilot injection of diesel fuel near TDC of the compression stroke rather than a spark plug. This pilot injection, shown in (C), triggers ignition through CI mechanisms, thereby sustaining the combustion process similar to that found in a CI engine [21].

One must appreciate that the main role of the diesel pilot fuel which has a high cetane number is to ignite the gaseous main fuel which has a high RON [52]. This pilot fuelling strategy is crucial to reduce the ignition delay of DFEs [49]. However, a complex interaction occurs between the liquid fuel spray and the bulk premixed gaseous fuel–air charge. This interaction involves both thermal effects and a substantial chemical kinetic component, which can result in extensions of ignition delays and increased emissions. The pilot fuel in a CI engine is necessary since gaseous fuels often have a high auto ignition temperature. For natural gas the auto ignition temperature is around 580°C which does not ignite under the compression unless the intake temperature is significantly heated to elevated temperatures [8]. As seen in Figure 2-4, dual-fuel

systems typically injects the gaseous fuel with air in the intake manifold however this fuel delivery tends to displace the intake air directly affecting the volumetric efficiency of the engine thus limiting CRs of up to 80% [22]. Another fuel delivery system which can be employed is DI which can reach SRs of up to 95%.

DI of gaseous fuel into the cylinder, particularly in modern engine systems, introduces additional complexity. In fact, during his studies Park [20], for simplicity reasons decided that an intake manifold fumigation was chosen to deliver CNG to the engine. DI requires generating a sufficiently high-pressure gas supply on board and precisely injecting the fuel gas into the cylinder at the correct moment. The timing and coordination of this injection, along with the mixing of the gaseous fuel and the liquid pilot fuel, demand careful sequencing, control, and execution [8].

Although typically diesel is used as a pilot fuel, due to its high hydrocarbon content it significantly changes the mixture's resistance to auto ignition [23], other alternative fuels have been explored. Namasivayam et al. [52] studied the combustion characteristics of a dual-fuel engine using emulsified biofuel for pilot ignition. The emulsified pilot fuels were found to have extended ignition delays when compared to diesel by a maximum of 10% which caused a 30% reduction in the peak combustion pressures. The author also commented that pilot fuel accounts for less than 10% of the maximum power output, meaning that the primary gaseous fuel predominantly controls the overall power output.

2.5 Hydrogen Combustion Process

After the combustion processes of SI, CI, and dual-fuel engines, were reviewed the fundamental H_2 combustion characteristics was evaluated. This literature review will then be used to compare with the results obtained from the H_2 experiments. Notably, although SI combustion was briefly discussed earlier, it is essential to first highlight the role of the spark in SI engines, given that the H_2 testing was conducted using this configuration.

2.5.1 Importance of Spark Timing in SI Engines

Ignition delay is inevitable in any type of internal combustion engine and becomes crucial to regulate especially in SI engines, where precise control of ignition advance is essential to obtain maximum torque. Performance can be effectively analysed by observing in-cylinder pressure variations with adjustments in ignition timing. Studies conducted by Binjuwair and Alkudsi [53] and Weibo Shi et al. [54] utilised petrol and H_2 fuels respectively and the results of the two engines demonstrated consistent findings. Specifically, both fuels demonstrated the highest peak pressures with increased ignition advance. The peak pressure achieved in an engine leads to enhanced torque and brake power characteristics, as illustrated by Zareei and Kakaee [55] in Figure 2-5 whilst performing petrol experiments. The authors noted that while advancing the spark timing initially leads to an increase in torque output, further advancement beyond a certain point result in a decrease in torque. This phenomenon occurs due to a rise in in-cylinder peak pressure during the compression stroke and a corresponding reduction in pressure during the expansion stroke.

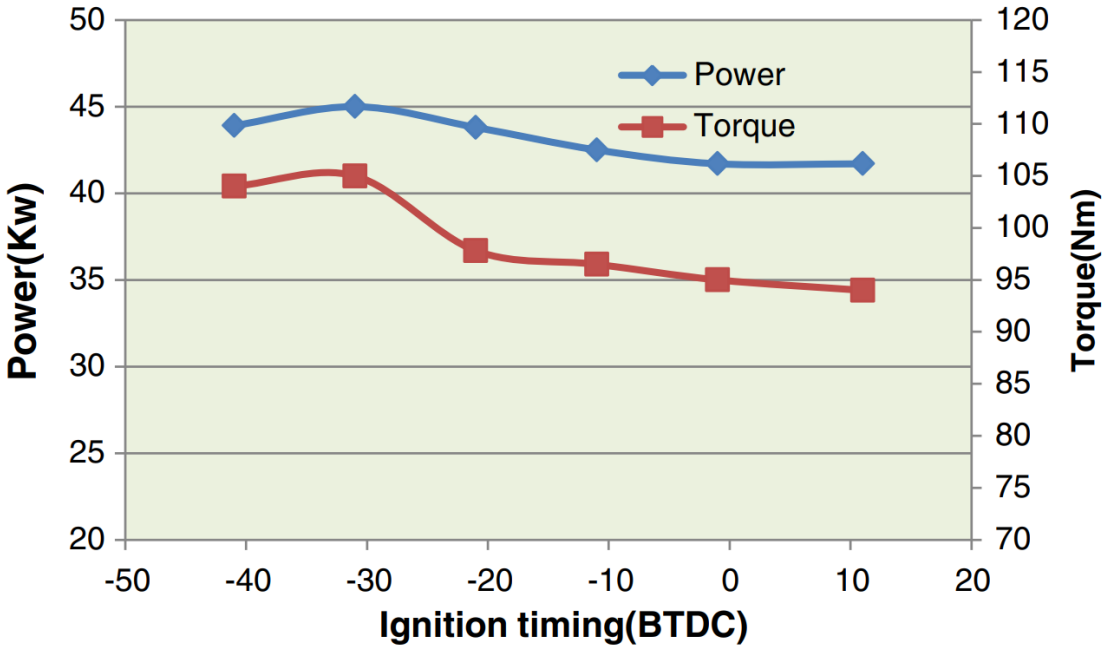

Figure 2-5: Variation of brake power and torque with different spark timings [55].

The ignition timing at which maximum torque is achieved is known as the Minimum Advance for Maximum Brake Torque (MBT). It is important to recognize that MBT timing varies with engine speed and throttle position which directly effects the Manifold Absolute Pressure (MAP). Consequently, when operating with a higher dense charge, a less ignition timing advance would be required when compared to a less dense charge.

Tunka and Polcar [56] emphasised that ignition timing operates as an independent variable, while engine power and torque are dependent variables. Optimal ignition timing facilitates a more efficient conversion of the fuel's chemical energy into mechanical work.

Furthermore, the optimal ignition advance can be assessed not only by evaluating torque and brake power but also through the analysis of exhaust gas temperatures. Late ignition results in elevated exhaust temperatures due to a delayed combustion onset during the expansion stroke, which causes afterburning in the exhaust phase. This condition negatively impacts the engine's thermal efficiency, as the thermal energy released from combustion in the cylinder escapes rapidly through the exhaust system rather than being effectively converted into mechanical work [56]. From the experimentation conducted by Tunka and Polcar [56], the relationship between exhaust gas temperature and ignition advance timing during petrol testing is illustrated in Figure 2-6. This figure clearly shows the effect that ignition advance timing has on the exhaust gas temperature, leading to a temperature variation of 100°C. Amongst their petrol experimental results, Binjuwair and Alkudsi [53] investigated the impact of ignition advance on thermal efficiency and concluded that a thermal difference of 5% was found between the minimum and maximum ignition timing angles.

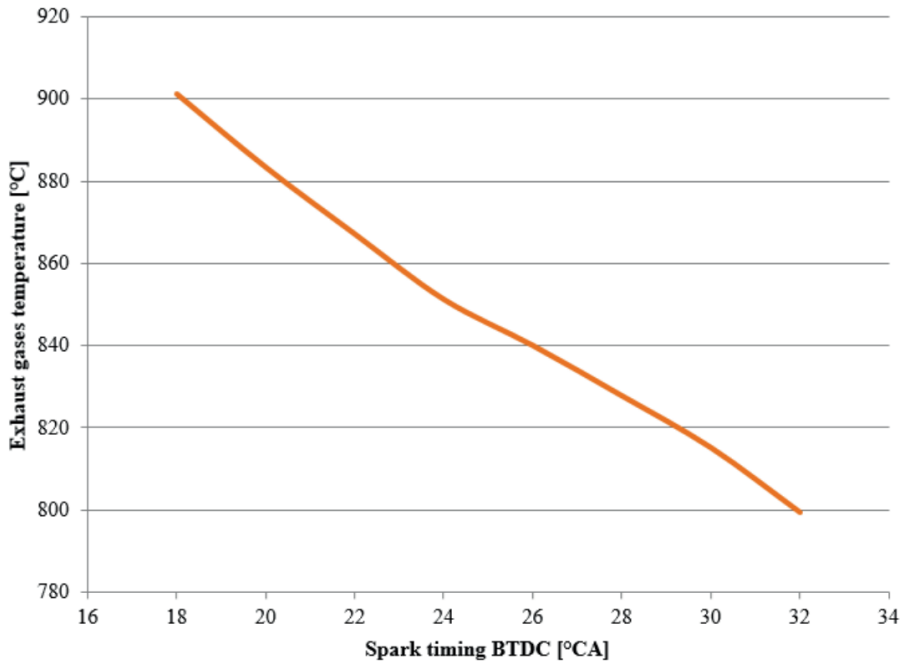

Figure 2-6: The dependency of spark timing on exhaust gas temperature during petrol testing [56].

2.5.2 Optimal Spark Timing in H_2 Engines

A two-zone quasidimensional model was developed by Hailin and Kharim [57] to predict the performance of a H_2 fuelled SI engine. During the investigation, the effects of change in CR were established. The optimised spark timing was plotted against Equivalence Ratio (Ø = ratio of stoichiometric AFR to actual AFR) at CRs of 8 and 10 at a MAP of 100 kpa as depicted in Figure 2-7. It is evident that spark timing must be retarded near stoichiometric conditions when compared to lean mixtures.

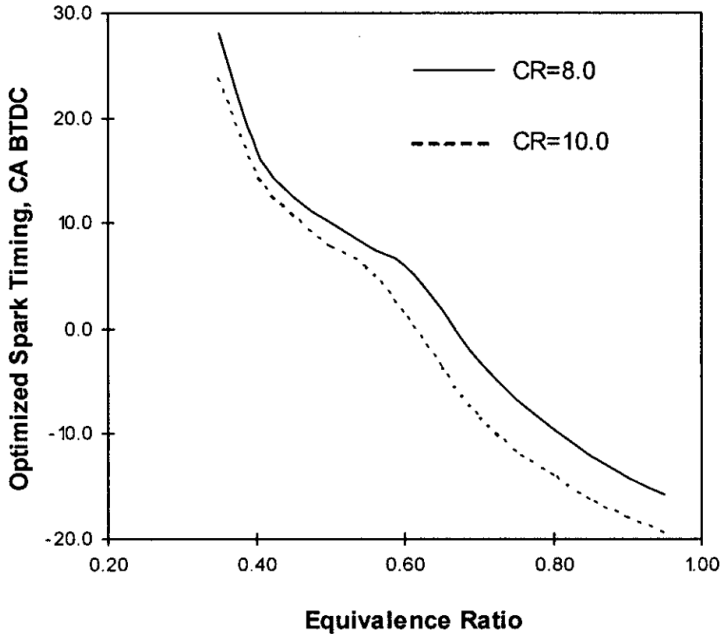

Figure 2-7: A comparison of the typical variation of the optimized spark timing with changes in Ø and CRs. T_{in}=311 K, P_{in}=100 kPa [57].

From the evaluation of the curves found in Figure 2-7 it can be concluded that for the two different CRs it can be revealed that at low Ø, the difference in required spark timing is less significant than the mixtures near stoichiometric conditions due to the difference in the gradients of the graph. It is also noted with increasing CRs, the SI is delayed for MBT. For the satisfactory operation of a SI engine when using H_2, the author emphasised the importance of maintaining a sufficiently wide operational mixture range, particularly during lean operations, when employing a high CR. This is essential to guarantee satisfactory performance of a SI engine running on pure H_2. Similar observations where noticed by Purayil et al. [58] which commented on the necessity to optimise the spark timing to prevent the occurrence of knock, as demonstrated in the extrapolated graph in Figure 2-8. The data indicate that as the fuel injection quantity increases, it became

necessary to retard the spark timing to avoid the onset of knock. This notion of delaying the spark is referred to as knock-limited spark advance (KLSA).

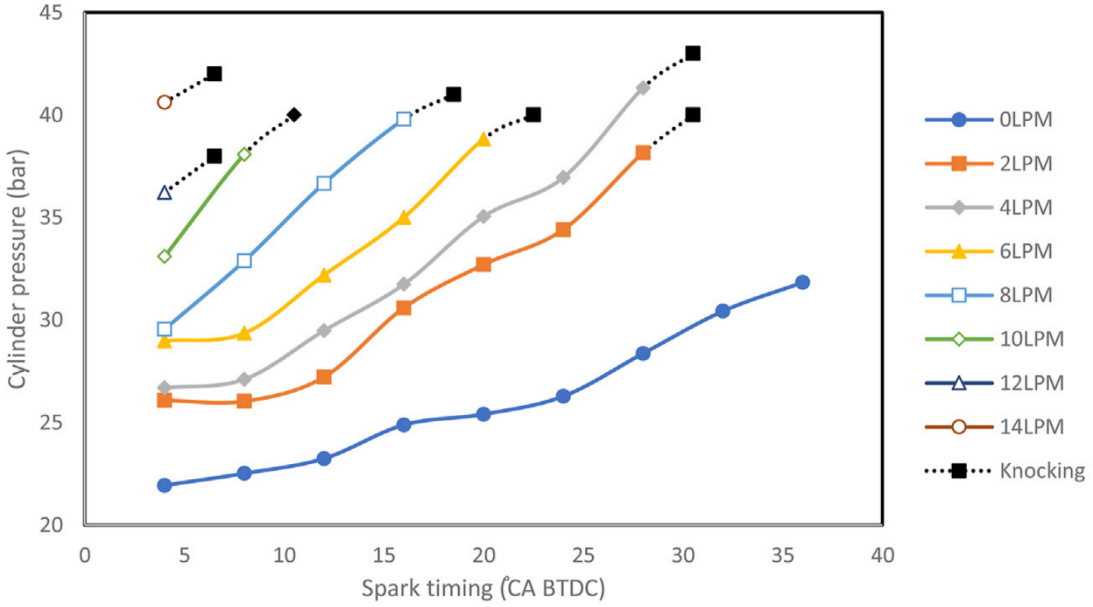

Figure 2-8: Peak Cylinder pressure as a function of spark timing for different H_2 flow rates [58].

Molina et al. [59] performed various H_2 tests with both PFI and DI strategies at an engine speed of 1500 RPM having a CR of 10.7:1 and conducted various research on multiple parameters. From these, the characteristic combustion periods CA10, CA50, CA90 and spark timing were plotted against λ at an engine speed of 1500RPM and low-load conditions depicted in Figure 2-9. In contrast with the ignition timing used by Hailin and Kharim [57], Molina et al. [59] did not use ignition timings after TDC near stoichiometric conditions despite having similar CRs to obtain MBT.

Rrustemi et al. [60] performed a similar investigation of H_2 combustion by utilising a numerical model which was validated with experiments conducted by Sementa et al. [61]. Similar to the results of Hailin and Kharim [57] depicted in Figure 2-7, Sementa et al. [61] for MBT during naturally aspirated conditions at λ=1.3 a spark timing of 10° CA BTDC was obtained when using a CR of 11.5. On the other hand, Demuynck et al. [62] utilised later ignition advances varying from 5 to -15° CA BTDC whilst analysing heat flux. Additionally, at leaner mixtures of λ=2.5 Rrustemi et al. [60] obtained a ST of 20° CA BTDC for MBT while Hailin and Kharim [57] utilised later spark timing of 15° CA

BTDC to obtain MBT. Such a small difference in spark timing might have occurred due to differences in the engine speeds and CRs.

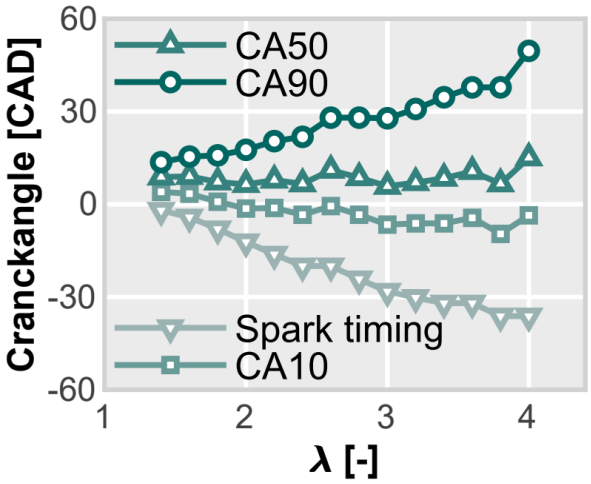

Figure 2-9: Characteristic combustion periods (CA10, CA50 & CA90) obtained at 1500 RPM engine speed and low load conditions for various λ values [59].

Lindqvist and Overby [63] referred to Al-Baghdadi [64] which through simulation provided a general idea of how optimal ignition timing varied according to engine load and speed. It was concluded that for lower loads, the ignition timing would occur over an earlier range between 18 to 26° CA BTDC and a later range between 10 to 18° CA BTDC for medium to full loads. Moreover, Lindqvist et al. [63] emphasised, these data findings can only provide a vague overview of the available window for optimal ignition timing since ultimately the ignition timing can heavily vary between engine configurations and geometry. Similar to Hailin and Kharim [57], Al-Baghdadi [64] numerically investigated through simulation the effects of CRs and SI timing and similarly derived the conclusion that as CR increases, ignition has to be set closer to TDC. This retardation is necessary due to the higher pressures and temperatures in the cylinder as well as high flame speeds which causes favourable ignition conditions due to the high CRs. Al- Baghdadi [64] presented a range between 4 and 20° CA BTDC for a CR between 12 and 6:1. Also as ∅ approached unity, the ignition timing had to be closer to TDC at a specific CR when compared to lower and higher ∅. Similarly, Al-Baghdadi [64] commented that deviations from the stoichiometric ∅ necessitate timing adjustments since lean mixtures reduce flame temperatures and combustion velocity. Rich mixtures limit available oxygen for combustion, while lean mixtures lower energy density, both resulting in slower flame speeds and delayed combustion progression [64].

The need of spark timing with different ∅ was further investigated by Verma [65] by generating in cylinder pressure data using a numerical simulation model of an engine having a CR of 9.5 at different engine speeds whose results are depicted in Figure 2-10. As expected with an increase in engine speed the spark timing is advanced drastically since the time required to cover same angular distance decreases. This advance in spark timing is more pronounced during lean mixtures rather than during rich mixtures which can be used to explain the similarities and differences in ST obtained by Hailin and Kharim [57] and Rrustemi et al. [60] during rich and lean mixtures. Verma et al. [65] also emphasised that for H_2 ICEs during stoichiometric conditions a lower spark timing between 0 to10° CA BTDC is required when compared to gasoline fuelled SI engines.

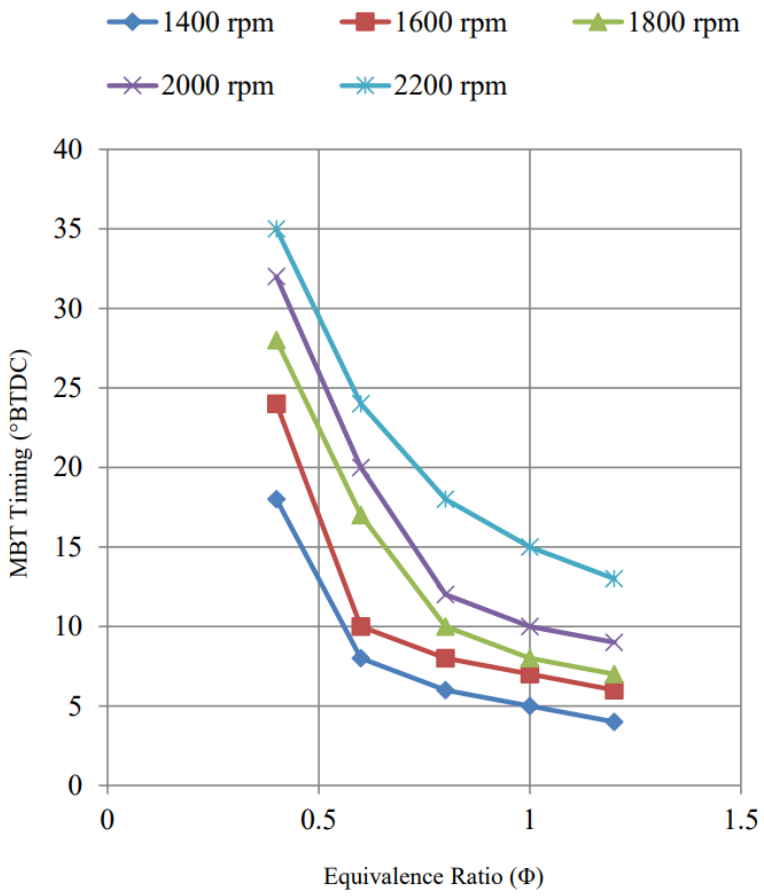

Figure 2-10: MBT timing against equivalence ratio [65].

Furthermore, Verma [65] commented that when the spark timing was advanced BTDC, the HRR also advanced showing earlier combustion of the fuel-air mixture, hence the combustion process started before the completion of the compression stoke and

continued in the expansion stroke. In addition, as spark advances the work required for compression increases but peak pressure also increases. In some instances, later timings would be beneficial since enough energy would be provided during the expansion stroke when the crank shaft leverage is high and peak pressure can use this advantage to produce higher expansion work resulting in greater torque output. However, if the spark timing is progressively delayed towards TDC, the compression work decreases however the peak pressure also decreases and takes place later during the expansion stroke. With too late spark timings the peak pressure would decrease to a certain extent which cannot be compensated by the higher crank shaft leverage resulting in a reduced total expansion work. The authors [65] also highlighted the parameters on which the optimum spark timing would depend upon; the rate of flame development (flame speed), path of the flame in combustion chamber and flame termination process after reaching the wall. These parameters surely differ when using different fuels and will directly affect the Mass Fraction Burned (MFB) crank angle values at different speeds and ∅. Verma [65] concluded that for stoichiometric mixtures the crank angle position of 50% MFB for petrol was of 10° Crank Angle (CA) After Top Dead Centre (ATDC) and changed to 0-1° CA ATDC during H_2 fuelled internal combustion engines due to the high burning rates of H_2 combustion.

To reduce undesired auto ignition when using H_2 fuel, Ceper [66] commented on how the ignition system needs to have a low residual charge. H_2's high-pressure insulating properties necessitate the use of spark plugs with smaller spark gaps with an optimal gap of 0.4 mm to reduce ignition voltage and residual energy compared to conventional petrol engines which commonly employ a gap of 0.8 mm [67]. This design helps to avoid challenges like voltage spikes improving the combustion reliability of the H_2-fuelled engines. Further reductions in residual energy can be achieved through optimised grounding systems or modified ignition cable resistance. Importantly, platinum electrodes should be avoided to prevent catalytic reactions with H_2 [68] that would create localised hotspots, which shortens the engine's lifetime.

2.5.3 Combustion Burn Duration

Negurescu et al. [69] conducted experiments at an engine speed of 3000 RPM at wide open throttle. From the extensive data collected, a graph of burning combustion duration in degrees Relative to After Compression (RAC) with varying lambda depicted in Figure 2-11 was composed. It is evidently shown that for leaner mixtures, the burn duration lengthens considerably. Such results can be indirectly related through the various Heat Release Rate (HRR) profiles found by Molina et al. [59] which were found to flatten and widen under diluted conditions. This behaviour aligns with findings that lower flame propagation velocity and disrupted flame structure contribute to prolonged combustion phases.

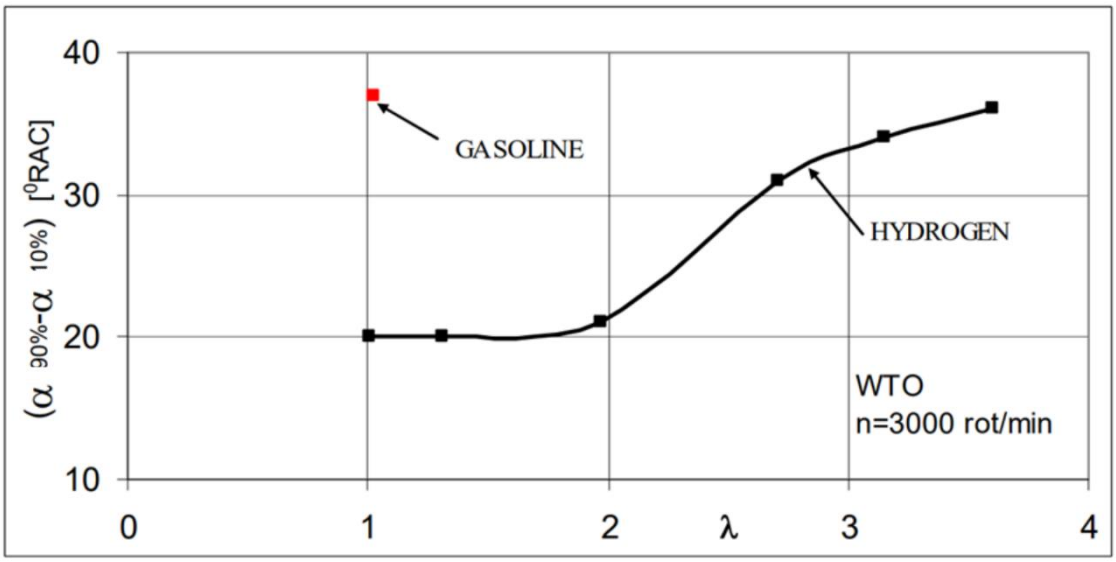

Figure 2-11: Burning combustion duration versus λ at wide open throttle [69].

In addition, Aljabri et al. [70], performed similar investigations through CONVERGE^{TM} simulation software and presented a graph depicted in Figure 2-12 of burn duration (CA90-CA5) with CR at a lean mixture of λ=2.85 and spark timing of 5° CA ATDC. It is evidently seen that CRs have a great impact on the burn duration of the air to fuel mixture. With high CRs of around 16.5 the burn duration is almost completely avoided when compared to a burn duration of 10° CA at CRs of 11.5. This difference in burn duration would ultimately require the need of spark timing optimisation especially during stoichiometric mixtures. As outlined by Hailin and Kharim [57] in Figure 2-7 when utilising lean mixtures, the adjustment in spark timing is not as significant.

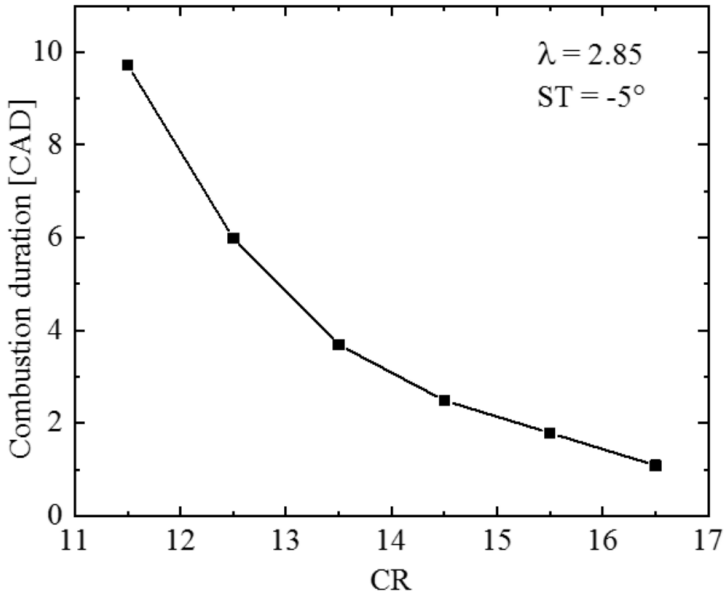

Figure 2-12: The variation of combustion duration with CR [70].

Among the previously mentioned work by Rrustemi et al. [60], a graph depicting burn duration against lambda for different MAPs is shown in Figure 2-13. It is evident that an increase in MAP prolongs the burn duration only at lean mixtures above a λ=1.5, compared to lower MAP values. For richer mixtures, variations in MAP do not significantly affect burn duration. This behaviour at lean mixtures is expected due to reduced burn velocities associated with slower laminar flame speeds.

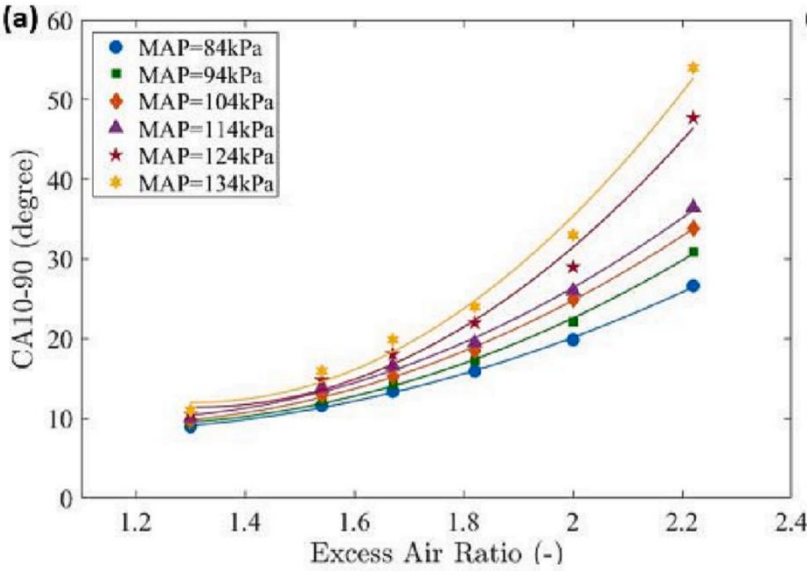

Figure 2-13:The variation of burn duration with λ for different MAPs [60].

2.5.4 Heat loss and blow-by

Heat transfers from the combustion gases to the engine walls greatly affects the efficiency and power output in internal combustion engines. Based on the experimental setup described by Demuynck et al. [62], the heat loss of different fuels was investigated. Amongst the multiple results deduced Figure 2-14 depicts the variation of heat flux when the throttle position and CR was changed.

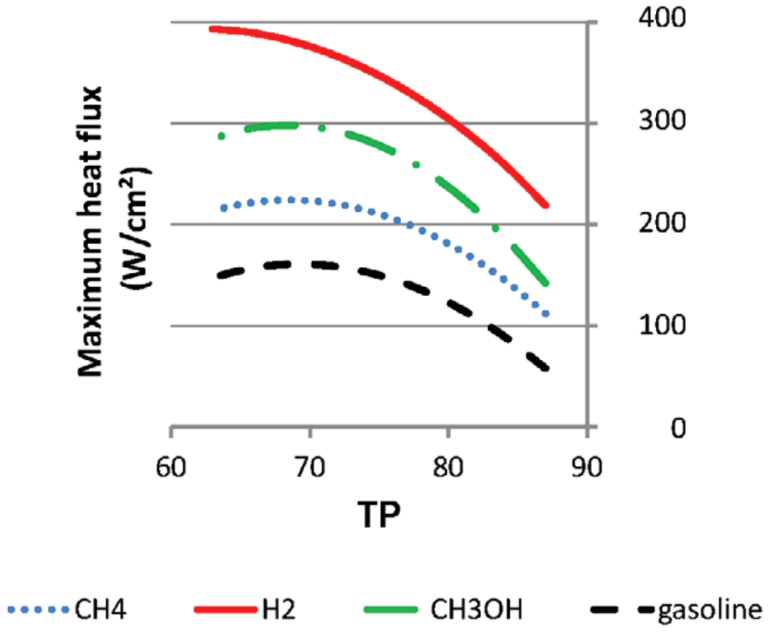

Figure 2-14: The variation of the maximum heat flux with Throttle Position (TP) and Compression Ratio (CR) for different fuels [62].

The authors [62] commented that during a partially closed throttle, the turbulence created improves the mixing of air and fuel, which leads to more efficient combustion over a larger area. This enhanced mixing can cause a higher heat flux than that experienced at wide open throttle because the combustion is more evenly distributed and the flame interacts more effectively with the combustion chamber surfaces. However, at wide open throttle, although there is less turbulence and mixing may be less intense, the engine receives a much larger amount of air and fuel. This results in a higher overall combustion temperature and greater total energy release which contrary to expectations results in a lower heat flux according to Figure 2-14. This turbulence of the ingoing flow created by the throttle position was less noticed during the H_2 experimentation and can be explained from the high diffusivity in air of 0.63 cm^2s^{-1} which results in a more uniform mixture formation [65]. The extended duration of fuel injection might also influence the extent of mixing between the fuel and air [62]. When the CR was increased,

it resulted in an increase of heat flux for H_2, methane and methanol. The effects of the ignition timing and air-to-fuel Ø on the maximum heat flux are plotted in Figure 2-15.

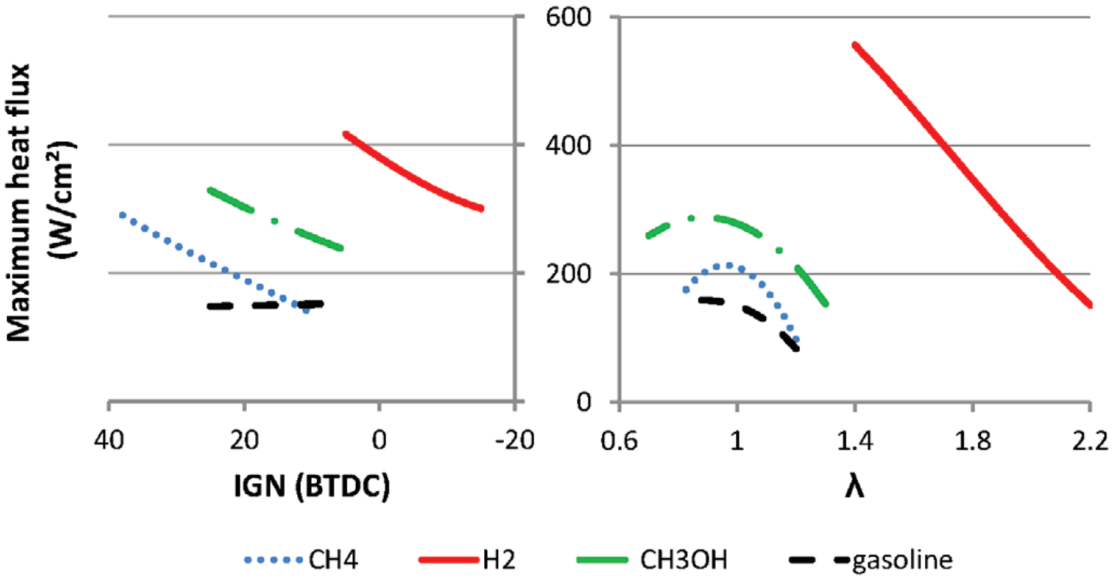

Figure 2-15: The variation of the maximum heat flux with ignition timing and λ [62].

For petrol, methane and methanol as ignition was advanced, at stoichiometric conditions the heat flux is seen to increase due to a higher peak gas temperature. Similar stoichiometric experiments of H_2 were not able to be performed due to the occurrence of abnormal combustion. Hence, lean H_2 mixtures had to be used which resulted in a higher peak heat flux even during advanced ignition timings. The heat flux is seen to be more affected when the AFR is changed. H_2's heat flux seems to vary linearly with air to fuel mixture when compared to the other fuel graph profiles. It is also important to notice that at leaner mixtures, the heat flux of H_2 seems to be similar to the peak heat flux obtained from the other fuels. The authors [62] commented that stoichiometric H_2 experiments will be carried out and the heat flux is expected to be three times higher than that of the other fuels. This high heat flux of H_2 might be mainly caused due to the small quenching gap of H_2, 0.6 mm compared to the higher 2 mm quenching gap of petrol [71]. Hence, during H_2 combustion the flame diminishes closer to the internal cylinder walls increasing the temperature gradient between the hot gases and the cooler wall surface encouraging heat transfer.

Pipitone and Beccari [72] during his evolution of the TDC determination method, commented on how besides the capability of the cylinder walls to exchange heat with the gas, the thermal energy within the mass leaked through the valve seats and piston

rings also need to be taken into account. The authors [72] sum up these two losses through determination of the "Loss Function" through evaluation of entropy variations and mass leakage by means of volume and pressure values. The thermodynamic loss angle was also mentioned by Caruana [73] during the formation of a one-dimensional simulation model of heat transfer analysis who commented that blow-by flow typically exerts a minimal influence on the loss angle compared to heat transfer. To incorporate this flow within the model, Caruana [73] referred to Pipitone and Beccari [72] and incorporated an orifice-type valve in each cylinder to account for the blow-by effects. These effects were also investigated by Rahmani et al. [74], who focused on the impact of H_2 combustion on the dilution and degradation of engine lubricants, as well as on the tribological behaviour of engine contact interfaces. The results deduced by Rahmani et al. [74] are depicted in Figure 2-16 where the mass flow rate of gas through the piston ring-pack crevices of H_2 fuelled engines are plotted against crank angle.

During both PFI and DI fuel delivery systems measurements were taken during stoichiometric AFR testing. Rahmani et al. [74] also investigated the differences in blow-by gases between petrol and H_2 experiments with DI fuel delivery at stoichiometric conditions. In the obtained results, the blow-by of gasses tend to be greater during H_2 operation when compared to petrol operation as depicted in Figure 2-16. This higher amounts of blow-by gases are mainly attributed to the higher in-cylinder pressures and temperatures produced during H_2 combustion [74] under stoichiometric conditions. The negative mass flow depicted in Figure 2-16 refers to the back flow of gas which takes place during the power stoke as parts of the gas flow to the back of the rim of the top compression ring and return to the combustion chamber. The authors [74] also mentioned that the type of fuel injection used also affects the quantity of blow-by gases, with PFI appearing to produce a lower quantity of blow-by gases compared to direct fuel injection.

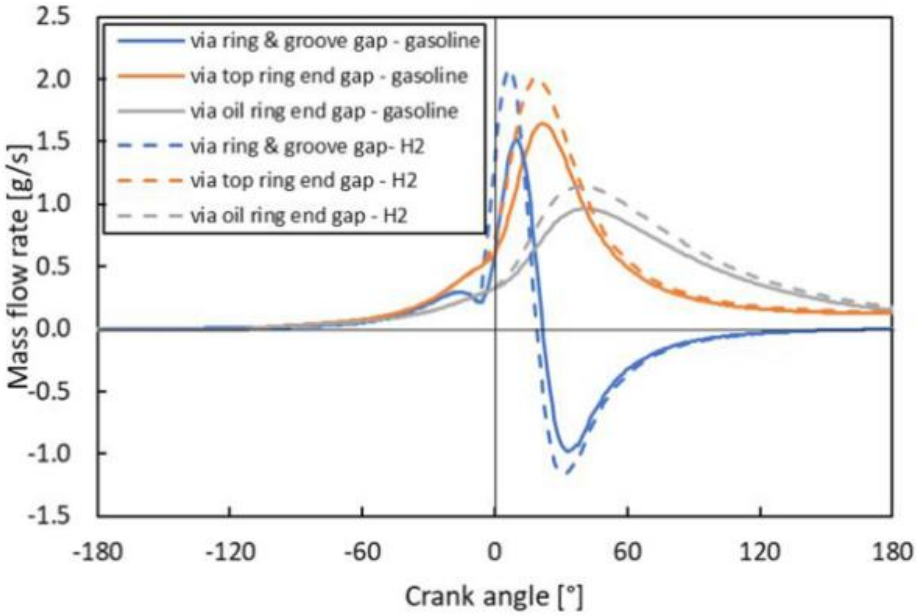

Figure 2-16: The variation of the mass flow rate through piston pack crevices during stoichiometric mixtures of H_2 and petrol for a single cylinder [74].

2.6 Engine Knock in Dual-Fuel Engines

2.6.1 Spark knock

During the compression of the unburned "end-gases" in an engine cylinder ahead of the flame front propagating across the combustion chamber, the temperature rises due to compression heating, leading to the initiation of pre-flame reactions [49]. These undesired pre-flame reactions are referred to as spark knock [75]. If conditions allow for sufficient time and temperature, rates of reaction increase causing these gases to self-ignite before the flame front, generating shock waves and high-pressure spikes. In most instances, the generated shock waves induced by knocking are of an acoustic nature and propagate in all directions within the combustion chamber [76]. Riccardo [13] describes knock as "the setting up within the cylinder of a pressure wave travelling at so high a velocity as, by its impact against, the cylinder walls, to set them in vibration and thus give rise to a high-pitched "ping". Such shock waves can cause damage to the engine and disrupt the quenching boundary layer of gas formed on the combustion chamber walls. This disruption is referred to as 'scouring' by Riccardo [13] who in his classic manuscript mentioned that it serves as the main contributor to increased heat fluxes rather than the elevated gas temperature.

Such increase in heat flux has been measured to be between two to three times the normal heat transfer [49]. Riccardo [13] also noted that the developing flame front is unsmooth due to the presence of turbulence causing the flame to proceed more rapidly and as a ragged flame front. The incidence of detonation of the end gases depends firstly upon the degree of heating and compression that the unburnt gas can endure; the chemical nature of the fuel itself referred to as the octane rating [28]. It also depends upon the opportunities that the unburnt mixture has to get rid of the heat given off by the propagating wave front. Hence, the propagating distance plays a crucial role in affecting the amount of absorbed heat and giving sufficient time for the reactions in the fuel to take place. Riccardo [13] insists that such detonation is dependent upon the degree of turbulence where such an effect can have positive effects; assist the unburnt gases to get rid of its heat and affect the advance of the flame front. However, the turbulence might also increase the amount of radiated heat due to the ragged flame front profile.

Unlike knock in SI engines which is mostly prominent at lower engine speeds and higher loads [76], spark knock in DFEs is seen to decrease with increased load [75]. The reason for this behaviour might be due to the reduction in the delay period [75] affecting the aforementioned propagation distance. Although difficult to quantify, several techniques such as stroboscopic observation through quartz windows in the combustion chamber indicate that the detonation of 5% or less of the total charge can lead to severe knock which if persistent will cause erosion of the piston crown. Syrimis and Assanis [76] conducted experimentation on heat transfer measurement of the piston where two knock intensity levels were obtained at a cylinder head coolant temperatures of 50°C and 80°C. The authors [76] concluded that a linear variation of heat flux with knock intensity occurs at locations with the same heat transfer mechanisms. In addition to this conclusion, Heywood [49] further concludes that the tendency for knocking is affected by several factors such as high CRs, elevated charge temperatures, heat spots, advanced ignition timing, and prolonged combustion.

2.6.2 Diesel knock

The fundamental aspect of knock combustion in dual-fuel diesel engines relies on the fact that sources of self-ignition can arise not only at the interface between the injected stream of diesel fuel and the charge filling the combustion chamber but also within the ambient compressed air and gaseous mixture [77]. This auto ignition would often take

place during the pre-mixed combustion phase, where due to ignition delay the gaseous mixture has mixed well with air but not yet ignited with the pilot fuel. Thus, in certain circumstances self-ignition can spontaneously occur in these regions. When self-ignition occurs in DFEs such as that within an air-methane mixture, it leads to an uncontrolled knock combustion process, disrupting the regular combustion necessary for proper operation of CI engines. It is important to mention that the maximum SR in a DFE is limited by the engine resistance to knock combustion. Methane has a relatively high RON (RON>100) [77] and therefore it is commonly used in SI engines with CRs around 10. In CI engines, usually the average value of the CR is approximately 17 which results in combustion chamber conditions that are not optimal for the use of this fuel. The low cetane value of methane would result in delayed ignition and extended ignition delays. For this reason, methane cannot be added in large quantities to a CI engine [77]. Żółtowski [77] performed experiments and for an engine speed of 1800 RPM, plotted the cylinder pressure against crank angle for different SRs (β) as depicted in Figure 2-17.

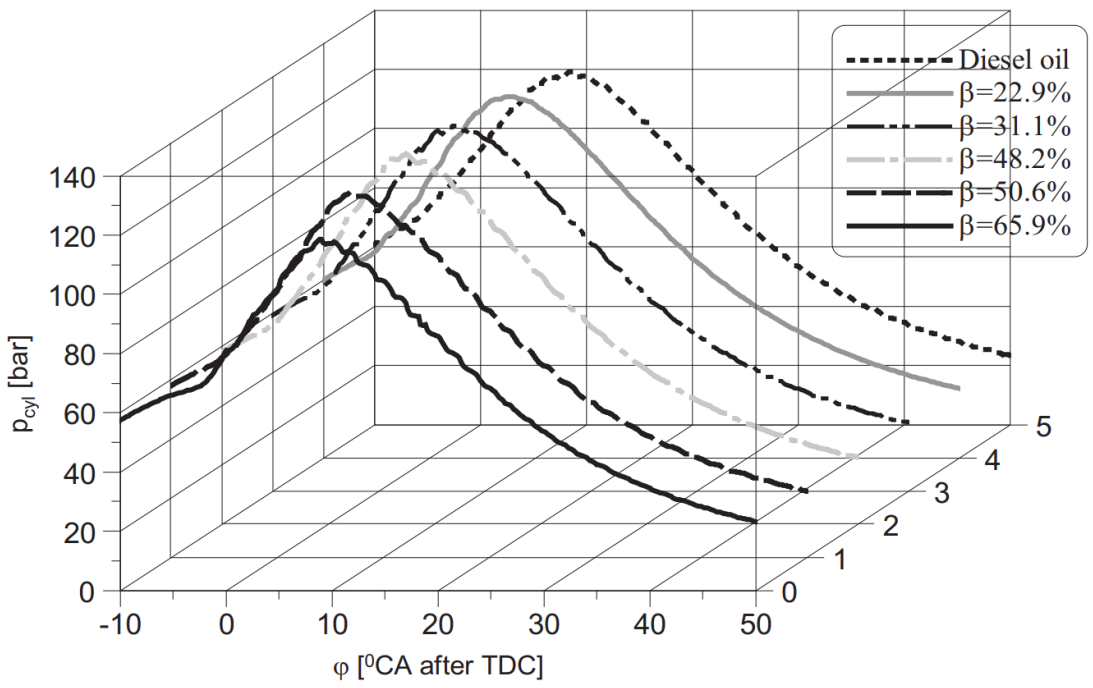

Figure 2-17: The variation of the in-cylinder pressure with crank angle for various βs of methane in fuel (n=1800 RPM, T=200 Nm) [77].

The author [77] noted that with an increase in methane fuel, the content of diesel pilot fuel decreases leading to a limited number of places where self-ignition can occur and from where the flame spreads through the mixture inside the cylinder. From Figure 2-17 it is evident that the first symptoms of knock combustion can be noticed when the SR of methane is larger than 50% ($\beta > 50\%$). The curve representing the highest SR of $\beta = 65.9$ suffered from knock combustion through the visible characteristic saw-tooth wave. Additionally, Nwafor [75] observed knock combustion characteristics at similar SRs during dual-fuel operation (diesel and natural gas). The author [75] also noted that dual-fuel operation suffered from long ignition delays having a Start Of Combustion (SOC) Before Top Dead Centre (BTDC) of 5.8° CA compared with 10.8° CA for pure diesel operation. It was concluded that in dual-fuel operation, during the extended ignition delays, the fuel system would still be delivering fuel, hence large quantities of premixed fuel would be present before auto ignition eventually occurs. Similar conclusions to those of Żółtowski [77] were reached by Nwafor [75]; the degree of knocking in DFE configurations is dependent upon the extent of the substitution fuel. Additionally, at higher engine speeds, this phenomenon is expected to be more pronounced due to extended ignition delays.

2.7 Solutions to Combustion Abnormalities

Due to experienced combustion abnormalities Riccardo [13] presented a list of appropriate mechanical designs which were derived upon the mechanisms of detonation. Some of which include:

- Designing a small combustion chamber and placing the sparking plug in appropriate position in order to reduce the length of the flame travel.
- Keeping the exhaust valves cool and positioning them far away from the end gases.
- By generating a consistent high intensity of turbulence in every cycle which results in a smooth operation and reduce the overall heat loss.

Besides these mechanical designs alternative fuels and other techniques specifically intake cooling can be used.

2.7.1 Knock mitigating fuels

Although not discovered by theory, from experimentation with multiple alternatives, both thallium and lead when introduced with gasoline are highly effective in reducing engine knock [13]. These elements can either have a finely divided metallic form or contain organic salts which are soluble in gasoline. In certain hydrocarbon fuels more than others, the effect of supressing detonation is more predominant. The presence of lead reduces the concentration of both peroxides and aldehydes. Riccardo [13] performed multiple tests on a "E6" variable-compression engine and compared the concentration of peroxides in parts per million. The addition of lead in high-octane petrol which typically detonate at CRs around 9.5:1 reduced the peroxide concentration from a maximum of 30 to only about 17 parts per million. Due to its toxicity, many developing countries have banned its use in gasoline as an antiknock agent [78]. Having said that, it is important to note that lead remains permitted and is still used as an anti-knock additive in the aerospace industry [79].

Zhuang et. al [80] investigated the effect of ethanol DI on knock mitigation. Ethanol is classified as a biofuel which is derived from sugary-rich plants, starchy material and other plant-based feedstocks [81]. Amongst the many advantages of a DI system in part-load fuel consumption and full-load torque output, it provides effective charge cooling. This charge cooling provides multiple benefits such as increase in volumetric efficiency, power output and primarily engine efficiency by mitigating engine knock. The authors [80] concluded that ethanol DI was more effective in reducing knock than GDI. Similar conclusions were drawn by Kasseris and Heywood [82] where the authors emphasised the fact that ethanol has a high latent heat of vaporisation when compared to traditional fuels such as gasoline. The configuration of a GDI engine results in a reduction of about 10 K in the charge temperature, which is approximately equivalent to an increment of 5 units in the RON. When ethanol is direct injected instead of gasoline, the latent heat of vaporisation is three times greater and the charge temperature reduces by 50K. Similar to ethanol, methanol is also a common practise used for mitigating detonation because of its high latent heat of evaporation [83]. This fuel is mostly utilised in SI engines due to its high-octane rating and lean flammability limits. Although implementing methanol in CI engines is highly advantageous, due to its lower NOx and sulphur compounds, ignition of this fuel is challenging because of its long ignition delay and low cetane number [83].

Alisaraei and Asl [81] performed a study on a six-cylinder CI engine which involves the comparison of pure diesel fuel with mixtures of ethanol concentrations of varying from 2 to 12%. Results showed that an average increase of 3.8% in torque and power was found when operating on a fuel blend with a concentration of 6% ethanol (D94E6) in comparison with diesel only operation. This increase in torque can be explained due to the increase in the percentage of dissolved oxygen. The percentage of dissolved oxygen in the fuel blends ranges from 0% for D100 (2% ethanol) to 3.97% for the D88E12 (12% ethanol) blend [84]. However, contrary to expectations, increasing concentrations of ethanol do not lead to improved performance. It was observed that by using the fuel blend of D88E12, the combustion quality declines due to the tendency of the mixture to become more heterogeneous [81]. Ethanol and diesel fuel cannot be precisely categorised as either miscible or immiscible. However, at higher concentrations of ethanol, they tend to be immiscible, which is influenced by the temperature of the mixture. Although, some ethanol can be dissolved in diesel fuel at room temperature, a decrease in temperature causes the solution to separate into two distinct phases [84]. In fact, it was reported that more shocks (sudden peak pressures) are experienced with increasing amounts of ethanol percentage. Such conclusion was based upon the increase of 4.75% in the RMS and 7.75% increase in kurtosis of the vibrations measured on the engine block [81]. The kurtosis value is dependent upon the fuel blend while the RMS value is more sensitive to the engine speed. Hence, despite the increase in power and torque, more shocks were created causing irregularities in engine performance. In addition, the author emphasised how the increase in ethanol concentration more than 8% in diesel fuel causes an increase in the ignition delay altering the in-cylinder pressure resulting in knock.

2.7.2 Cooling of intake air

Several studies [85] [86] [87] where performed on different engines to investigate the relation of charge intake temperature and engine knock. During natural gas operation, lean AFRs are commonly employed since such conditions mitigate the knocking tendency of the engine and facilitates the use of higher CRs [85]. However, as lambda increases, the flame speed and combustion temperature are decreased increasing combustion instability. During these lean operating conditions, NOx emissions increase and richer AFRs are forced to be used. Thus, additional measures need to be employed such as EGR or water injection. As seen in Figure 2-18, water has higher variations of

heat capacities with temperature when compared to N_2, O_2, CO_2 (remaining main components of exhaust gas).

Due to the high heat capacity of water, active cooling of the aspirated charge is commonly used due to the endothermal process of evaporating water inside the intake manifold. Consequently, the mixture temperature at the end of compression is also lowered, thereby reducing the knock tendency during middle and high-load operating points.

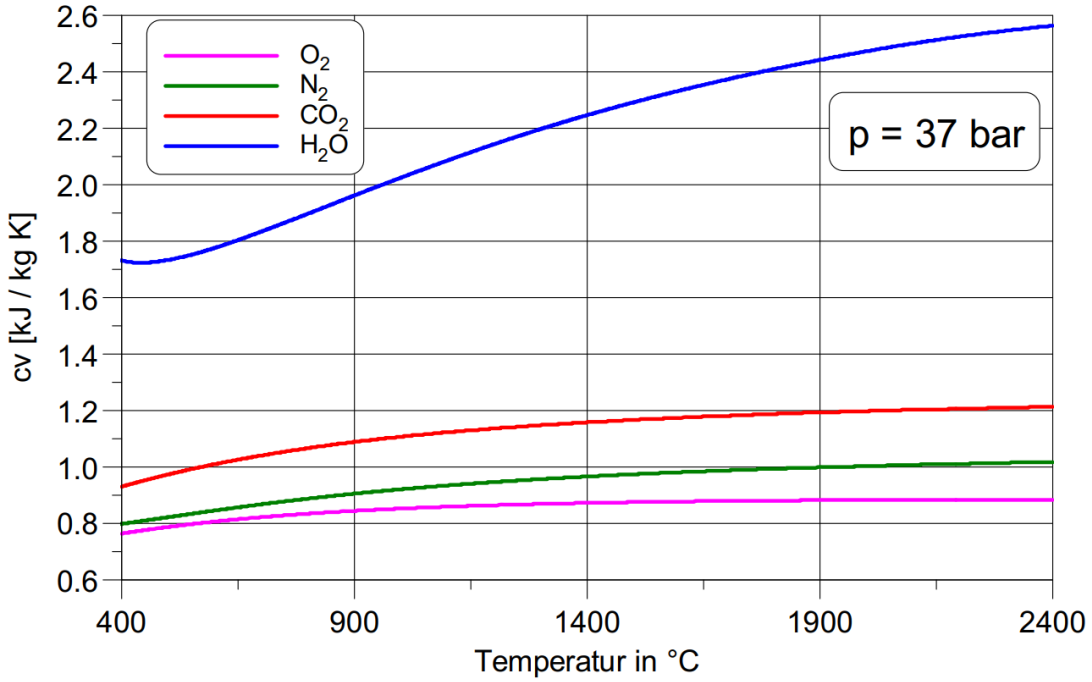

Figure 2-18: The variation of the specific heat capacity at constant volume of several gases with temperature when p= 37 bar [85].

Lakshmanan et al. [86] utilised water injection technology on an acetylene-diesel DFE. The implementation of this technology led to a decrease in brake thermal efficiency of 3% for the same acetylene flow rate when compared to diesel only operation. This was attributed to the decrease in combustion temperature at the end of the compression stroke which permitted a greater fuel portion to escape the combustion process as a result of quenching effects. At full load, the exhaust gas temperature decreased to 259 °C compared to 444 °C during diesel engine operation.

Additionally, Ghazal [87], performed a numerical analysis by using GT-Power professional software on a single cylinder dual-fuel CI model running on diesel and H_2 coupled with water injection. The author [87] reported an 8% decrease in the in-cylinder temperature resulting in a 50% reduction in NOx emissions. It was also reported that the delay period of maximum cylinder pressure increased with water injection due to the reduction of the inlet temperature. The maximum cylinder pressure was obtained when simulating engine speeds between 2000 and 3000 Revolutions Per Minute (RPM) and the lowest peak pressure occurred during the higher engine speeds. This phenomenon was attributed to insufficient time needed for cooling of the in-cylinder charge. Adnan et al. [88] reported similar outcomes and further confirmed that the presence of water in the mixture delays the onset of combustion consequently affecting the maximum in-cylinder pressure accordingly. Ghazal [87] emphasised the importance of correct timing of diesel injection when using water injection since it highly affects engine performance and emission characteristics. Further investigations were carried out by varying the engine speed and also the diesel injection timing. As seen from Figure 2-19a up to medium engine speeds (3000 RPM), the pressure increased and decreased rapidly with further increase in engine speed. Conversely, the combustion temperature appears to increase with engine speed driven by the enhanced flame propagation of the H_2 fuel flame and accelerated combustion. Based on Figure 2-19b, increasing the injection timing results in a corresponding increase in the maximum in-cylinder pressure as the combustion is shifted closer to TDC. This mitigates the expansion into the power stroke avoiding pressure losses observed with the -20° CA injection timing.

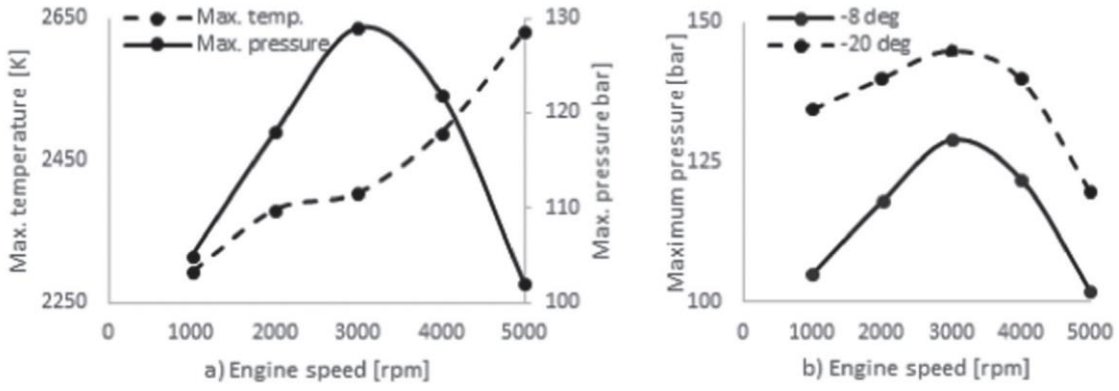

Figure 2-19: Effect of different engine speeds on a) cylinder temperature b) cylinder pressure [87].

The author [87] concluded that the implementation of the water-cooling technique necessitates adjustments in the diesel injection to reduce the chance of engine knock to take place. To increase the rate of change of the intake temperature, cryogenic liquids such as LNG can be used where the rate of heat transfer between the hot cylinder walls and the intake air is accelerated. This causes an increase in the effective polytropic exponent of compression. The primary consequence is a significant reduction in the final compression temperature, as a result of the lower initial temperature at the beginning of the compression stroke [41]. Consequently, the reduced compression temperature will negatively impact the fuel vaporisation during the initial stages of the delay period, leading to a delay in the diffusion of lighter fuel components into the air and in the initiation of pre-ignition chemical reactions. Karim [41] through thermodynamic calculations involving the combustion of methane and air, revealed that the flame temperature is less sensitive to lower reactant temperatures during stoichiometric and rich mixtures than when compared during lean mixture conditions, as demonstrated in Figure 2-20.

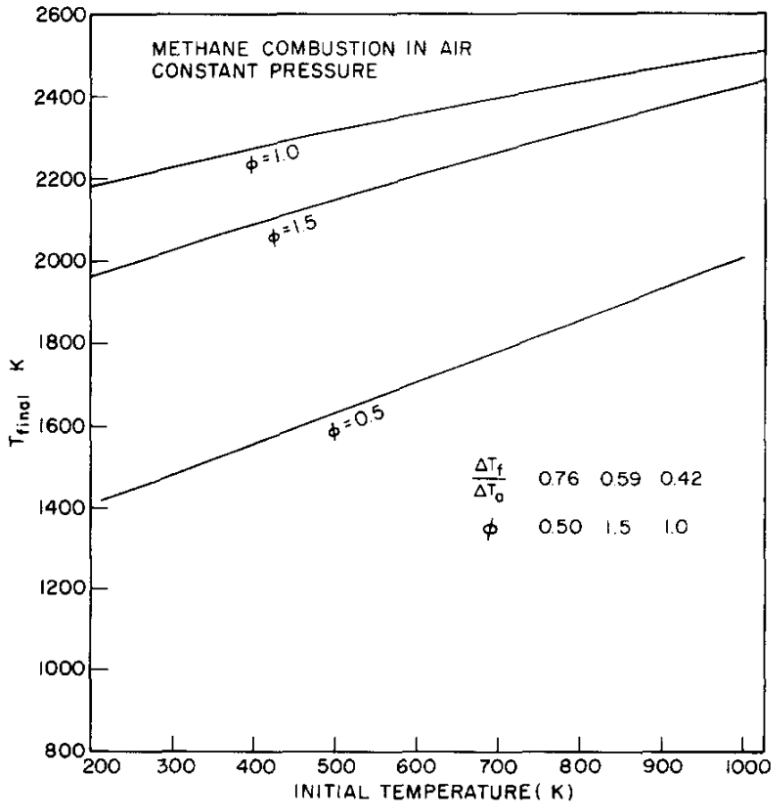

Figure 2-20: Variation of the calculated peak temperature after adiabatic combustion of a homogeneous methane-air mixture as a function of the initial mixture temperature for three Ø at atmospheric pressure [41].

Furthermore, Karim [41] observed that a reduction in the intake mixture temperature had significant adverse effects on the ignition of pilot fuel in air at low gaseous concentrations. The same amounts of pilot fuel that successfully ignited the same mixture at room temperature led to complete ignition failure during low-load operation with a cold intake temperature whereas successful ignition was achieved at high loads. The decrease in intake temperature adversely affects the already poor combustion efficiency associated with lean fuel mixtures. This reduction in combustion efficiency is attributed not only to the increased cooling effect of the cold intake temperature but also to the narrowing of the effective lower flammability limit. As a result, only a limited amount of gaseous fuel near the ignition sites participates in the combustion process, leading to the production of partial oxidation products and unburned gaseous fuel in the exhaust.

2.8 Recent University of Malta Research on Dual-Fuel and H_2 Engines

As internal combustion engines are shifting to H_2 fuels, one must properly analyse the combustion characteristics of this fuel. As evident in Section 2.5, numerous studies were presented and compared to investigate the combustion behaviour of this currently developing fuel. The results obtained from this dissertation will be compared to these studies. Currently at the thermodynamics laboratory at the university of Malta H_2 combustion tests were conducted on the J.A.P. 6 engine setup. Several different projects were performed on this engine however first H_2 tests were conducted by Portelli [89]. During the investigation a test matrix was compiled consisting of two fuels; H_2 and petrol, where power tests were performed to compare performance of the same engine whilst utilising different fuels. During the tests in-cylinder pressure measurements were conducted to allow the exploration of different combustion characteristics. Prior to these investigations, lean H_2 combustion was explored by Fenech [90] who improved the setup to allow proper indication of the fuel mixture during testing. Unlike Portelli [89], besides petrol and H_2, Fenech [90] made use of propane so that the gaseous fuel supply could be cross checked between propane and H_2 use. Similarly, power tests were performed at different fuel mixtures and comparison was made between the three different fuels. Continuation of this H_2 experimental investigation would provide substantial amount of knowledge to enable such a fuel to be implemented into the dual-fuel setup found at the same university. The dual-fuel setup was recently utilised by Azzopardi [91] who

performed multiple tests to investigate engine knock in DFEs while also highlighting optimal engine parameters for best efficiencies at different operating conditions. Simultaneously, Scicluna [92] made use of this knock detection system during the investigation of Water/AdBlue port injection while also studying the impact of this medium in reducing NOx. As outlined by Azzopardi [91] and Scicluna [92] engine knock is likely to take place when operating in loaded conditions; increasing of in-cylinder pressure and temperature [75] as depicted in Figure 2-21 [93].

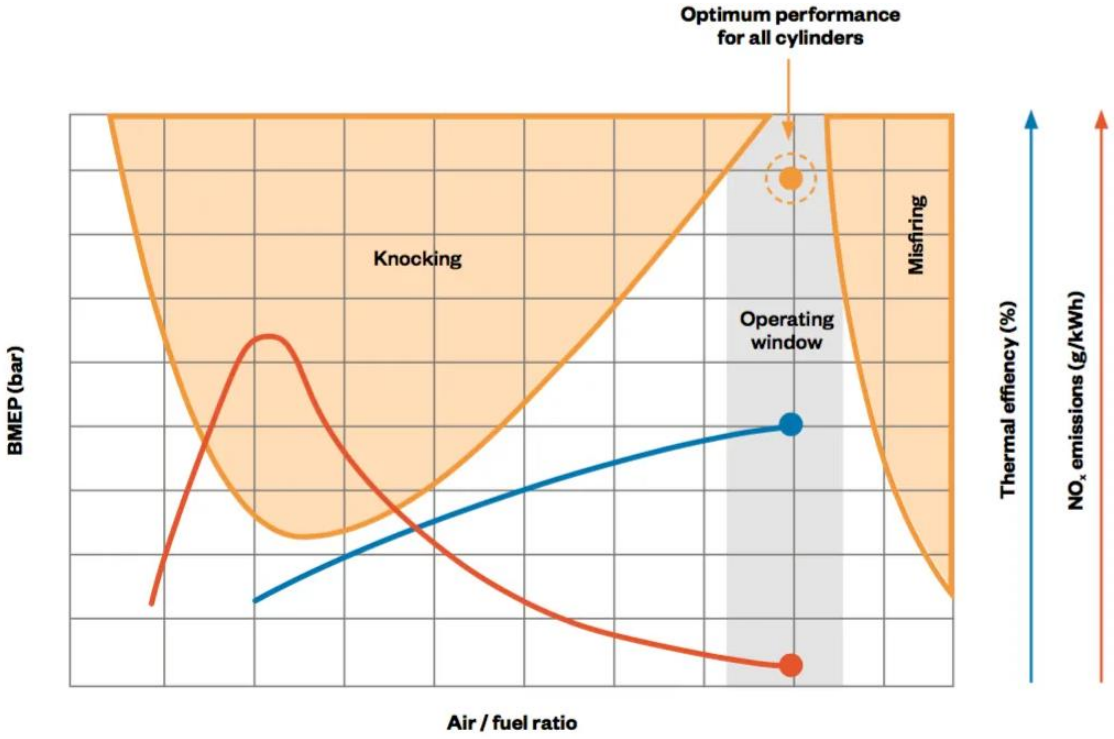

Figure 2-21: Operating window of a DFE showing BMEP versus air/fuel ratio with regions of knock, misfire and optimal combustion [93].

Among the various parameters influencing engine knock combustion, peak combustion temperature is a key factor. Numerous studies [83] [82] have demonstrated that the reduction in knock observed with different fuels is attributable to variations in their latent heat of vaporisation, which directly impacts the peak combustion temperature. With the rapid growth in the use of LNG within the power industry, especially in heavy-duty vehicles, there is an increasing trend toward adopting LNG as a fuel for the internal combustion engine [27]. Although, this approach gives the opportunity to utilise the high latent heat of evaporation of LNG, which exceeds that of the conventional petrol and diesel fuels, the common practise is to first convert it into gaseous state before injecting it. This exact setup was built at Malta's Dellimara power plant, where LNG stored on the floating storage unit is converted into natural gas and then supplied to the D3 and

D4 power stations [94]. In addition, Procházka et al. [95] investigated liquid propane injection; however, the injector nozzle was electrically heated to vaporise the fuel, which eliminated its ability to cool the combustion temperature. On the contrary, if the fuel is injected directly into the combustion chamber or into the intake manifold in its liquid form rather than in its gaseous state, it would absorb heat from the surrounding environment during vaporisation. This phase change reduces the combustion temperature, which helps to suppress engine knock as evidently seen from numerous studies mentioned in Section 2.7.2.

2.9 Review Rationale

The literature review comprehensively explored the opportunities and challenges associated with dual-fuel engines in the engine industry, emphasizing their potential during the transitional phase toward H_2 integration. A significant research gap was identified regarding the use of cryogenic liquid fuel injection specifically LNG to harness the latent heat of evaporation as a strategy for knock reduction in dual-fuel engines. This gap aligns with findings from previous studies indicating that knock occurrence at high engine loads is strongly influenced by intake air temperature, which can be effectively lowered through the evaporative cooling effect of the injected liquid fuel. Such insights motivated the experimental focus on liquid fuel injection techniques, particularly the use of liquid propane, to leverage these knock-mitigating effects. This approach aims to improve engine performance and durability while facilitating smoother transitions toward H_2 integration in dual-fuel engine technologies.

A considerable emphasis was placed on H_2 combustion, specifically the importance of optimising spark timing for achieving optimal performance in H_2-fuelled SI engines. Investigations into burn duration, heat loss, and blow-by effects were also conducted. This comprehensive review laid the foundation for the experimental work presented in this dissertation, which involves the study of H_2 combustion in SI engines compared to petrol and propane. Notably, the review highlighted evidence of the need of variation of spark timing (even late spark timing in the region of ATDC) prompting the development of a zero-dimensional combustion model to better explain this phenomenon. This research was pivotal for expanding the understanding of H_2 combustion and will facilitate the effective integration of H_2 into future dual-fuel engine systems.

Chapter 3. Analytical Methods for Combustion Characterisation

This chapter presents analytical methods used to analyse selected aspects of combustion obtained from experiments. Specifically, it discusses the used theories related to combustion characterisation derived from the post-processing of the H_2 tests. Within this chapter, related theoretical approaches are compared and critically evaluated, leading to the selection of the most suitable theory to be applied to achieve the results presented later in Chapter 6.

3.1 Net Heat Release Rate

The net HRR method presented by Heywood [49] and Stone [96] was employed by using (3.1). The net HRR analysis is used in an ICE for quantifying the energy released (with crank angle) during combustion. It is applied to both SI and CI engines [96]. This method calculates the rate of energy required by the cylinder to generate the observed pressure variations, based on well-established assumptions regarding the combustion process. One assumption refers to the crevice regions such as the volume between the pistons, rings and cylinder walls which amounts to a few percent of the clearance volume. Although the gases in these crevices are cooled close to the wall temperature, resulting in increased density, their relatively small volume means that heat transfer within these crevices is typically neglected [49]. Another assumption is that the contents inside the combustion chamber are treated as a single zone; reactants and products are completely mixed. Furthermore, there are no differences in the properties of the reactants and products, and the temperature is assumed to be uniform throughout the system [96].

When plotting the net HRR, the polarity of the curve is initially negative, implying that heat is being transferred to the cylinder surfaces. From such a curve, one can determine the position of ignition, which occurs near the point of minimum cumulative heat release. The minimum cumulative heat release occurs at the zero-crossing of the net HRR which ultimately corresponds to the SOC in a diesel engine due to the rapid combustion of the pre-mixed reactants [96]. However, in SI engines the minimum net HRR is not well-defined due to the initial low rate of combustion. As combustion nears its end, the heat transfer to the combustion chamber exceeds the heat generated by the

combustion process. As a result, the net HRR decreases, indicating that the total amount of heat being released begins to diminish. This phenomenon can be employed to indicate the point at which combustion will be completed. The net HRR ($\frac{dQ_{net}}{d\theta}$) presented in (3.1) [97] is defined as the rate of energy released during combustion. Where p represents the in-cylinder pressure and V denotes the instantaneous cylinder volume, where all parameters are a function of crank position (θ). The cylinder volume was calculated by using the crank-slider relationship presented in (3.2) [98].

$$\frac{dQ_{net}(\theta)}{d\theta} = \frac{\gamma}{\gamma-1}p(\theta)\frac{dV(\theta)}{d\theta} + \frac{1}{\gamma-1}V(\theta)\frac{dp(\theta)}{d\theta} \tag{3.1}$$

Regarding the specific heat ratio (γ), Heywood [49] suggests the use of a polytropic index value of 1.3 instead of γ for most fuels. The numerical differentiation of volume and pressure with respect to crank angle was determined by using (3.3) and (3.4), respectively.

$$V(\theta) = V_c + \frac{\pi}{4}{d_B}^2\left(L + R - R\cos\theta - \sqrt{L^2 - R^2\sin^2(\theta)}\right) \tag{3.2}$$

Where V_c is the clearance volume, d_B is the bore diameter, L is the connecting rod length ($L = 2a$) and $R = \frac{L}{a}$ where a is the crank radius

$$\frac{dV(\theta)}{d\theta} = \frac{(V_{i+1} - V_{i-1})}{(\theta_{i+1} - \theta_{i-1})} \tag{3.3}$$

$$\frac{dp(\theta)}{d\theta} = \frac{(p_{i+1} - p_{i-1})}{(\theta_{i+1} - \theta_{i-1})} \tag{3.4}$$

Equation (3.5) is another approach which was developed by Pipitone and Beccari [72]. As correctly observed by Caruana [73], (3.5) is an improvement over (3.1), as it accounts for energy losses due to blow-by effects by incorporating an additional term that deducts this energy from the heat released by the fuel, resulting in a more accurate representation.

$$\frac{dQ_{net}(\theta)}{d\theta} = \frac{\gamma}{\gamma-1}.p(\theta).\frac{dV(\theta)}{d\theta} + \frac{1}{\gamma-1}.V(\theta).\frac{dp(\theta)}{d\theta} - \frac{\gamma(\theta)}{\gamma-1}.\frac{p(\theta)V(\theta)}{m_{air}(\theta)}.\frac{dm_b(\theta)}{d\theta} \tag{3.5}$$

Where, the blow-by gases (m_b) are approximated by using (3.6) [73], representing the flow through an orifice during chocked conditions.

$$\frac{dm_b(\theta)}{d\theta} = A_{orifice}\sqrt{\gamma . m_{air}\frac{p(\theta)}{V(\theta)}.\left(\frac{2}{\gamma+1}\right)^{\frac{\gamma+1}{\gamma-1}}} \; when \; \left(\frac{p_{crank\ case}}{p}\right) < \left(\frac{2}{\gamma+1}\right)^{\frac{\gamma}{\gamma-1}} \quad (3.6)$$

It should be noted that Rogers [97] presented a similar relationship for net HRR presented in (3.7), as outlined in the AVL Engine Indicating Handbook [99], with the primary difference being of a constant K multiplier.

$$\frac{dQ_{net}(\theta)}{d\theta} = \frac{K}{\gamma-1}\left(\gamma p(\theta)\left(\frac{dV(\theta)}{d\theta}\right) + V(\theta)\frac{dp(\theta)}{d\theta}\right) \quad (3.7)$$

The K multiplier is introduced because when (3.5) is used all surface losses are neglected and the displayed net HRR is lower than the actual gross energy released (by approximately 20%). This heat loss is also discussed by Heywood [49] who illustrated this concept through Figure 3-1.

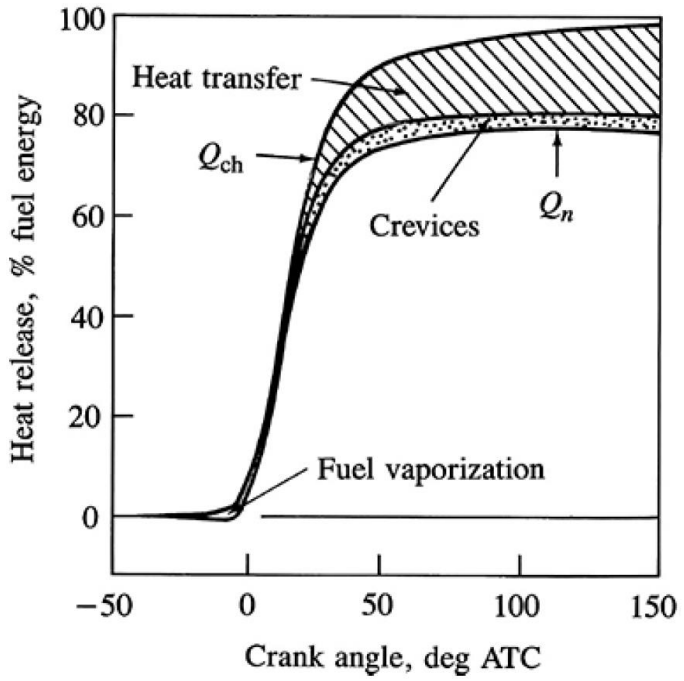

Figure 3-1: The variation of the gross (upper line) and net heat-release (lower line) profiles during combustion with crank angle, showing relative magnitude of heat transfer, crevice and fuel vaporisation and heat-up effects [49].

The author [49] comments that the injected fuel requires less than 5% of the total calorific value to undergo phase change and heat up to typical compressed air temperatures. However, when heat transfer is integrated over the entire combustion period it accounted for 10 to 25% of the total heat released.

3.2 Energy Losses

When evaluating the engine's energy losses, unburnt fuel, blow-by gases, and heat loss together make up the total energy loss. This parameter provides valuable insight into the portion of energy which is lost instead of being converted to power. Two different approaches were used.

The first approach, described in (3.8) in which the energy lost is quantified by subtracting the energy lost with the exhaust and the power based upon the indicated work from the amount of energy available from the injected fuel. This has to be done to allow comparison between the two approaches. Otherwise, if the torque obtained from the load cell is used, the mechanical inefficiencies of the system would also be subtracted. The brake torque measured by the load cell is the effective torque transmitted to the load which captures the actual usable power output. The load cell configuration and setting up is described by Portelli [89].

The second approach presented in (3.9) involves the subtraction of the cumulative net HRR from the total energy stored in the injected fuel. To calculate the cumulative net HRR, the approach presented in (3.5) is ideally to be used as previously described in Section 3.1.

$$Energy\ Loss = Heat\ generated\ by\ the\ fuel - Heat\ lost\ from\ exhaust - Indicated\ work$$

$$Energy\ Loss\ = \dot{m}_{fuel}H - \left(\dot{m}_{fuel} + \dot{m}_{air}\right)C_p(T_{ambient} - T_{exhaust}) - \frac{N * W_i}{60} \quad (3.8)$$

$$Energy\ Loss = \dot{m}_{fuel}H\ - \sum_{i=ignition}^{i=end\ of\ combustion} \left(\frac{dQ(\theta)}{d\theta}\right)_i \quad (3.9)$$

Where $\dot{m}_{fuel}$ & $\dot{m}_{air}$ are the mass flow rate of fuel and air respectively, $C_p$is the specific heat at constant pressure, N is the RPM and τ is the torque. $T_{ambient}$ & $T_{exhaust}$ are the temperatures of ambient and exhaust conditions respectively.

It is important to note that the calorific value (H) employed in both approaches is the Lower Heating Value (LHV) as the combustion products exiting the engine contain water in the vapour phase. Consequently, the latent heat of vaporisation is not recovered, making the LHV a more appropriate measure than the Higher Heating Value (HHV) as it more accurately reflects the energy available during engine combustion.

3.3 Start and End of Combustion

The SOC cannot be simply defined as the ignition advance due to the unavoidable ignition delay [49]. Instead, the SOC can be approximated by analysing the net HRR curve, specifically near the minimum point of the cumulative net HRR. The minimum cumulative heat release occurs at the zero-crossing of the net HRR which ultimately corresponds to the SOC in a diesel engine due to the rapid combustion of the pre-mixed reactants [96]. Similarly, the SOC as stated by Heywood [49] is defined as the "change in slope of the heat-release rate (from negative to positive) calculated from the cylinder pressure data" which corresponds to the minimum net HRR. Furthermore, the End Of Combustion (EOC) can be approximated using the same principle. As combustion nears its end, the heat transfer to the combustion chamber exceeds the heat generated by the combustion process. As a result, the net HRR decreases, indicating that the total amount of heat being released begins to diminish. This phenomenon can be employed to indicate the point at which combustion will be completed [96].

3.4 Ignition Delay

The ignition delay can be determined through the use of (3.9), which relies on the identification of the SOC and ignition advance values. The SOC can be identified through the change in gradient of the net HRR as discussed in Section 3.3. Then through the ignition advance values the ignition delay can been calculated accordingly. Jet [100] mentions that several authors found ignition delay differently but ended using the following approach presented in (3.10) where the SOC was identified as the point where the net HRR turned positive.

$$Ignition\ Delay = Ignition\ Advance - Start\ of\ Combustion \tag{3.10}$$

Ignition delay is influenced by multiple parameters and experimental results have shown that it decreases with increasing engine speed, as well as with increases in pressure, temperature, and CR [101].

3.5 Mass Fraction Burned

The most influential and widely accepted research on instantaneous energy release derived from the pressure curve was conducted by Rassweiler and Withrow in the mid-1930s. Their experimental study presented in the 1938 technical paper [102] used high-speed photography to capture the progression of the combustion flame during a single engine cycle, correlating these images with cylinder pressure data over time and crank angle. Rassweiler and Withrow developed a method to distinguish between the pressure changes within the cylinder resulting from combustion and those arising from changes in cylinder volume. By isolating the pressure change attributable solely to the combustion process and then summing and normalising this value, a direct correlation with the percentage of the fuel charge burned (by mass) at each corresponding crank angle or time interval was found which is presented in (3.11).

$$Fractional\ mass\ "inflamed" = \frac{P_t^{\frac{1}{n}}V_t - P_{ti}^{\frac{1}{n}}V_{ti}}{P_{tf}^{\frac{1}{n}}V_{tf} - P_{ti}^{\frac{1}{n}}V_{ti}}\ [102] \tag{3.11}$$

The subscripts indicate the different stages of combustion: the subscript t denotes the conditions during combustion, the subscript tf denotes the state at the end of combustion, and the subscript ti denotes the conditions at ignition

An alternative approach was derived and proposed by Pipitone and Beccari [72] which can be used to compare the results with those obtained from the Rassweiler and Withrow approach [102]. The authors [72] started from the first law of thermodynamics applied to the in-cylinder mass:

$$dQ_{comb} + dQ_{ht} - pdV = dU = m_{air}\, C_v dT \tag{3.12}$$

Where Q_{comb} is the combustion energy, dQ_{ht} is the heat lost to the surroundings and C_v is the specific heat capacity at constant volume

$$dQ_{comb} = m_{fuel}Hdx_b \quad \& \quad dU = \frac{pdV+Vdp}{\gamma-1} \qquad (3.13)\ \&\ (3.14)$$

Where m_{fuel} is the mass of fuel, H is the calorific value and x_b is the MFB

Therefore

$$dQ_{net} = m_{fuel}Hdx_b + \ dQ_{ht} = \frac{\gamma(pdV+Vdp)}{\gamma-1} \qquad (3.15)$$

If no heat is assumed to be lost by the engine to the surroundings; $dQ_{ht} = 0$ the fraction mass burnt for each cycle can be found from:

$$\sum dx_b = \sum \frac{\gamma(pdV + Vdp)}{(\gamma - 1)m_{fuel}H} \qquad (3.16)$$

When comparing (3.11) to the approach adopted by Pipitone and Beccari (3.16), it is important to recognize their key differences which can be visibly detected through Figure 3-2. The Rassweiler and Withrow method (blue curve) models the progression of the combustion process up until it reaches a complete burn (unity), relying on the pressure rise caused by combustion and as Heywood [49] noted, it is proportional to the amount of fuel chemical energy released rather than the mass of mixture burned. This relationship incorporates heat transfer effects through the use of a polytropic index (n), which must be appropriately selected as it differs from γ and varies throughout the different stages of the combustion cycle. When making use of (3.11) Heywood [49] emphasised on the importance of accurately choosing the polytropic exponent due to its variation during combustion. Additionally, Mittal et al. [103] emphasised on how important the EOC is accurately identified to minimise the uncertainties associated with the MFB calculations. Mittal et al. [103] made use of two models where one made use of a least-squares fit algorithm and the other is found through location of the peak net pressure to find the exact location of the EOC. The Rassweiler and Withrow method would assume that the EOC takes place at the point when the exhaust valve opens, which may not accurately represent the true EOC.

In contrast, Pipitone and Beccari's approach [72] (red curve) based on (3.16) utilises pressure and volume data but further incorporates the mass of fuel and its calorific value employing γ instead of n, as it is derived directly from the first law of thermodynamics. It was concluded that any results derived from the Rassweiler and Withrow method during the post processing analysis, specifically the EOC pressure and volume values would correspond to the crank angle identified by the peak MFB value obtained using Pipitone's approach. Furthermore, from Figure 3-2, the Rassweiler–Withrow method reaches unity by definition since the equation is self-normalizing. The Pipitone and Beccari method never reaches unity, as losses prevent full conversion of chemical energy to pressure rise. This method only reaches unity in an ideal, loss-free, perfectly complete combustion—which real engines never achieve. This difference in the maximum MFB between the two curves highlights this loss of energy of approximately 30% as reported by Heywood [49] and Rogers [97] in Figure 3-1.

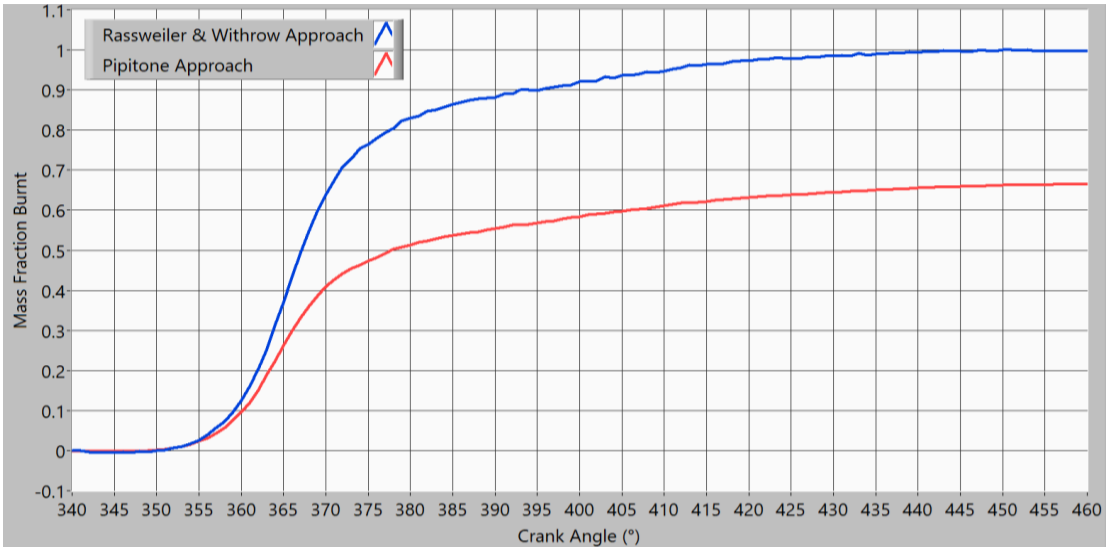

Figure 3-2: MFB against crank angle during petrol experimentation with a MAP of 95 kPa.

3.6 Locations of CA10, CA50 and CA90

The combustion characterisation curve, also referred to as MFB profile or history, is often described in numerical terms by using the terms Crank Angle to 10% MFB (CA10), the Crank Angle to 50% MFB (CA50) and the Crank Angle to 90% MFB (CA90). These computations were computed on both MFB approaches; the Rassweiler and Withdraw and Pipitone's methods described in Section 3.4. For both different methods, the crank angles corresponding to CA10, CA50, and CA90 were found by finding when the MFB values which reached 0.1, 0.5 and 0.9 respectively.

The CA50 location is critical for MFB profile analysis, as it depends on parameters such as burn velocity and spark timing [49]. Most combustion research examines CA50 since it gives an insight to the work output produced. The TDC position is critical to prevent any expansion work during heat addition, ensuring that all the heat input is manifested as an increase in the pressure and temperature of the gases, which are subsequently utilised during the expansion stroke. However, this idealised theory cannot be used in practice as Heywood [60] notes: "the real combustion process occupies a finite crank angle period between about 20 to 70 crank angle degrees". Additionally, Heywood implies that in reality, the 50% crank angle position shifts from TDC for MBT timing, and this angle shift is referred to as the "combustion retard" parameter. For a wide range of engines the centre of combustion takes place at 5 to 7° CA ATDC [49] which is confirmed by a number of authors [104], [105], [106].

A comprehensive analytical study on the evaluation of the optimal combustion phase in SI engines performed by Beccari et al. [107] investigated this well documented phenomenon previously described by Heywood [60]. The authors [107] first considered an ideal adiabatic engine in which it was demonstrated that the optimal phase of the combustion depends on the "shape" of the HRR curve. The commonly used Wiebe function was compared with two scenarios: one symmetrical and one asymmetrical heat release profile, both defined relative to the midpoint of the combustion angle. The analysis showed that if the HRR is perfectly symmetrical about its maximum, the best spark timing would position the midpoint of the combustion arc at the TDC. The authors [107] also highlighted that a linear heat release (which was initially adopted in the 0D model) has a symmetrical derivative, meaning a constant combustion velocity which is not possible in a SI engine.

However, when the combustion is delayed by an angle θ compared to a profile which is symmetrically centred at TDC, for each piston position lower gas temperatures are created when compared to an advanced combustion profile. This reduction in gas temperature leads to diminished heat transfer to the chamber walls, thereby decreasing the overall heat subtracted from the gas improving cycle efficiency [107]. As a result, the optimum combustion phase is shifted several degrees after TDC.

In addition to thermal considerations, the authors [107] accounted for mechanical friction losses, specifically those arising from piston-cylinder interactions and neglected any losses caused by the friction in the loaded bearings or the power needed to drive the engine accessorises. Through the analysis, Beccari et al. [107] concluded that the optimal combustion phase is delayed by approximately 6° CA which are caused due to heat exchanges with the chamber walls and an additional 1° CA delay is resulted from friction losses. These findings are in strong agreement with the prementioned conclusions reported by Heywood [60].

Wiseman [108] also performed an experimental and simulation investigation of the optimum location of 50% mass burnt. Similar to Beccari et al. [107], the main influences of burn duration, heat loss, magnitude of heat released, manifold pressure and engine dimensions were varied. It was concluded that change in engine geometry had no effect on the optimum 50% mass burn location indicating that the rate of fuel burning is dominant over the volume changes. Similar conclusions to Beccari et al. [107] were drawn were heat rejection is more significant because it directly influences the heat energy available to produce work. As commented by Beccari et al. [107], the amount of heat lost at any instant is dependent on the gas temperature which distorts the pattern of the effective heat release and alters the location of the 50% mass burnt. Furthermore, burn duration also influences the optimum burn location because it directly affects the burn shape. A fast burn can release more energy near TDC without incurring large compression losses. The increase in energy release at TDC will produce a higher cylinder pressure, due to the smaller volume and will produce more work done. Therefore, a fast-burning charge will have an optimum 50% mass burnt location nearer to TDC than a mixture whose combustion is slow.

3.7 Burn Duration

The burn duration can be calculated by subtracting the end-of-burn angle from start-of-burn angle [97]. Specifically, the burn duration was found by subtracting the CA10 from the CA90 as recommended by Heywood [49] since such choice of angles avoid the challenges of precisely identifying the very beginning and end of the combustion curve, which are often difficult to define accurately. This burn duration approximation is referred to as the fast burn duration since in reality the burn duration would be longer [108]. As discussed in Section 3.4, since two different approaches were used to obtain

the MFB, the fast burn duration was found for the two approaches and compared accordingly. Another interesting approach developed by Bayraktar and Durgun [109] is presented in (3.17) where the CA50 location can be used to estimate the burn duration.

$$\Delta\theta_b(\theta_s) = 1.0685 - 0.2902\left(\frac{\theta_s}{\theta_{s1}}\right) + 0.2545\left(\frac{\theta_s}{\theta_{s1}}\right)^2 \quad (3.17)$$

Where $\Delta\theta_b$ is the burn duration and θ_s is the spark ignition angle

3.8 Zero Dimensional Models

Recently developed engine software such as Riccardo's Wave and Gamma Technologies' GT Power are widely used for engine performance analysis. In these software programs, it is common for the MFB or HRR to be imposed or modelled using empirical functions such as the Wiebe function [110], rather than being directly predicted from first principles by the software itself. These programs typically simulate combustion based on user-defined combustion models or inputs derived from experimental or literature data to replicate realistic combustion behaviour. To simulate such behaviour, these software programs typically employ a zero-dimension (0D) modelling strategy. This simplified approach treats the combustion chamber as a single control volume without spatial resolution since it does not support the concept of space [110]. One advantage of 0D models is their ease of use and their computationally efficient [111]. The model performs mass and energy balances over the entire combustion chamber or engine volume, assuming uniform properties throughout. Hence, at each time step a single value of pressure, temperature and other thermodynamic properties is calculated for the trapped mass within the cylinder. Such calculations are consistent with the first law analysis of a non-flow system as the mass within the cylinder is considered stagnant. Such models are commonly used by various authors [110], [112], [111] as it simplifies the system to a lumped parameter model focusing on averaged quantities rather than spatial variations [113]. Therefore, a 0D model was developed to investigate the optimal CA50 for H_2 fuel, as described in Section 4.5. The results from this model were later compared with those obtained from post processing of experimental data.

3.9 Closing Remarks

Various analytical methods for combustion characterisation were studied and evaluated to establish approaches for post-processing and interpretation of experimental H_2 combustion data. During this evaluation, the most appropriate analytical techniques were selected which would later allow direct comparison with traditional fuels. In some cases, multiple methods were employed simultaneously to cross-validate results and enhance confidence in the outcomes. This comprehensive assessment was essential for identifying common combustion analyses, such as the net HRR, ignition delay and burn duration all of which are critical in highlighting the indicative combustion behaviour of H_2. Making use of these combustion parameters will facilitate meaningful comparisons with existing literature and support further optimisation of H_2 combustion strategies.

Chapter 4. H_2 Experimental Investigation

As part of the experimental investigation to support the transition of H_2 in DFEs, tests were performed on a dedicated H_2 engine operating under lean conditions. These tests were designed to complement the primary research focus by providing insights into combustion dynamics specifically during lean mixtures. These operating conditions are possible through the wide flammability range of H_2 [114] which is a key aspect to be incorporated in future applications of DFE.

Understanding how to manage lean combustion conditions with H_2 will be crucial for integrating this fuel into dual-fuel engines, where maintaining consistent combustion across varying fuel ratios is essential. H_2 engine tests were conducted to gather and process data on several parameters including the net HRR, ignition delay, brake thermal efficiency and compared to the same parameters extracted during operation with traditional fuels. The experiments were conducted using the existing H_2 engine setup depicted in Figure 4-1.

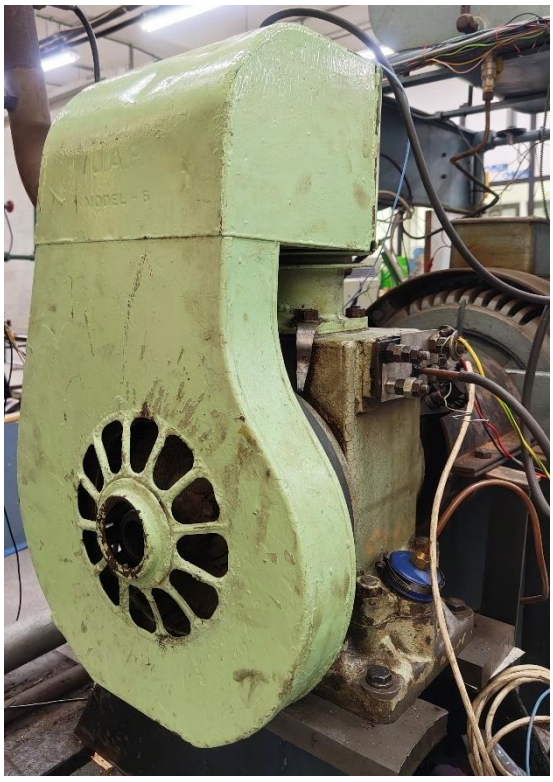

Figure 4-1: J.A.P model 6 engine used during H_2 testing.

4.1 Previous Engine Projects and its Specifications

The H_2 engine setup is composed of a single cylinder J.A.P. 6 engine whose specifications are listed in Table 4-1 [115].

Table 4-1: J.A.P. 6 engine specifications.

Model	6
Number of cylinders	1
Capacity (c.c.)	588
Stroke (mm)	102
Bore (mm)	86.1
Compression Ratio	5.36:1
Valve train	Side valve

Several projects were performed on this engine including water injection and combustion photography however the recent major alterations were performed by Portelli [89] who converted the engine to work on both H_2 and petrol fuels. During this conversion the engine was equipped with multiple sensors both on the engine itself and also in its surroundings to detect any H_2 leaks. This leak detection system can also prevent the H_2 engine setup from operating until certain safety detection criteria are met ensuring safety at all times. Portelli [89] utilised LabVIEW software to prepare VIs which were used for the acquisition of slow data during experimentation and for the post processing of in-cylinder pressure measurements. Last modifications were done by Fenech [90] where the H_2 setup was improved to aid in the H_2 experimentation. The main improvements where targeted to correct the method of AFR determination. This was done through proper determination of the H_2 flow rate through the Hercules injector

(3bar) which was additionally supported with theoretical analysis. Another main improvement was the installation of a petrol catalyst which served as a Laminar Flow Element (LFE) to measure the Mass Airflow (MAF). Effort was also put to convert the existing PFI to a DI system however acquisition of appropriate H_2 injector was unsuccessful.

4.2 H_2 Engine Setup Alterations

4.2.1 Existing mass airflow measurement scheme, laminar flow element

During the engine setup improvements done by Fenech [90], three independent methods were implemented to determine the air-to-fuel ratio during H_2 operation. Two exhaust gas oxygen sensors were installed to measure the oxygen content in the exhaust, enabling the determination of the air-to-fuel ratio through combustion analysis. An alternative technique involved the previously mentioned petrol catalyst which was calibrated and integrated into the setup to function as an LFE, and this component was referred to as an in-house viscous flow meter. This component was useful to determine the airflow of the engine during H_2 operation which combined with the injected fuel quantities meant that the AFR could be determined. Although the LFE is commonly used in engines due to the linear relationship between pressure drop and measured flow rate [116], a quadratic equation was implemented nevertheless to account for entry length effects. It was noted that the entrance length of the air flowing through the channels of the in-house viscous flow meter was significant (10 cm) when compared to the total length of the catalyst (16 cm). Fenech [90] highlighted the fact that two empty reservoirs had to be installed on the setup to mitigate the pulsation caused by the single cylinder J.A.P. 6 engine. These pulsations are important to be dampened to create a steady measurement as emphasised by Rathakrishnan [117]. Despite these considerations, Fenech [90] commented that the developed air measurement scheme involving the in-house viscous flow meter proved to be effective.

4.2.2 New mass airflow measurement scheme, critical flow orifice

For a certain ratio of the pressure upstream and downstream of an orifice, the velocity at the orifice becomes sonic, a condition known as chocked or critical flow [107] [118]. According to chocked flow theory, once critical flow occurs in a passage of a gaseous fluid, the mass flow rate depends solely on the absolute pressure and temperature upstream becoming unaffected by any changes in downstream conditions [116]. From

the extensive investigation carried out by Laurantzon [118] this theory when applied through critical flow nozzles is ideal for measuring pulsating flow. In fact, Kastner et al. [119] utilised this theory to measure the flow of engine exhaust.

To further improve the air measurement scheme on the H_2 engine setup and ascertain accurate calculation of the air to fuel measurement, a critical flow orifice scheme was used. This scheme was used as a replacement for the in-house viscous flow meter system previously discussed. When using the critical orifice air measurement scheme, calculation of the engine's airflow was done through (4.1). This approach effectively addresses and mitigates concerns regarding the setup proposed by Fenech [90], including the high entry losses observed within the in-house viscous flow meter and the damping scheme employed for airflow regulation.

As already mentioned, to utilise the critical orifice measurement scheme, chocked conditions have to be created by using compressed air at the upstream of the orifice. These conditions allow the critical orifice to regulate the MAF through variations in the upstream pressure and orifice area making it completely unaffected by changes in downstream pressure. It was decided that an upstream pressure of 3 barg was assumed to be within the range of the air pressure system of the thermodynamics laboratory. Therefore, correct sizing of the orifice diameter was essential but first the mass airflow ($\dot{m}_{air}$) of the engine must be calculated through:

$$\dot{m}_{air} = \rho \eta_v V_s \frac{N}{2} n_{cyl} \text{ [120]} \tag{4.1}$$

Where the density (ρ) was taken to be 1.2 kg/m^3 at 1 bar absolute, η_v is the volumetric efficiency assumed to be 100%, the engine speed (N) taken to be 1250 RPM, V_s is the displaced volume and n_{cyl} is the number of cylinders.

$$\dot{m}_{air} = 1.2 \times 1 \times \frac{\pi \times 0.0861^2 \times 0.102 \times 1250}{4 \times 2 \times 60} \times 1 = \mathbf{7.47 \times 10^{-3}\ kg/s}$$

For a chocked flow (4.2) [116] was used.

$$\dot{m}_{air} = \frac{c_D A_t p_0}{\sqrt{R T_0}} \gamma^{\frac{1}{2}} \left(\frac{2}{\gamma + 1}\right)^{\frac{\gamma+1}{2(\gamma-1)}} \tag{4.2}$$

Where A_t is the throat diameter, p_0 is the upstream pressure, T_0 is the upstream temperature, R is the air gas constant and the coefficient of discharge $c_D = 0.982$, according to the diameter ratio of 0.15 ($\beta_d = d/D$) [121] [49]

$$7.47 \times 10^{-3} = \frac{0.982 \times \pi \times {d_t}^2 \times 4 \times 10^5}{4 \times \sqrt{287 \times (25 + 273)}} 1.4^{\frac{1}{2}} \left(\frac{2}{1.4 + 1}\right)^{\frac{1.4+1}{2(1.4-1)}}$$

$$d_t = 3.22 \times 10^{-3} m \approx \mathbf{3\ mm}$$

The nozzle was machined as seen in Figure 4-2 and an O-ring was used to ensure no air leakage occurred and installed onto the setup accordingly.

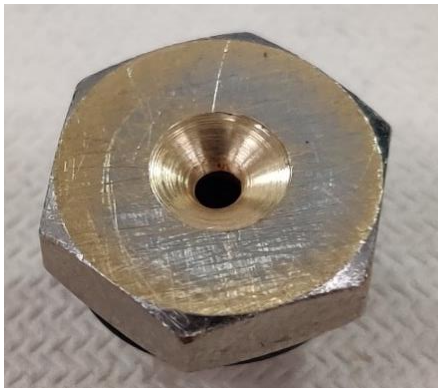

Figure 4-2: The chocked flow nozzle

To consistently monitor the upstream pressure an Omega pressure transducer which have an accuracy of 1% (PXM 319-015G17) was installed, as depicted in Figure 4-3A. The transducer was calibrated using a dead weight tester setup, illustrated in Figure 4-3B. The calibration equation of the curve depicted in Figure 4-4 was implemented into the LabView software to calculate the airflow first and subsequently calculate the AFR during testing. To regulate the intake air during experimentation, a pressure regulator was integrated into the setup and installed upstream of the pressure transducer shown in Figure 4-5.

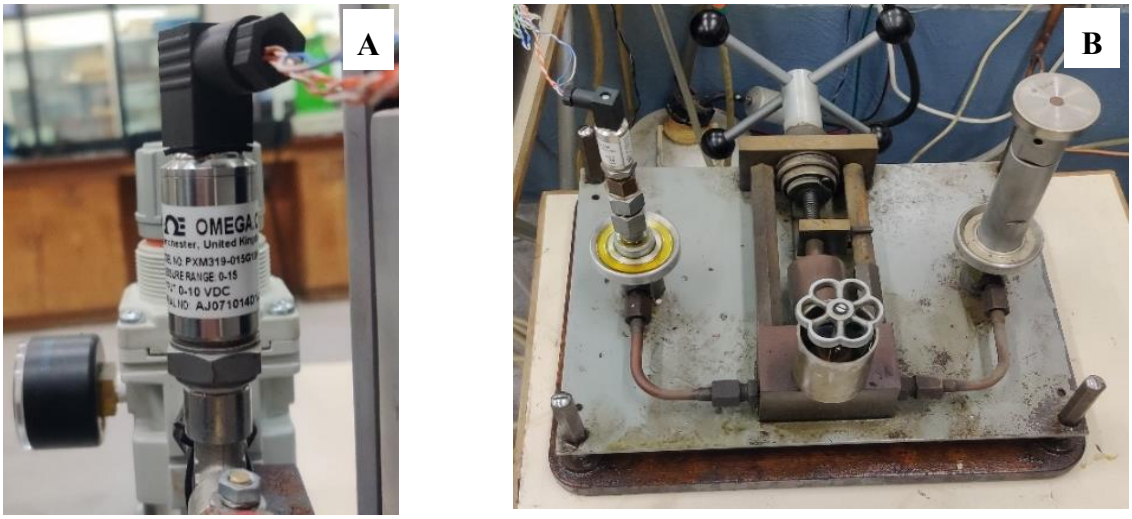

Figure 4-3: A) Omega pressure transducer B) Dead weight tester

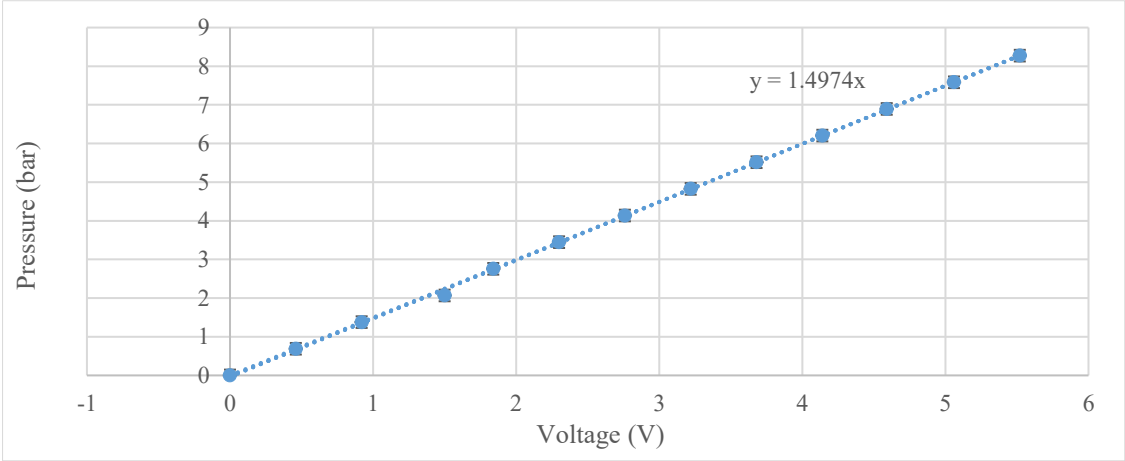

Figure 4-4: The calibration curve for the Omega pressure transducer.

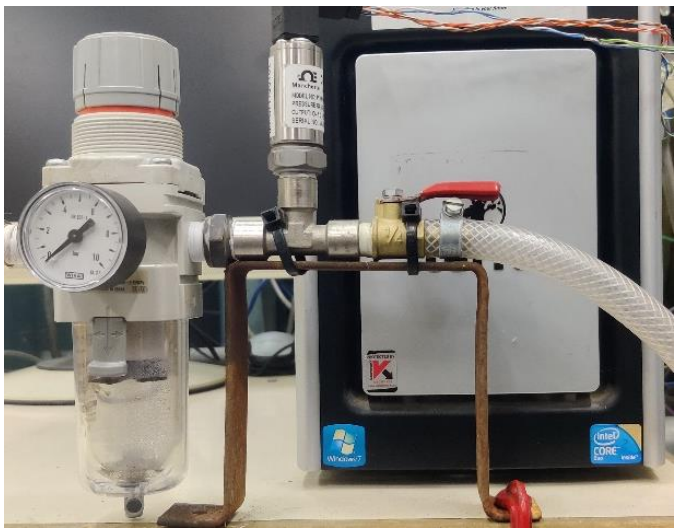

Figure 4-5: The pressure regulator installed upstream of the Omega pressure transducer.

Additionally, the original Bosch 0261230189 MAP sensor installed by Portelli [89] was replaced with a higher range MPX4250AP K0728AF MAP sensor. This modification was implemented to safeguard the sensor from potential damage against any human error in case of a potential pressure increase beyond atmospheric conditions and to enable the possibility to investigate boosted operating conditions. It is noted that the Bosch 0261230189 is rated at 100 kPa, while the MPX4250AP K0728AF is rated at 250kPa Prior to initiating experimentation, the setup underwent a close inspection to ensure that there were no air leaks present. This inspection was crucial to ensure the reliability and precision of the MAF measurement scheme.

After the setup was fully prepared and functioning, a Spartan JRP wideband sensor was installed to facilitate comparative analysis with the computed critical orifice-based lambda. Figure 4-6, illustrates two distinct wideband sensors; on the left is an Air-Fuel Ratio Monitoring System (NGK #91101) previously utilised by Fenech [90] during gasoline engine testing and the other is the aforementioned Spartan JRP wideband sensor integrated into the setup. However, as determined by Portelli [89], the NGK #91101 sensor exhibited inconsistent results during H_2 engine testing, necessitating reliance on a narrowband sensor instead. The primary distinction between these two wideband sensors lies in their measurable lambda range: the NGK #91101 can read up to a λ value of 1.1, whereas the Spartan JRP sensor is capable of measuring λ values as high as 3.

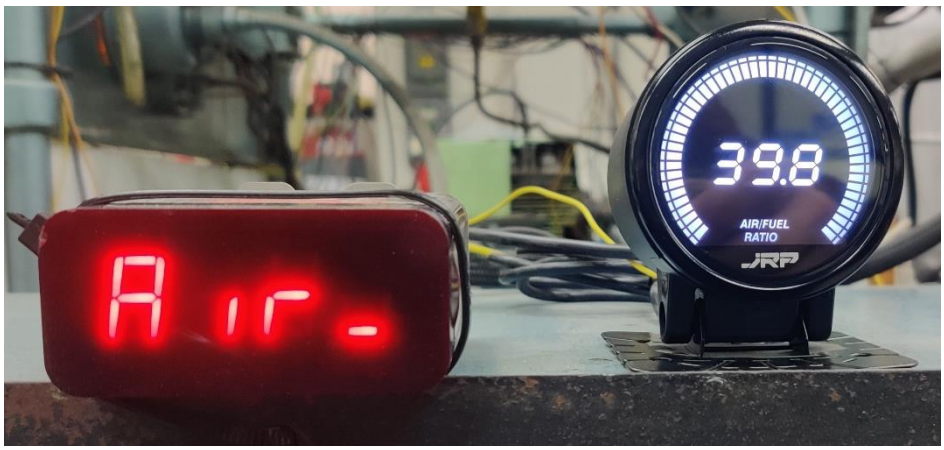

Figure 4-6: the NGK #91101 (on the left) and Spartan JRP (on the right) wideband sensors.

Both narrow band and NOx Exhaust gas oxygen sensors previously used both by Fenech [90] and Portelli [89] during H_2 engine testing were once again used. The NOx sensor has two channels one used to measure the amount of NOx and the other is used to

measure the amount of oxygen content found in the exhaust. The alternative approach utilising a low temperature (AO2) O_2 sensor, detailed by Fenech [90] in Section 4.9, was not implemented due to the considerable response delay observed through the experiments, which were notably greater than that of the other sensors installed on the setup. At a fixed engine speed of 1250 RPM and a MAP of 75 kPa, a H_2 fuel sweep was conducted and the resulting λ measurement from the various techniques were comparatively analysed, as presented graphically in Figure 4-7.

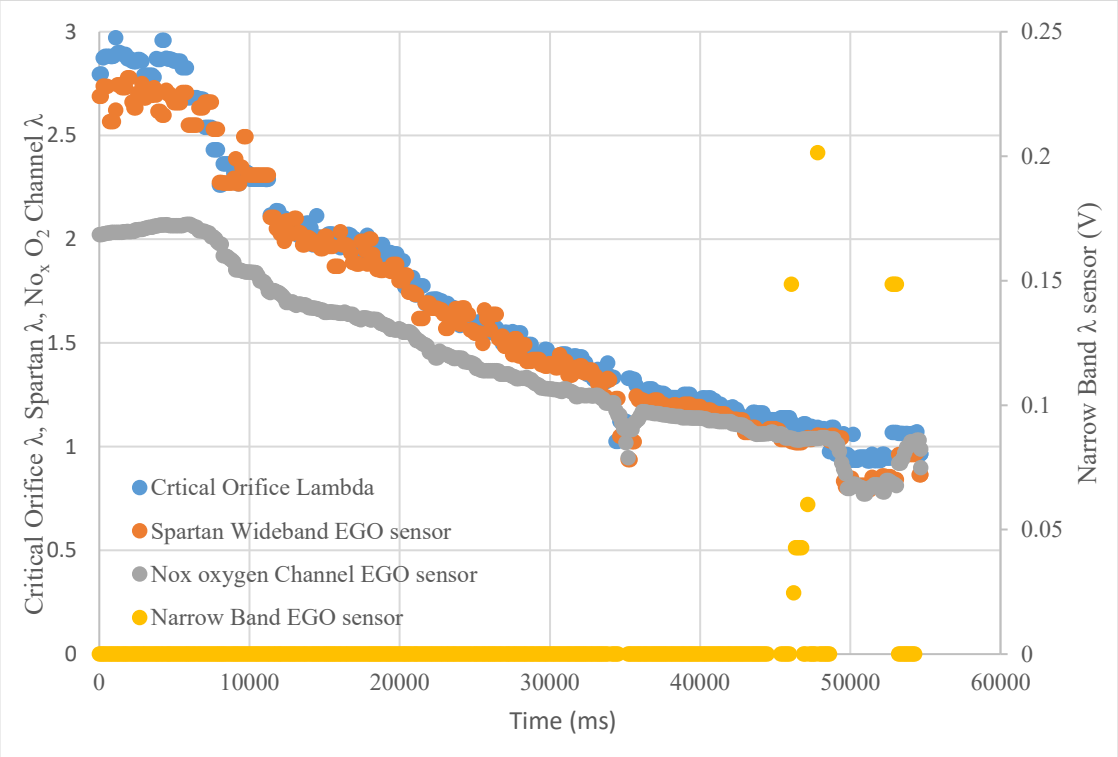

Figure 4-7: Comparison of the various λ measurement techniques.

When comparing the four curves obtained from the different evaluation schemes, the critical orifice λ (blue curve) exhibits characteristics closely aligned with those obtained from the JRP Spartan wideband sensor. However, this alignment is not observed with the curve derived from the NOx oxygen channel (grey), which appears to provide inaccurate measurements during extreme lean conditions and only seems to align with expected characteristics at close to stoichiometric mixtures. In contrast, the narrowband sensor demonstrates proper functionality, as demonstrated by its voltage signal significantly deviating from 0V during transient conditions from lean to rich mixtures.

Consequently, it was concluded that the critical orifice setup performed effectively and can be reliably utilised during H_2 engine testing.

4.3 H_2, Propane and Petrol Test Matrices

The H_2 test matrix detailed in Table 4-2**,** involves all experiments which were conducted at a constant engine speed of 1250 RPM, with varying MAPs of 75, 95, and 120 kPa, across different λ values. For each test condition, optimisation of spark timing, was necessary to achieve minimum spark timing for MBT conditions as suggested by Zareei and Kakaee [55]. To achieve the optimised spark timing, for each fuel, variation of spark timing would be performed at different MAP and the spark value for MBT would be noted. This experimental procedure is often referred to as a "spark sweep". At a MAP of 95 kPa for the three different fuels are illustrated in Figure 4-8.

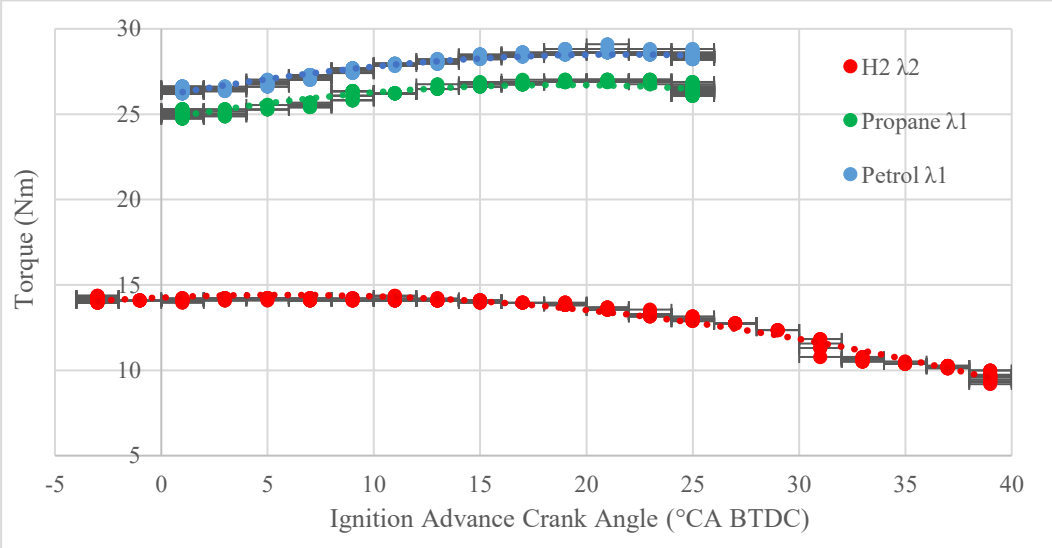

Figure 4-8: The spark sweeps performed for the three fuels at a MAP of 95kPa.

As shown in Figure 4-8, H_2 exhibits a notably wider spark advance curve compared to petrol and propane. For the traditional fuels, petrol and propane, the MBT timing appears more pronounced due to the characteristic shape of the curve, whereas for H_2, this distinction is less clear. Results show that the crank angle range between 10 and 0° CA BTDC tends to produce the maximum torque output for H_2. Literature reports from multiple sources [60] [61] [59] indicate that under similar operating conditions, SI was typically set between 10 and 15° CA BTDC. According to the H_2 spark sweep in Figure 4-8, an ignition advance of 15° CA BTDC was not optimal. However, an ignition advance of 10° CA BTDC falls within the range of crank angles producing maximum

torque. Consequently, the MBT timing for H_2 at λ2 was set to 10° CA BTDC. This optimal ignition advance is further examined and validated in the following Section 4.5.

Table 4-2: H_2 optimal spark timing for MBT at 1250RPM, varying MAP and λ.

MAP (kPa)	λ	Ignition Advance (°CA BTDC)
75	2	10
75	3	20
95	2	10
95	3	10
120	2	10
120	3	10

For comparison reasons, tests with propane and petrol fuels were performed at stoichiometric conditions. For both fuels, MAPs of 50 kPa were also possible but such fuels cannot operate at high lean mixtures as opposed to H_2 which supports operation at high lean conditions of lambda 2 and 3. The propane and petrol test matrices are listed in Table 4-3 and Table 4-4 respectively.

Table 4-3: Propane optimal spark timing for MBT at 1250RPM, λ1 with varying MAP.

MAP (kPa)	λ	Ignition Advance (°CA BTDC)
50	1	25
75	1	20
95	1	20

Table 4-4: Petrol optimal spark timing for MBT at 1250RPM, λ1 with varying MAP.

MAP (kPa)	λ	Ignition Advance (°CA BTDC)
50	1	25
75	1	20
95	1	20

The experimental test matrix is the combination of table 4, 5 and 6 comprising a total of 12 test points.

4.4 Data Acquisition Systems

Data acquisition was done using LabVIEW software in two separate systems referred to as the fast system acquired at 40 kHz and the slow speed system acquired at10 Hz.

4.4.1 Fast data acquisition and post processing

For the fast data processing (40 kHz), the LabVIEW software was utilised, with implementation of the post processing Virtual Instruments (VIs) prepared by Portelli [89]. In-cylinder, crank angle resolved, pressure data was acquired along with other channels namely: crank teeth, cam tooth, current through the spark ignition coil and current through the injector coil. The spark ignition coil current trace was used to measure the ignition delay and confirm the spark advance, while the injector current trace was used to confirm the DOI. The crank angle resolved data is referred to here as the fast data to differentiate it from the slow data that was recorded at 10 Hz. The pressure transducer, AVL GH 13Z-24, integrated in the spark plug, was used to obtain the in-cylinder pressure and its output signal was fed to a charge amplifier (AVL Flexifem Piezo Type 2P2G). The in-cylinder pressure obtained from the piezo electric sensor was pegged to the MAP at bottom dead centre (BDC). One hundred and fifty (150) cycles at each test point were used for the analysis. The fast data was acquired using a National Instruments PCI 6221 card and saved using TDMS file format.

Portelli's VIs where further refined with the required improvements such as the implementation of the two approaches to calculate the MFB. Substantial effort was

dedicated to gain a thorough understanding of the structure and function of these VIs, facilitating the expanded utilisation of the acquired data and enabling additional post-processing analyses. As described in Chapter 3, a number of theoretical combustion analyses were compared and implemented into the VIs to ensure consistent and accurate results across all test points in the test matrix.

4.4.2 Slow speed data acquisition

LabVIEW software was also used for acquisition of operational data (slow data) at 10 Hz to log slow speed parameters such as engine torque, mass air flow, exhaust gas temperature (1/16" type K sheathed thermocouple), switching EGO sensor, NOx emissions, etc., which were measured directly by National Instruments DAQ. The VI previously developed by Portelli [89], was already modified by Fenech [90] and continued to be adapted and modified to accommodate the required changes done to the engine set up. Primarily, the H_2 λ based upon the orifice MAF measurement scheme was introduced alongside the λ computed from the Spartan JRP sensor. It is noted that the slow-speed data acquisition obtains data from the Engine Control Unit (ECU) interface (by sniffing the RS232 data, such as engine speed, MAP, DOI and spark timing) which is then integrated with data acquired from the LabVIEW DAQ system. Therefore, when slow-speed data is referenced in this work, it refers to LabVIEW log files that include synchronized (in-time) engine ECU data.

4.5 Zero-Dimensional Model

As observed in Section 4.3, specifically in Figure 4-8, the minimum ignition advance for MBT from the H_2 curve appears less distinct compared to those for propane and petrol fuels. Therefore, an exercise to numerically model the behaviour and dependency of the engine power loop as a function of spark timing was done in the form of what is termed as a 0D model. This 0D model was formulated to identify the optimal position of the centre of combustion (CA50) to produce a maximum net work output, thereby clearly identify the optimum ignition advance. This model would need inputting of MFB profiles for different spark timings which can either be obtained from experiments or simulations. The main scope of development of this model is to identify the optimum position for the CA50 when working with fuel. A flow diagram of the 0D model is presented below.

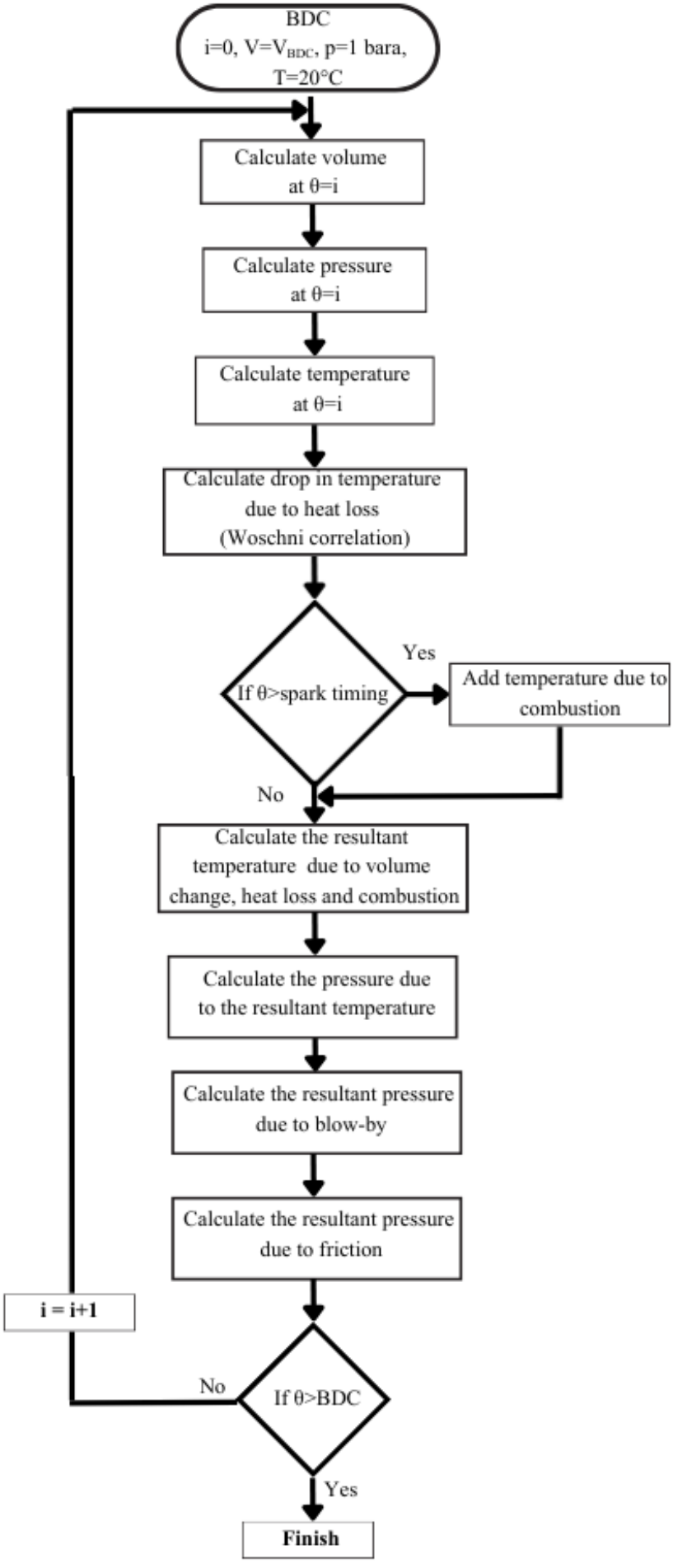
BDC
i=0, V=V_BDC, p=1 bara, T=20°C
Calculate volume at θ=i
Calculate pressure at θ=i
Calculate temperature at θ=i
Calculate drop in temperature due to heat loss (Woschni correlation)
If θ>spark timing
Yes
Add temperature due to combustion
No
Calculate the resultant temperature due to volume change, heat loss and combustion
Calculate the pressure due to the resultant temperature
Calculate the resultant pressure due to blow-by
Calculate the resultant pressure due to friction
i = i+1
No
If θ>BDC
Yes
Finish

Limitations of this 0D model included determining the constants for the Woschni heat transfer correlation and the Chen-Flynn friction correlation, as well as accounting for the variation of properties with temperature and composition during combustion. Key assumptions were that the combustion chamber contained only air and fuel at the start of compression where in reality some exhaust gas recirculation would occur. The temperature and pressure of air at BDC was taken as 20°C and 90 kPa respectively.

From the first law of thermodynamics:

$$Q + W = \Delta U \tag{4.3}$$

The analysis is going to be performed over the entire power loop, i.e. from BDC to TDC and back to BDC. This analysis is conducted in increments of 1 crank angle degree. The work output is calculated based on the volume change occurring between successive crank angle increments. Therefore, at a fixed crank angle, the heat supplied to the engine ΔQ is equal to the energy contained within the fuel which causes the change in internal energy of the air (Energy losses were neglected here but will be incorporated in subsequent analyses).

$$\Delta Q = \Delta MFB \times m_{fuel} \times H = m_{air} \times C_v \times \Delta T_{combustion} \tag{4.4}$$

Where m_{fuel} is the injected fuel, m_{air} is the mass air trapped within the cylinder ($m_{air}$was calculated with η_v=100%)

The burn duration was found from the tests performed and the MFB values (profile/history) obtained from the Rassweiler and Withrow method were evenly distributed by dividing the profile values with the respective burn duration of each experiment. This procedure was only performed for the 95kPa experiments for all the three fuels. Moreover, as done by Beccari et al. [107], a linear relationship was employed to model combustion progress of the cumulative burned mass from ignition start to completion. The temperature due to combustion was found from:

$$\Delta T_{combustion} = \frac{\Delta Q}{m_{air} \times C_v} \tag{4.5}$$

The temperature due to compression ($T_c = T_{i+1}$) was found from:

$$T_{i+1} = T_i \left(\frac{V_i}{V_{i+1}}\right)^{n-1} \tag{4.6}$$

Where the final temperature T'_{i+1} due to the combined effect of compression and combustion was approximated through:

$$T_{i+1}{}' = T_{i+1} + \Delta T_{combustion} \tag{4.7}$$

The resulting pressure due to compression ($p_c = p_{i+1}$) was calculated from:

$$p_{i+1} = p_i \left(\frac{V_i}{V_{i+1}}\right)^{n} \tag{4.8}$$

Where $n = 1.3$ was assumed for both compression and expansion

Since, the volume at each crank angle and amount of gas are kept constant the pressure due to compression and combustion was estimated from:

$$p'_{i+1} = p_{i+1} \left(\frac{T'_{i+1}}{T_{i+1}}\right) \tag{4.9}$$

The incremental work (ΔW) was calculated from (4.8) where the $\Delta V = \frac{V_{i+1} - V_{i-1}}{2}$

$$\Delta W = p'_{i+1} \Delta V \tag{4.10}$$

And the cumulative work can be found by summing the incremental works from Bottom Dead Centre (BDC) to TDC back to BDC.

The analysis was conducted at a MAP of 95 kPa for all three fuels, petrol, propane and H_2. The different fuels have varying burn characteristics, the linear MFB profile imposed was varied for all the three different fuels and according to its respective burn duration. Then the MFB profile was shifted accordingly into different crank angle locations. Shifting the location of the inputted MFB profile directly alters the position of the CA50 and the corresponding cumulative work. The indicated gross work was calculated for each different CA50 location and presented comparatively, as depicted in Figure 4-9.

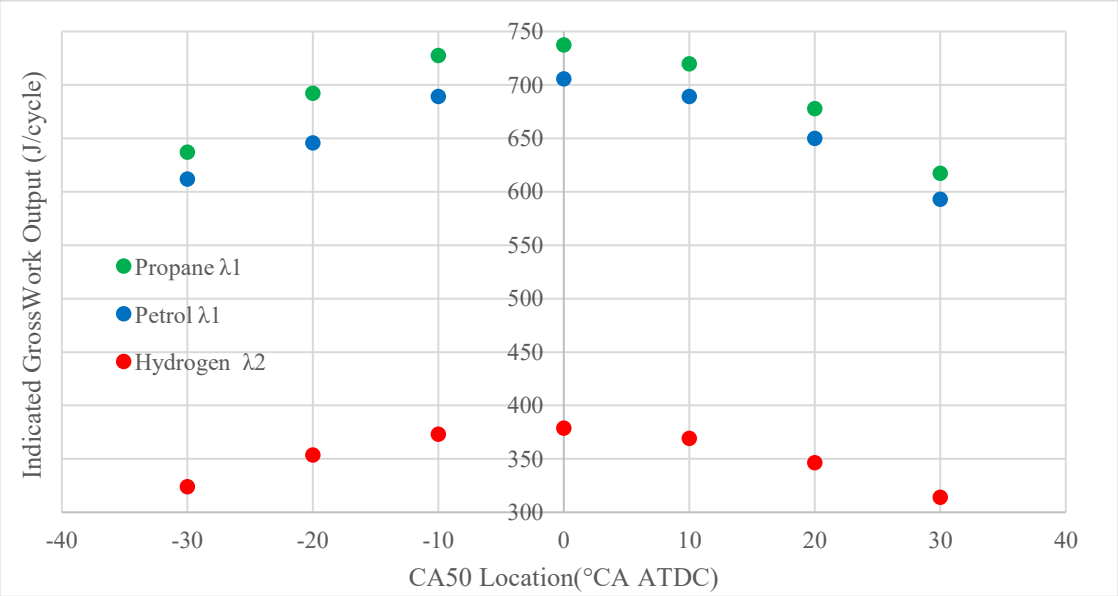

Figure 4-9: Indicated gross work output against different CA50 locations.

It should be recognised that despite H_2 possessing the highest calorific value in this 0D model, it did not produce the highest work output. This outcome is mainly because the H_2 investigation was conducted under non-stoichiometric mixture conditions. Additionally, the low developed torque may also be attributed with the low density of H_2 . The observed variations in the curvature of the plots for the three fuels can be largely attributable to differences in their respective burn durations. From Figure 4-9, the analysis shows that CA50 should always be at TDC to maximise work output. However, the inputted linear MFB profiles in the 0D model for the three different fuels produced higher work compared to that obtained from the experimental investigation. This was attributed to the fact that no friction, auxiliary losses or even pumping loop were taken into consideration.

The “pumping loop” (the work required to move the intake and exhaust gases in and out of the cylinder) is the summation of area B and C identified in Figure 4-10. This was subtracted from the gross indicated work which gives the net indicated work.

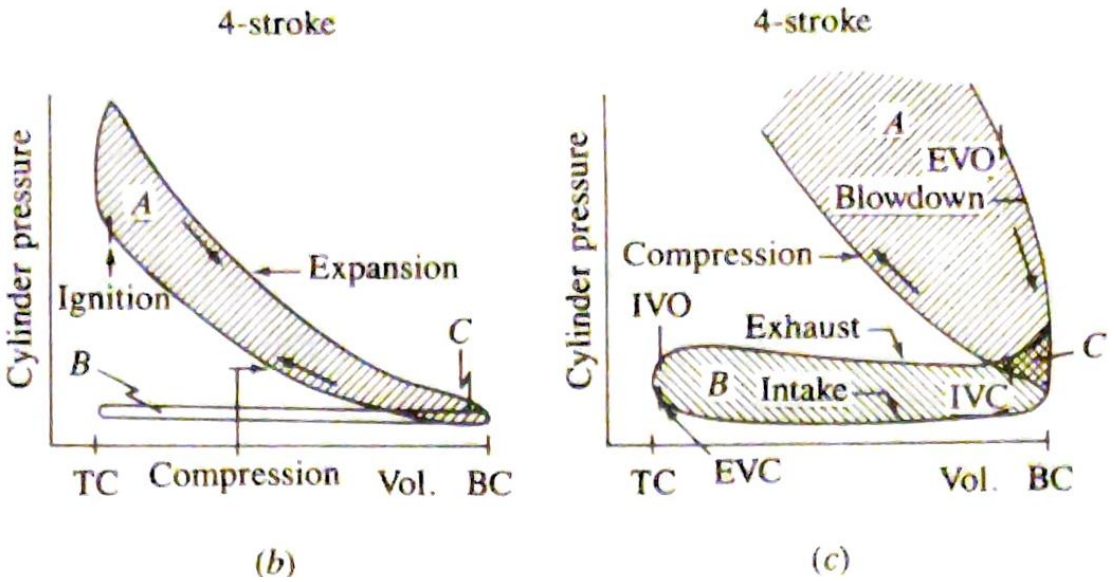

Figure 4-10: P-V diagrams for (b) a four stroke cycle engine and (c) magnification of a four stroke cycle spark-ignition engine exhaust and intake strokes (pumping loop) at part load [60].

Although heat loss was incorporated through n=1.3 the findings presented in Figure 4-9 aligned well with the Otto cycle theory or constant volume cycle where instantaneous heat addition is assumed to take place at constant volume – specifically at TDC – the point at which the piston is momentarily stationary [49].

4.5.1 Alterations to the 0D model

Upon literature findings, a further alteration was done to the 0D model where in order to simulate better the heat loss of the engine, the Woschni correlation was incorporated, rather than simply applying a polytropic index. As stated by Caruana [73], this correlation is used in Ricardo Wave and Gt Power, which are two widely known engine simulation software programs used both for commercial use and also for research purposes. The Woschni correlation is a one-zone model whose limitations are well recognised due to inter-cycle calculations [73], however for the purpose of this 0D model these correlations are adequate and yield acceptable approximations. When describing this Woschni correlation Heywood [49] highlighted the fact that during the development of this correlation only data used from cylinder head thermocouple locations were used. However, it is often used to estimate the “instantaneous spatial average heat fluxes for

the entire combustion chamber". When H_2 MFB profiles were inputted in this OD model as suggested by Krishnanunni et al. [122] the Woschni correlation was multiplied by a factor of 2.2 due to the high burning velocities and low quenching distances of H_2 fuelled internal combustion engines. The Woschni correlation estimates a cylinder heat transfer coefficient (k_c) presented in (4.9).

$$k_c = 3.26B^{-0.2} \times p^{0.8} \times T^{-0.55} \times w^{0.8} \text{ [49]} \quad (4.11)$$

Where the average cylinder gas velocity ($\overline{w}$)

$$\overline{w} = C_1 \bar{S}_p = C_2 \frac{V_s T_r}{p_r V_r} \left(p'_{i+1} - p_{i+1}\right) \text{ [49]} \quad (4.12)$$

Where $\bar{S}_p$ is the mean piston speed; $\bar{S}_p = 2 * Stroke * Engine\ Speed.$ V_s is the displaced volume, p_r, V_r, T_r are the working-fluid pressure, volume and temperature at some reference state (such as at inlet valve closing). p_2 is the pressure due to compression found from (4.8) and $p'_{i+1}$is the final pressure due to compression and combustion found from (4.9). The constants $C_1$and C_2 vary:

For the gas exchange period: $C_1 = 6.18$ $C_2 = 0$

For the compression period: $C_1 = 2.28$ $C_2 = 0$

For the combustion and expansion period: $C_1 = 2.28$ $C_2 = 3.24 \times 10^{-3}$

Then the instantaneous heat flux (q'') per crank angle was found from:

$$q'' = k_c(T_{i+1}{}' - \mathrm{T}_{wall}) \quad (4.13)$$

Where T_{wall} is the cylinder liner wall temperature which was assumed to be 373K

Which then resulted in the instantaneous temperature drop (T_{h_c}) calculated from:

$$T_{h_c} = \frac{q''}{(C_v \times m_{air})} \quad (4.14)$$

Therefore from (4.9) the final pressure due to compression, combustion and heat loss (p''_{i+1}) was found from:

$$p''_{i+1} = p_{i+1}\left(\frac{T'_{i+1} - T_{h_c}}{T_{i+1}}\right) \tag{4.15}$$

The calculation of blow-by gases was incorporated in the 0D model by using (3.6) explained in Section 3.1 at each crank angle which was subtracted from the mass of air and fuel (since the engine is port fuelled) initially occupied within the cylinder.

Although as outlined by Beccari et al. [107] friction has a lower impact when compared to thermal losses it was still added in the in the 0D model. Ricardo WAVE makes use of the Chen and Flynn correlation to estimate the Friction Mean Effective Pressure (FMEP) [123] where Caruana et al. [124] compared this correlation with experimental data and successfully deduced an acceptable match. Hence the correlation presented in (4.16) was used as a guideline to identify the most important terms to incorporate in the 0D model. It is important to appreciate that (4.16) cannot be directly implemented in this model since it is not crank angle based.

$$FMEP = A_{CF} + \frac{1}{n_{cyl}}\left[B_{CF}P_{max_i} + C_{CF}\left(\frac{RPM \times stroke}{2}\right) + Q_{CF}\left(\frac{RPM \times stroke}{2}\right)^2\right] \tag{4.16}$$

Where A_{CF} represents the constant accessory friction, B_{CF} is the coefficient multiplied to the linear pressure load term, C_{CF} is the coefficient to the engine speed contribution and Q_{CF} is the coefficient to term representing the windage losses [125]. For the purpose of the 0D model, windage losses were incorporated into the constant accessory friction term since the experimental tests were conducted at a constant speed. The value of the constant accessory friction was found in terms of energy and was subtracted from the gross work. Consequently, the only two remaining terms that would be a function of crank angle would be those resulting from piston ring friction ($F_{piston\ velocity}$) caused by the fluctuating piston velocity (4.12) and in-cylinder pressure acting on the rings ($F_{pressure}$) (4.14).

$$F_{piston\ velocity} = C_{CF} \times S_p(\theta) \tag{4.17}$$

The instantaneous piston
speed

$$S_p(\theta) = a\cos\theta + \sqrt{L^2 - a^2\sin^2\theta} \tag{4.18}$$

where a is the crank radius, L is the connecting rod

$$F_{pressure} = B_{CF} \times p'_{i+1} \tag{4.19}$$

Therefore, the absolute total friction (F_{total}) was found by summation of the pressure, velocity and auxiliary terms as in found from (4.17).

$$F_{total} = F_{pressure} + F_{piston\ velocity} \tag{4.20}$$

The summation of the total friction is depicted in Figure 4-11 and to validate the values of B_{CF}, C_{CF} and the combined term of A_{CF} & Q_{CF} of the total friction, a comparison was made with Figure 4-12 [49]. The similarity in magnitude observed between the two graphs supports the validity of the applied friction modelling in the 0D model. Although friction was plotted with a consistent positive sign, the model ensured that these effects were subtracted from gross indicated work rather than added. For record $B_{CF} = 0.00009$, $C_{CF} = 12$ and the combined term A_{CF} & $Q_{CF} = 38.4\ J/cycle$

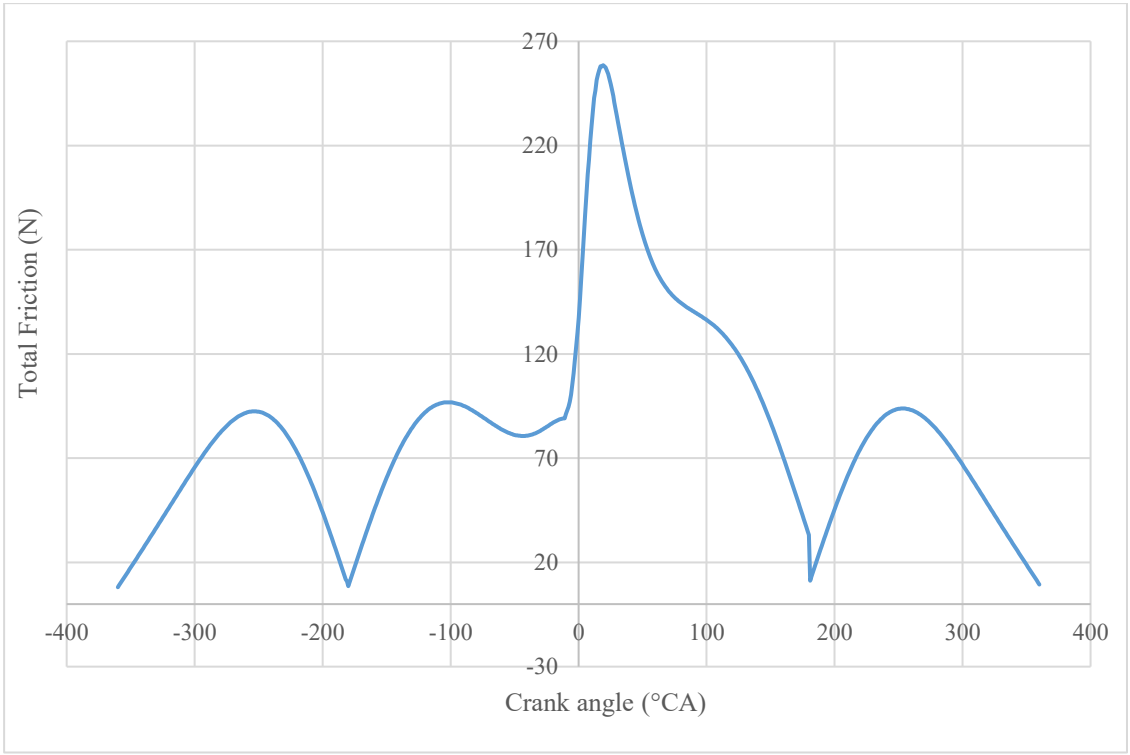

Figure 4-11: The variation of the total friction with crank angle.

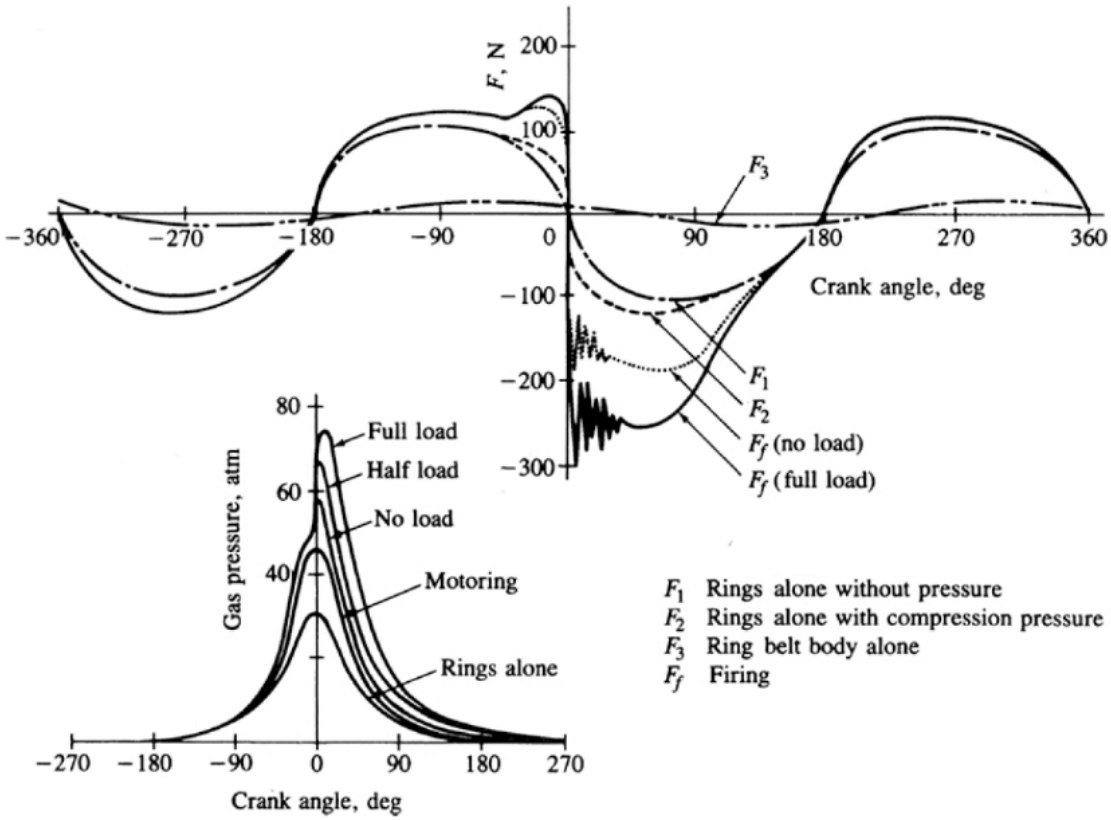

*Figure 4-12: Measured frictional force on cylinder liner **[49]**.*

Additionally, the γ for the intake air was varied accordingly with the in-cylinder temperature by using C_p relations for nitrogen and oxygen where the corresponding coefficients were quoted by Heywood in Table 4.10 [49]. After combustion ended; when MFB reached unity, a different γ derived from values of the combustion products [126] were implemented for the rest of the cycle.

4.5.2 Implementation of MFB Profiles with a Varying Heat Release

In an effort to adhere more closely to the heat release characteristics and as Beccari et al. [107] clearly stated to as the "heat release rate law", implementation of MFB profiles with a non-constant heat release was essential. Rather than making use of the traditional Wiebe function, the correlation proposed by Bayraktar and Durgun [109] in (3.17) was utilised to estimate burn durations corresponding to various CA50 positions. However, upon implementation, the resulting burn duration values deviated from those reported by the authors [109], suggesting possible limitations in directly applying the published

correlation. As an alternative, additional tests were performed using H_2 and petrol fuels at various spark timings. Post-processing of these tests enabled the implementation of

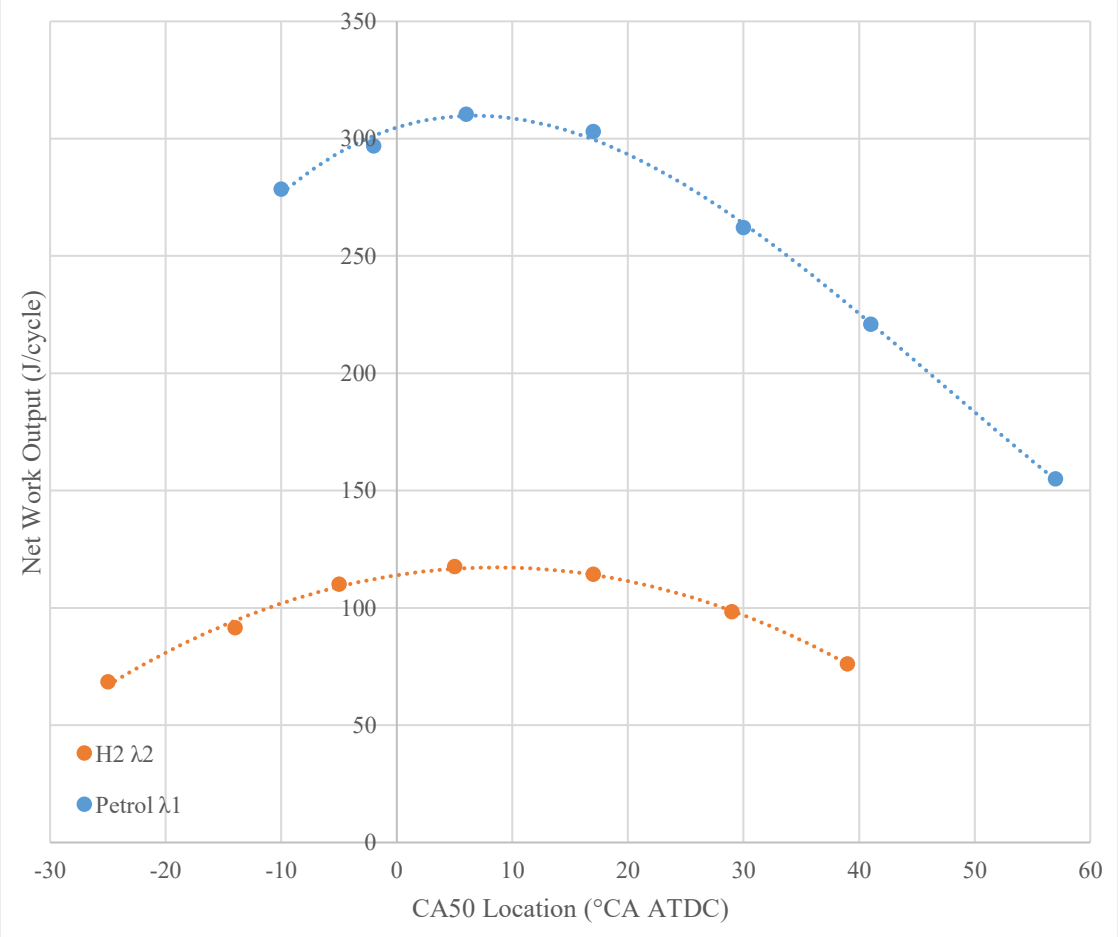

the various obtained MFB profiles (presented later in Chapter 6) to be inserted into the 0D model according to the corresponding CA50 locations. The net work output at the different CA50 locations was plotted as observed in Figure 4-13.

To ascertain the accuracy of this 0D model, the corresponding pressure values obtained from the model (Analytical), after inputting the experimental MFB profiles, were compared to the experimental measured in-cylinder pressure by using the p-v diagram shown in Figure 4-14. It is noted that the exhaust portion, known as the "blow down phase" that is the expulsion of gases due to their own high pressure, is not shown in Figure 4-14. This is because it involves modelling critical flow through complex and varying valve geometry. Subsequently the remaining exhaust gases are pushed out of the cylinder by the so called "exhaust displacement phase". The blow down occurs practically at constant volume and hence no work involved while the displacement phase

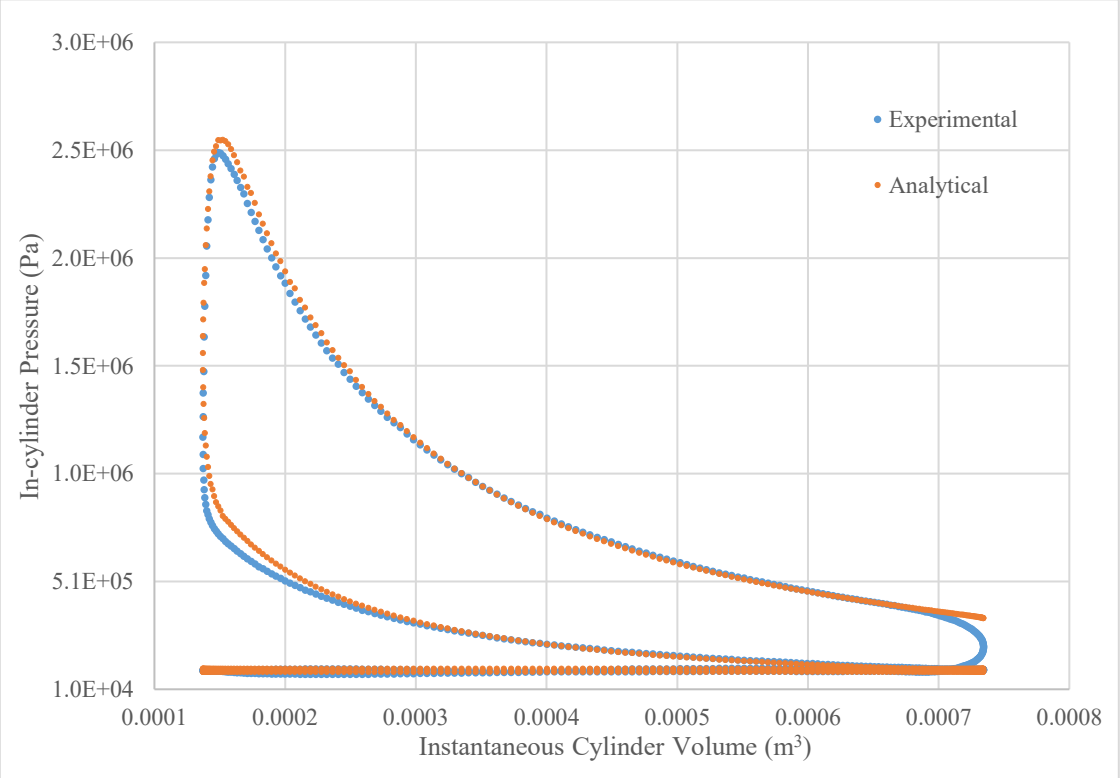

Figure 4-14: In-cylinder pressure against instantaneous cylinder volume for petrol fuel at 95 kPa MAP

occurs cover a whole stroke thus, there is associated work. Therefore, there was no need to model the blow phase. To achieve agreement between the analytical and experimental in-cylinder pressure readings, it was necessary to apply a reduction factor to the gross

work output. This reduction was applied to the inputted Rassweiler and Withrow MFB profiles that in fact also complied with the MFB profile as obtained from Pipitone's approach in Section 3.4. On average, across all experiments conducted, a 20% reduction in the gross work output was required. This reduction in work align closely with the loss previously highlighted by Rogers [97] and Heywood [49].

As seen in Figure 4-13, the peak net work output for petrol fuel deviated by approximately 7° CA with respect to TDC which aligns well with the values suggested by Heywood [49] and Beccari [107]. For the H_2 fuel, the peak net work output was obtained at a CA50 location of approximately 10°CA. This conclusion perfectly matches that obtained by Rrustemi et al. [60], Sementa et al. [61] and Molina et al. [59] who all obtained similar CA50 locations. Moreover, although H_2 has a higher burn rate compared to petrol, the CA50 position deviated further from TDC than the CA50 obtained during petrol experiments. This was unexpected, as Beccari et al. previously indicated that a faster burning charge typically reaches 50% MFB closer to TDC than a slower burning mixture. However, it is important to note that the ignition advance was set to 20° CA BTDC for petrol, whereas it was set to 10° CA BTDC for H_2. Despite this, the CA50 location did not differ significantly, further demonstrating H_2's faster burn duration.

4.6 Closing Remarks

Initially, a critical orifice was integrated into the experimental setup to improve the accuracy of airflow measurement, thereby enabling accurate AFR calculations during H_2 testing. This method was compared to an off-the-shelf Spartan wideband EGO sensor, which exhibited similar behaviour to the calculated AFR values. Subsequently, comprehensive tests were conducted using H_2, propane and petrol for comparison purposes, with a test matrix comprising of 12 operational points. Furthermore, a 0D model was developed to evaluate the maximum net cycle work output as a function of CA50 variation for H_2 at $\lambda 2$ mixtures and petrol under stoichiometric conditions.

Chapter 5. Dual-Fuel Experimental Investigation

During varying loads, DFEs tend to experience combustion instability, mainly caused by engine knock thus an operating window is identified [18]. During this transient operation a decrease in the intake temperature can reduce this instability and provide some leeway within the operating window. The main scope of this experimental investigation, referred to as Liquid State Dual injection (LSDi) is to make use of the latent heat of cryogenic liquids such as LNG which would be abundantly available on LNG cargo ships to reduce such phenomena. A cryogenic setup, designed for potential use with LNG, was constructed and initially tested with liquid nitrogen (LN_2), followed by testing with liquid propane. Unfortunately, the acquisition of LNG in Malta was not possible due to transportation complications and storage requirements, which could have compromised safety. This cryogenic set up was directly installed onto the existing dual-fuel engine setup which runs on diesel and propane at vapour state. Several tests were carried at steady state conditions at boosted conditions of 150 kPa absolute and varying intake air temperatures where knock intensity was monitored.

5.1 Previous Engine Modifications and its Specifications

The dual-fuel setup is composed of a 2.0 litre common-rail diesel engine depicted in Figure 5-1 and its specifications are listed in Table 5-1.

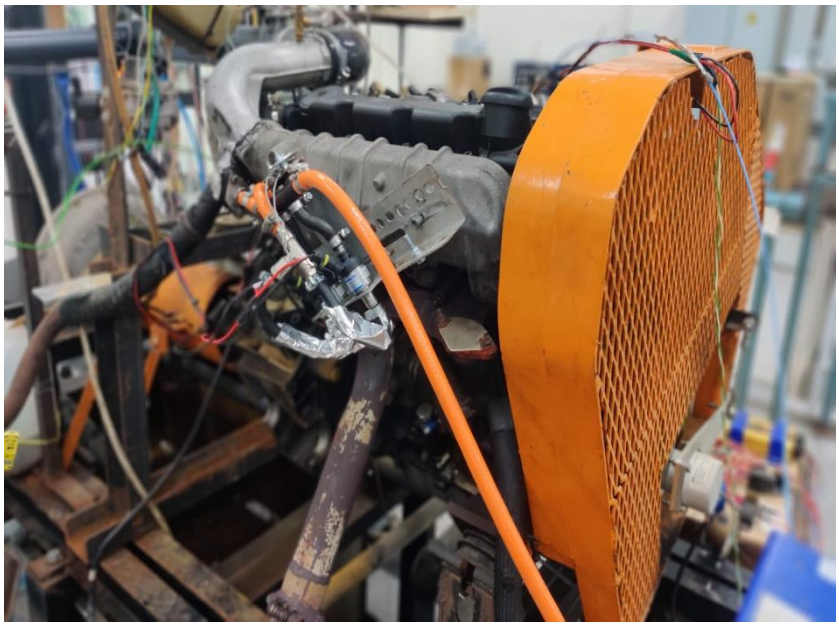

Figure 5-1: The dual-fuel engine setup.

The engine was retrieved from a Peugeot 306 in which its conversion to dual-fuel was first implemented by Mifsud [127] and afterwards by Schembri [128]. Subsequently, Schembri [129] optimised its performance and carried out an experimental investigation on the combustion behaviour through in-cylinder pressure investigation and also measured its NOx emissions. Schembri [129] removed the engine's original factory turbo charger to facilitate testing. Following this, Azzopardi [91] built a modular air intake system which supported both boosted (using an electrical driven roots blower) and natural aspirated conditions. In addition, Azzopardi [91] installed an off-the-shelf MoTec M600 ECU and a knock detection system onto the dual-fuel setup after it was verified on a SI engine. This detection system consists of a MoTec 53116 SKM knock signal DAQ system which provided a real-time knock indicator.

Table 5-1: Peugeot 306 engine specifications.

Manufacturer	Peugeot Société Anonyme (PSA)
Model	DW10 TD/RHY
Number of cylinders	4
Capacity (c.c.)	1997
Stroke (mm)	88
Bore (mm)	85
Compression Ratio	18:1
Valve train	8 Valve, Overhead Camshaft

5.1 Dual-Fuel Testing with LN_2

5.1.2 Acquisition of appropriate apparatus

During the equipment selection process for the cryogenic injection system, foundational

cryogenic specifications were prioritised to guide equipment selection. To narrow down component selection from commercially available options, simple calculations and assumptions were conducted. Primarily the required cryogenic liquid mass flow rate was determined to achieve a measurable reduction in intake air temperature, which subsequently guided the sizing of the cryogenic storage tank and solenoid valve. Initial calculations focused on estimating the engine's air mass flow rate under a boosted intake pressure of 150 kPa using (5.2) and the engine speed was assumed to be set to 3000RPM, however the actual tests were performed at 2000RPM due to apparatus limitations.

Assuming adiabatic compression of an ideal gas its temperature would rise to:

$$T_{i+1} = T_i \left(\frac{p_{i+1}}{p_i}\right)^{\frac{\gamma-1}{\gamma}} = 298 \times \left(\frac{100 \times 10^3}{150 \times 10^3}\right)^{\frac{0.4}{1.4}} = \mathbf{334.6\ K \approx 62\ ℃} \quad (5.1)$$

The η_v was once again assumed to be 100% and the ρ for air was taken to be 1.75 kg/m^3 at an air pressure and temperature of 150 kPa and 25°C despite the compression temperature rise to 62°C - since an intercooler is installed on the setup.

$$\dot{m}_{air} = \rho \eta_v V_s \frac{N}{2} n_{cyl} = 1.75 \times 1 \times \frac{\pi(0.085)^2}{4} \times 0.088 \times \frac{3000}{60 \times 2} \times 4 \quad (5.2)$$

$$= \mathbf{0.0875\ kg/s}$$

It was decided that the first preliminary tests would be performed with Liquid Nitrogen (LN_2) to test the credibility of the apparatus. A schematic diagram of the proposed cryogenic setup onto the engine setup is illustrated in Figure 5-2.

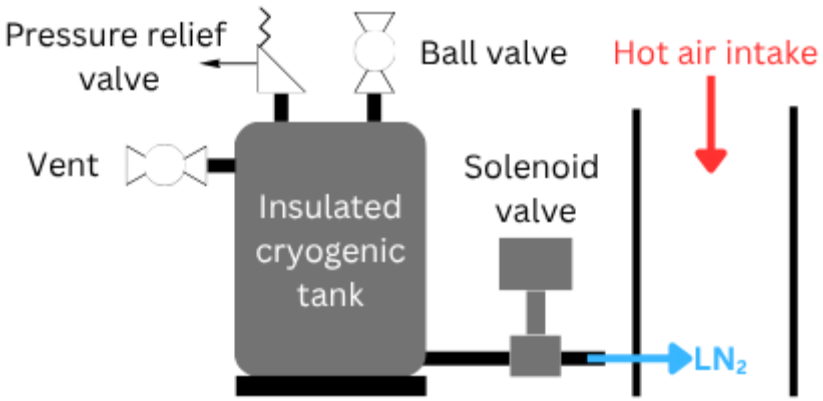

Figure 5-2: Schematic diagram of the proposed cryogenic setup.

If losses are neglected the latent heat of the injected LN_2 would be equal to the energy decreased from the intake air and assuming that a drop in temperature of 20 °C would be sufficient to mitigate the chance of knock to take place [130], the mass flow rate of LN_2 needed was found from (5.3). The latent heat (h_{fg}) of LN_2 was taken to be 190 kJ/kg at a pressure of 150 kPa (due to boosted conditions of 0.5 barg) [126].

$$\dot{m}_{N_2} h_{fg} = \dot{m}_{air} C_p \left(T_f - T_i\right) \tag{5.3}$$

$$\dot{m}_{N_2} = \frac{0.0875 \times 1005 \times 20}{190 \times 10^3} = \mathbf{0.0093\ kg/s}$$

If each test would last approximately 1 minute which is sufficiently long enough to gather the relevant data needed for investigation, the total LN_2 (m_{LN_2}) consumed would amount to:

$$Total\ m_{LN_2} = 0.0093 \times 60 = \mathbf{0.56\ kg}$$

The reservoir would be pressurised to 3.5 barg, the corresponding volume occupied by the LN_2 (V_{LN_2}) would result to: where ρ = 755 kg/m^3 [126]

$$V_{LN_2} = \frac{0.56}{755} = \mathbf{0.74\ litres}$$

Hence, a 2-litre reservoir would be sufficient to conduct two experiments without refilling. The reservoir displayed in Figure 5-3A was purchased, which is made out of stainless steel 304 as recommended by multiple sources [131] [132] and withstands a pressure of 12.5 bar.

The cryogenic solenoid valve (HSB-3 90767) purchased is rated to work between temperatures of -200 °C and -40 °C and is mainly designed to work with LN_2. However, since the boiling temperature of LN_2 is less than that of LNG, it would be suitable as well for the cryogenic fuel. From Figure 5-3A it is important to appreciate that the valve stem of the nozzle is long to mitigate heat transfer from the coil to the cryogenic fluid and avoid it boiling off before being injected into the manifold. This design reassures the injection of LN_2 rather than gaseous N_2.

5.1.3 Orifice diameter determination

An orifice is required downstream of the cryogenic solenoid valve to effectively control (meter) the flow of the cryogenic fluid as it exits the valve. This component is essential to ensure precise delivery of the medium. Maintaining consistent flow characteristics is crucial for the reliable cooling of the intake air during testing. In the absence of a nozzle, the fluid discharged from the solenoid valve may become uncontrolled, thereby reducing the efficiency and accuracy of the cooling process, which demands precise fluid dispersion control. As outlined by White [133], an orifice can operate in different modes depending on the ratio of discharge to supply pressure. For the LN_2 injection system, a 3 bar pressure difference was established between the intake manifold and reservoir, to be consistent with the supply pressure used in prior propane tests [91] [92]. The nozzle throat diameter (d_t) was subsequently determined based on this pressure difference.

$$A_t = \frac{\dot{m}_{LN_2}}{C_d\sqrt{2\rho\Delta p}} = \frac{0.0093}{0.65\sqrt{2 \times 750 \times 3 \times 10^5}} = 5.60 \times 10^{-7}\ m^2\ [133] \qquad (5.4)$$

$$d_t = \sqrt{\frac{4 \times 5.60 \times 10^{-7}}{\pi}} = 0.844mm \approx \mathbf{0.85\ mm}$$

The value of 0.65 for the C_d were based upon recommendations done by Ower [116] and values from the ISO 5167-2 [121].

5.1.4 Prototype setup

After all necessary equipment was procured a prototype set up was built to perform some initial testing with LN_2 to verify the integrity of all the equipment as an integrated whole system as depicted in Figure 5-3A. A fine filter, as shown in the Figure 5-3B, was positioned at the bottom of the reservoir to prevent debris from entering the solenoid valve thereby avoiding potential blockages or damages to the solenoid valve. The vent valve depicted clearly in the illustration in Figure 5-2 evacuates N_2 gas during apparatus cooling. Initially, large amounts of LN_2 evaporate instantly upon pouring therefore this valve enables continuous filling by removing this N_2 gas from the reservoir. As depicted in Figure 5-4A a container was also placed beneath the solenoid valve so that LN_2 can be poured into it to increase the cooling process of the solenoid valve and LN_2 can be delivered accordingly. This cooling is necessary because temperatures above the boiling

point of LN_2 can cause it to change to the gaseous state. Additionally, insulation was applied to the reservoir and to all necessary piping to reduce heat transfer from the surroundings.

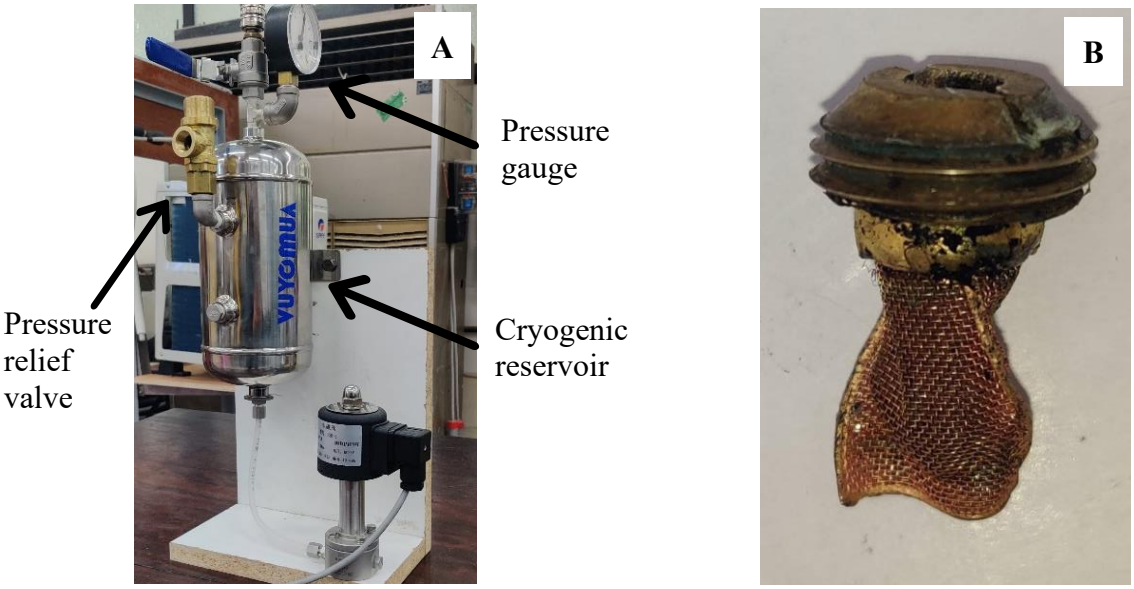

Figure 5-3: A) The cryogenic setup before installed onto the engine.

B) The fine filter installed at the bottom of the cryogenic tank.

Due to the large temperature difference between the apparatus of the setup at ambient conditions and LN_2, the amount of LN_2 (m_{LN_2}) needed for the cooling process was estimated by weighing of the whole setup and assuming the same type of material throughout being stainless steel. The heat energy needed for the latent heat of LN_2 would be equal to the change in temperature of the relevant components from ambient temperature of 25 °C to the boiling temperature of around -200 °C. The whole setup weighed approximately 4 kg (m_{setup}).

$$m_{LN_2} h_{fg} = m_{setup} C_p \Delta T \tag{5.5}$$

$$m_{LN_2} = \frac{4 \times 480 \times (25 - -200)}{199 \times 10^3} \approx \mathbf{2\ kg}$$

Approximately 2 kg of LN_2 was required to cool the apparatus to the corresponding boiling temperature. This cooling process was essential to ensure that the solenoid valve delivers LN_2 rather than gaseous nitrogen (N_2). Injecting N_2 into the intake manifold would mean that the latent heat of vaporisation would already have been transferred to the medium, thereby significantly diminishing the effectiveness of the cooling effect.

Therefore, maintaining the apparatus of the injection system at the boiling temperature of LN_2 was crucial for optimal cooling performance. Frost immediately formed onto surfaces with no insulation applied as seen in Figure 5-4A. Leaks were checked with compressed air before filling up with LN_2 and insulation was installed onto the prototype to decrease the heat transfer to the surrounding ambient and minimise vaporisation of the LN_2 as seen in Figure 5-4B.

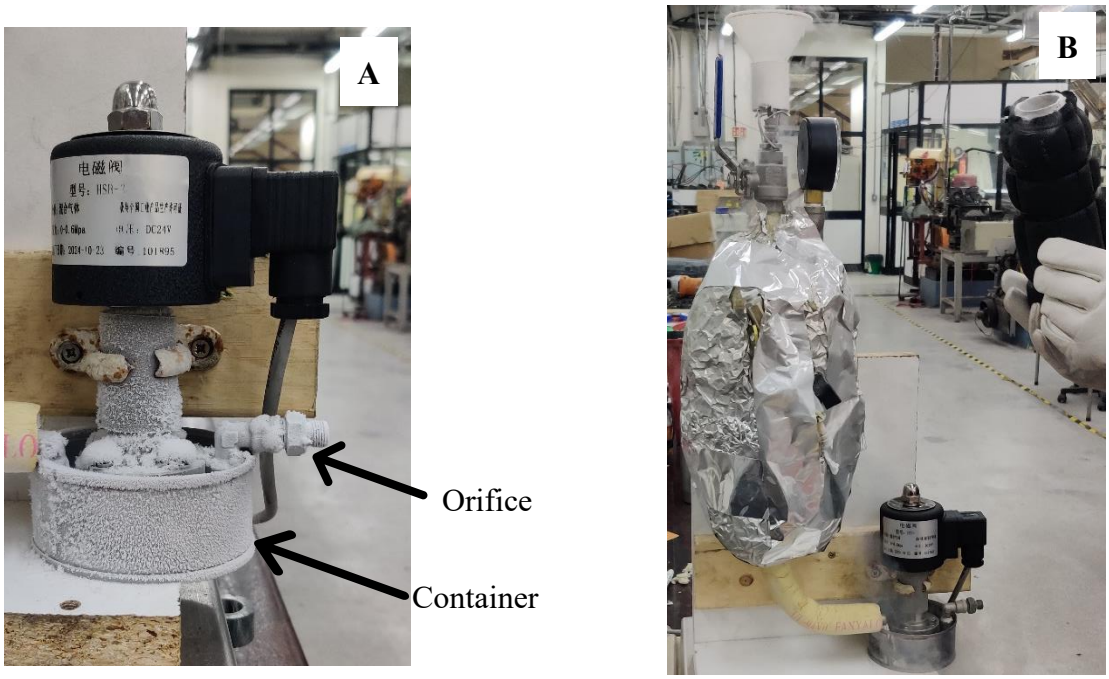

Figure 5-4: A) The container placed beneath the solenoid valve.

B) The insulated cryogenic setup during LN_2 preliminary testing.

5.1.5 Solenoid valve calibration

The flow rate of the solenoid valve is determined by the calculated orifice diameter and the associated parameters described in Section 5.1.3. To calibrate and verify the flow rate of the orifice a gravimetric flow test was performed where the entire setup was weighed while the solenoid valve was operated at a 100% duty cycle. The 2-litre tank (cryogenic tank) was supplied with compressed air of 3 barg to be consistent with the calculations performed in Section 5.1.3. To determine the flow rate through the orifice, the total weight of the cryogenic setup was measured before the injection of LN_2 and again after a defined time interval of 36s. A flow of 9.5±0.1 g/s was measured during this test which is fair when compared to that previously calculated of 9 g/s in Section 5.1.3.

5.1.6 Cryogenic setup installation

Due to the vibrations caused by the engine during experimentation, it was decided that the whole cryogenic setup would be installed onto the surrounding structure rather than with the engine itself. Since vibrations still would be present in the fixed structure the cryogenic setup was installed by means of studs as seen in Figure 5-5A to dampen the vibration caused and decrease the sploshing of the cryogenic fluid inside the reservoir. This mounting fixture was chosen for its structural rigidity in the vertical direction and ability to minimize resonant amplification in the horizontal direction. Its position was also determined to optimise accessibility for refilling. An adequate flexible pipe was carefully chosen to allow the transfer of the cryogenic fluid from the static reservoir to the vibrating intake pipe of the engine depicted in Figure 5-5B.

Figure 5-5: A) Installed cryogenic setup on the engine.

B) Flexible pipe fixed to the solenoid valve and intake pipe.

As seen in Figure 5-7 and Figure 5-6, inside the intake pipe, a stainless steel sheet was installed horizontally to increase the contact surface area of the intake air to increase the cooling effect. The sheet was installed to prevent cryogenic fluid from immediately being carried away into the intake manifold by the high velocity intake air. The sheet width matched the pipe diameter, its length was three times the width (engineered

choice), and the 8 mm lip height minimized airflow blockage. This was done by forming a 90° at the far edge facing the intake manifold. Moreover, this avoids inconsistent delivery of intake air temperatures to different combustion chambers and through turbulence within the intake air pipe formation of a more homogeneous intake air temperature is encouraged. Two slots were also done to the intake pipe to allow fixing of the plate to avoid it rotating or worse ending up blocking the intake manifold during experimentation. During the procedure it was made sure that all components installed are clean and free of any debris which might damage the engine. The cryogenic solenoid valve was designed to be controlled from the LabVIEW software program previously utilised to monitor the other equipment found on the engine setup.

Figure 5-7: The fabricated stainless-steel plate.

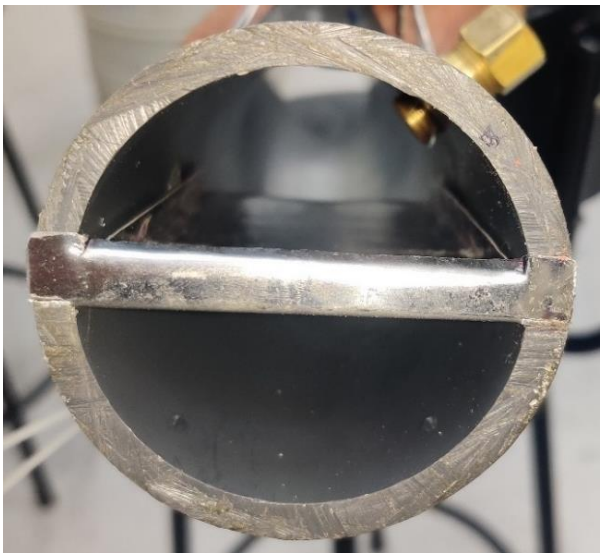

Figure 5-6: Stainless-steel plate inserted inside the intake pipe.

The solenoid valve was actuated using an input signal from a FeelTech DDS signal generator and the associated electrical circuit, as illustrated in Figure 5-8, to produce the required pulse widths required during the calibration process.

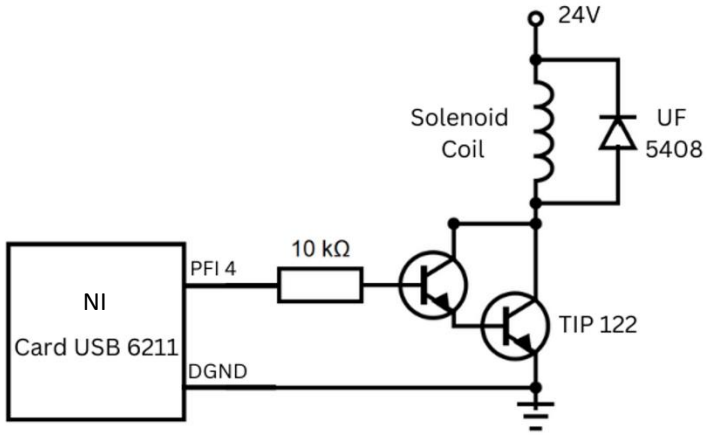

Figure 5-8: Electrical circuit for the cryogenic solenoid valve used during engine testing.

5.1.7 Steady state testing

To test the installed setup and ensure correct functionality, dual-fuel tests with diesel and LPG were first conducted with LN_2 injection. To investigate the effect of this setup with regards to knock, steady state tests were performed where the intake air was heated from the setup prepared by Azzopardi [134] to a temperature of approximately 70 °C and the diesel injection was advanced to 22° CA BTDC. Such conditions increase the likelihood of knock and facilitate a clearer demonstration of the effect of intake temperature reduction through LN_2 injection. Before experimentation took place, it was ensured that the pressure inside the 2-litre tank had increased to 3.5 barg providing a pressure difference of 3 bar between the manifold and the 2-litre tank due to boosted conditions of 0.5 bar. The solenoid valve was set to operate at a 100% duty cycle, which resulted in an initial temperature drop of approximately 13 °C as observed in **Error!**

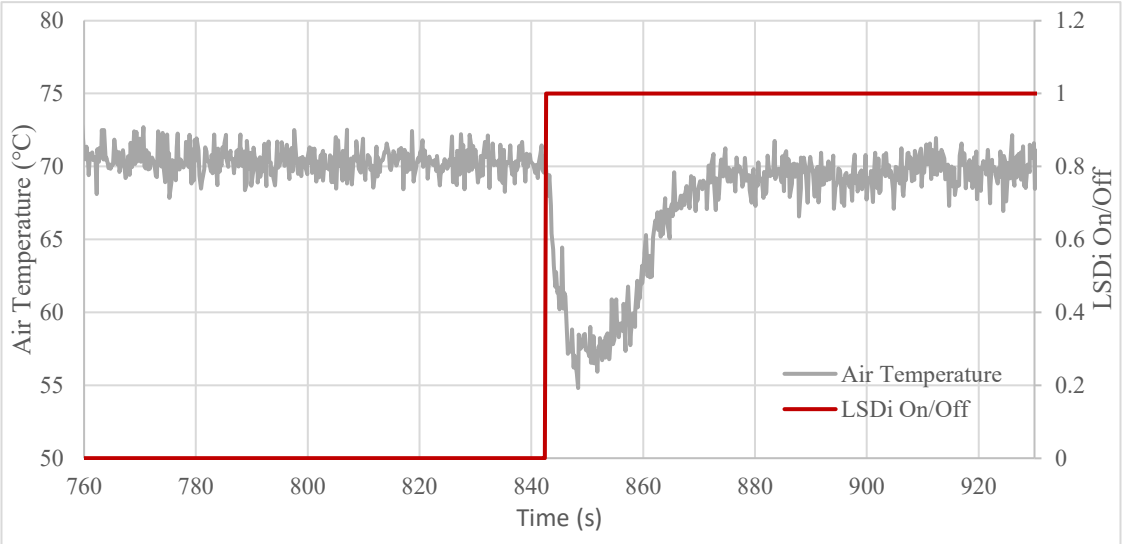

Figure 5-9: Drop in intake temperature during LN2 injection without compressed air

Reference source not found.. This discrepancy between the observed temperature drop and that initially assumed of 20 °C is attributed to the lack of sufficient pressure inside the reservoir which directly affected the flow rate. However, the temperature gradually began to rise afterwards. The air temperature was measured using a K type 1/16″ thermocouple positioned approximately 400 mm downstream of the LN_2 injection. During testing, it was noticed that the pressure within the 2-litre tank changed noticeably in response to LN_2 injection. Due to the reservoir's limited capacity, even minor changes in the amount of LN_2 affected the internal pressure significantly. Additionally, limited time prevented LN_2 from evaporating at a sufficient rate, resulting in unstable pressures. This unstable pressure resulted in inconsistent LN_2 injection quantities which caused a varying intake temperature drop compromising the obtained results. Hence, to stabilise the pressure, compressed air was supplied to the 2-litre tank and regulated to 5.5 barg. A higher air pressure was selected compared to the initially calculated 3.5 barg in the previous section to achieve a greater temperature drop, thereby enhancing the knock reduction effect. It is also important to mention that the initial assumed experimental duration of 1 minute will be greatly affected. As seen in Figure 5-10, with the compressed air supply of 5.5 barg the drop in the intake air temperature of approximately 45°C remained constant until the solenoid valve was closed (red curve changed from 1 V to 0 V).

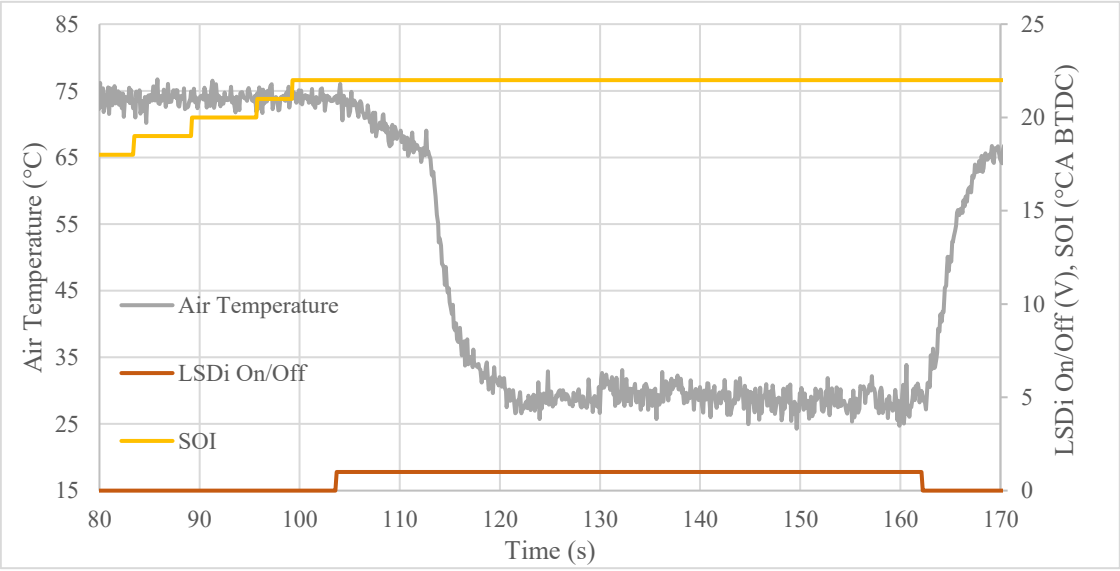

Figure 5-10: Drop in intake air temperature during LN_2 injection with compressed air of 5.5 barg.

As shown in Figure 5-11, when vapour propane steady-state testing was conducted under no-knock test conditions at an optimised SOI of 18° CA BTDC, the measured torque was observed to gradually decline over time. However, no significant changes were

reported in the intake air temperature, MAF, MAP, or diesel fuel pressure. After extensive investigation, it was determined that the pressure of the propane gas supplied from the 15 kg (net) propane tank was decreasing drastically, directly affecting the flow rate through the LPG injectors. This phenomenon is attributed to the high consumption of propane over a short period, which did not allow sufficient time for the latent heat to be transferred from the surrounding environment to be supplied to the liquid propane within the gas cylinder. Consequently, controlled heating had to be applied to the surface of the cylinder through partial submersion of the gas cylinder into a water tank during dual-fuel testing. Water was continuously circulated at room temperature to maintain stable propane pressure thereby ensuring a consistent gas flow rate. The implementation of this setup seen in Figure 5-12 was successful as the propane flow rate caused a stabilised torque.

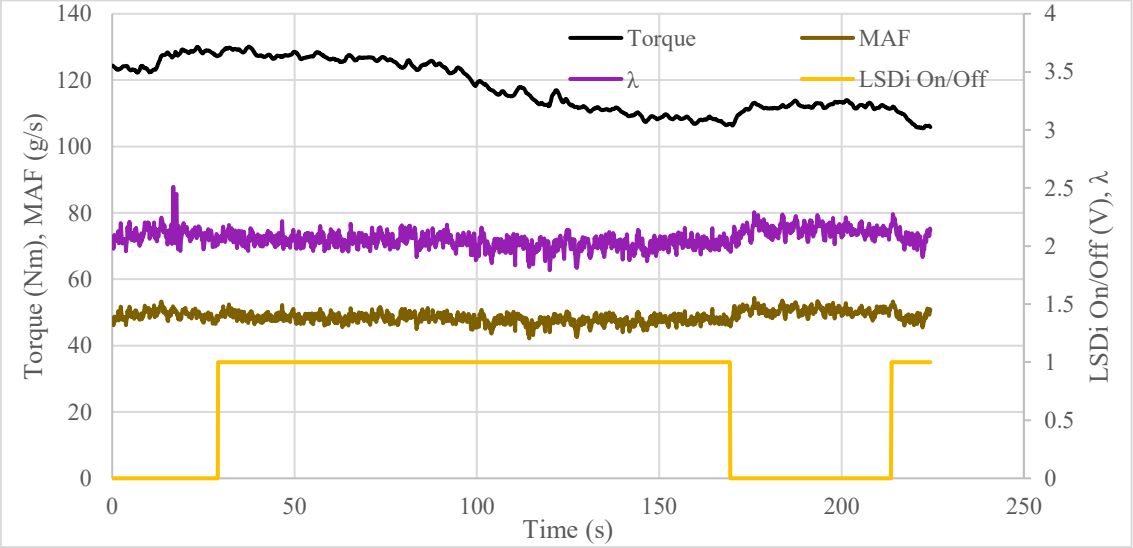

Figure 5-11: Reduction in torque during the steady LN_2 state.

Figure 5-12: Partially submerged gas tank cylinder in water.

As observed in Figure 5-11 the measured MAF was less than the initially calculated value of 0.0875 kg/s. This is a well-known phenomenon attributed to the injection of gaseous fuel, which reduces the volumetric efficiency of the engine [135] [90]. In addition, the MAF further decreased when LN_2 was injected which is likely attributed to the air displacement caused by N_2 expansion as it changes state to gaseous form. This reduction in MAF is also reflected in the calculated lambda where it is seen to increase slightly during the LN_2 injection. The final results of the LN_2 steady state test with the corresponding reduction in knock is presented in Section 7.1.

5.2 Dual-Fuel Testing with Liquid Propane

5.2.1 Liquid propane transfer unit

Due to safety concerns, the transportation and storage of LNG at the university were deemed unfeasible. Therefore, propane was selected as the preferred fuel to test the cryogenic fuel injection setup. Despite its properties differing considerably from LNG, experimentation with propane allowed for development of a reliable refilling procedure, thereby increasing confidence in the overall setup. To facilitate the filling of liquid propane into the 2-litre tank, an existing setup was utilised [136]. The schematic diagram and corresponding picture illustrated in Figure 5-13 and Figure 5-14 respectively, primarily consist of a refrigeration cycle, a vacuum pump, a storage tank, and a water reservoir. It is important to note that the 100-litre tank has two different outlet valves: a vapour outlet valve and a liquid outlet valve. More details about the exact functions of the different components of this setup are provided by Farrugia et al. [135].

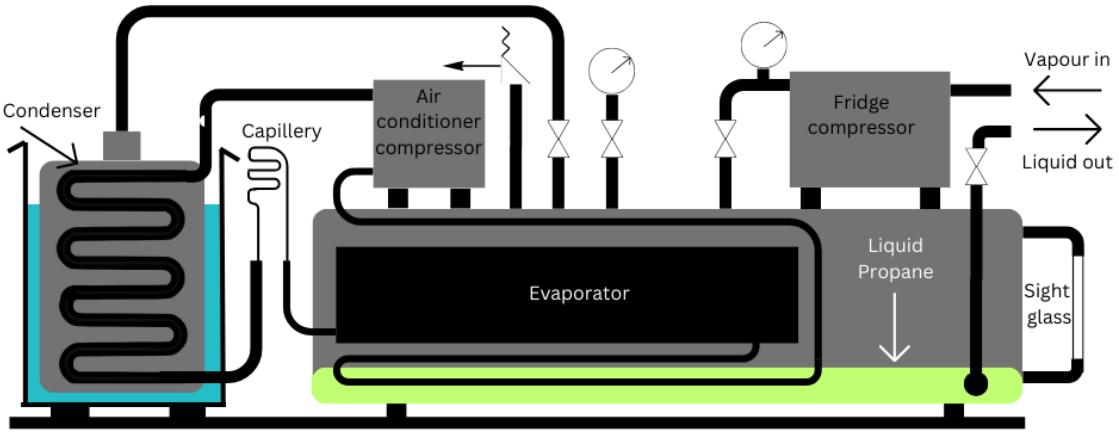

Figure 5-13: Schematic diagram of the LPG transfer unit.

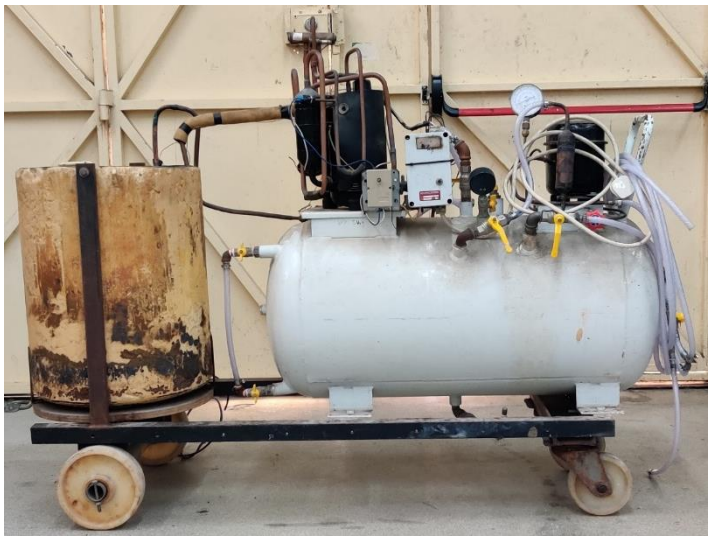

Figure 5-14: The LPG transfer unit.

5.2.2 Alterations of the cryogenic setup and its filling procedure

Figure 5-15 illustrates the cryogenic setup which was altered to accommodate the new working medium which is propane.

The pipe used to divert propane to the exterior in case of excessive pressure buildup

The manual shut off valve

Figure 5-15: Modified cryogenic setup for liquid propane injection.

The tray beneath the cryogenic solenoid valve was removed since no cooling of the solenoid valve is needed to inject liquid propane. A manual shut off valve was installed between the 2-litre tank and the solenoid valve providing the ability to isolate the liquid propane inside the 2-litre tank particularly in the event of solenoid valve damage or failure to close. The outlet of the pressure relief valve was routed outside the thermodynamics laboratory to prevent any accidental release of propane gaseous fuel indoors in case of excessive pressure buildup within the 2-litre tank. The insulation previously applied to the setup was removed as the 2-litre tank would be at equilibrium pressure (approximately 8 bar at ambient temperatures).

The LPG transferring unit was then used to fill up the 2-litre tank with liquid propane. Connections were made such that the liquid outlet from the filling system was attached to the top shut off valve while the vapour outlet was connected to the vent valve located at around 2/3 height of the 2-litre tank. In the first filling with propane after LN_2 use, the 2-litre tank was evacuated of any residual gases. Subsequently, liquid propane was allowed to flow thanks to the difference in pressure. The filling procedure was halted when liquid propane was observed flowing through the transparent tubing connected at the vent valve connection. The compressor integrated in the filling setup was then used to pump the propane from the supply lines back to the LPG transfer unit 100 litre tank. Therefore, after the filling procedure ends it can be concluded that the reservoir is consistently maintained at approximately 2/3 of its volume filled with liquid propane.

5.2.3 Liquid propane temperature drop

Unlike LN_2, when working with liquid propane precise amounts of liquid fuel had to be supplied to the intake manifold pipe to satisfy the desired SR and AFR of the operating test being carried out. Hence, the drop in temperature of the intake temperature would be fixed and dependent upon the mentioned parameters. This was found through first calculating the AFR of propane:

$$C_3H_8 + x\left(O_2 + \frac{79}{21}N_2\right) \rightarrow aH_2O + bCO_2 + dN_2 \tag{5.6}$$

Performing element balance:

$$C: 3 = b \qquad \& \qquad H: a = 4 \qquad \& \qquad O: x = 5$$

$$AFR_{volume} = \frac{5(1 + 1.\frac{79}{21})}{1} = \frac{23.8}{1}$$

$$AFR_{mass} = AFR_{volume} \times \frac{molar\ mass_{air}}{molar\ mass_{fuel}} = 23.8 \times \frac{28.97}{44.1} = \mathbf{15.6} \quad (5.7)$$

Based on previous testing, Azzopardi [91] and Scicluna [92] deduced that a 70% SR was needed to experience engine knock. However, due to the pilot diesel fuel needed to ignite the propane this value continues to change with the SR utilised during testing. Using previous trials [91], the minimum diesel fuel needed to ignite the gaseous fuel amounts to 0.76 g/s hence the propane mass flow rate would decrease to:

$$SR = \frac{\dot{m}_{propane} LHV_{propane}}{\dot{m}_{propane} LHV_{propane} + \dot{m}_{diesel} LHV_{diesel}} \quad (5.8)$$

$$0.7 = \frac{\dot{m}_{propane} \times 46.296 \times 10^6}{(\dot{m}_{propane} \times 46.296 \times 10^6 + 0.76 \times 10^{-3} \times 42.791 \times 10^6)}$$

$$\dot{m}_{propane} = \mathbf{0.0016\ kg/s}$$

Hence, the temperature drop caused by this amount of propane flow rate results to:

$$\dot{m}_{propane} h_{fg} = \dot{m}_{air} C_p \Delta T \quad (5.9)$$

$$\Delta T = \frac{0.0016 \times 0.426 \times 10^6}{0.0875 \times 1005} = \mathbf{7.75}\ ^\circ\mathrm{C}$$

5.2.4 Liquid propane orifice resizing

The previous orifice sizing calculations done in Section 5.1.3 were performed for LN_2 as a medium. Hence, a flow test was carried out with liquid propane using the previously installed LN_2 orifice and controlling the flow via PWM. Measures were taken to avoid any drops in pressure inside the 2-litre tank caused by the unavoidable time required for the liquid propane to get the latent heat needed to change its state during the injection of liquid propane. The 2-litre tank was supplied with compressed gaseous propane in order to maintain the equilibrium pressure inside the 2-litre tank at all times. To perform the flow test, the same apparatus used by Fenech [90], Azzopardi [91] and Portelli [89] during gaseous flow tests were used. However, a water heat exchanger was installed in

series to provide the latent heat to any liquid propane which might not have yet changed to its gaseous state as shown in the schematic Figure 5-16.

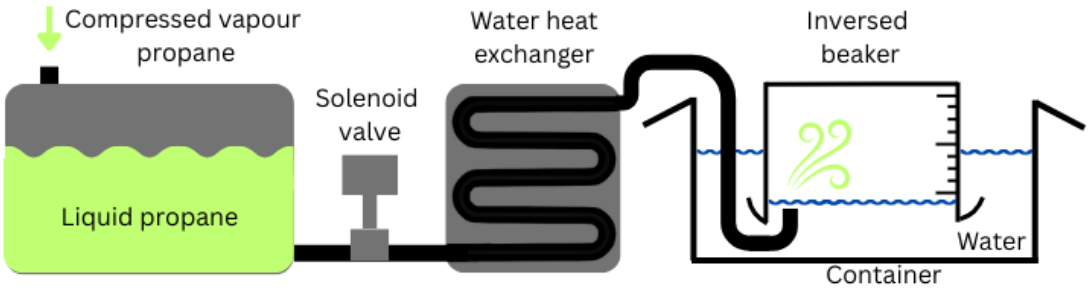

Figure 5-16: Liquid propane flow test apparatus.

As deduced from the gradient of the flow test results presented in Figure 5-17, the flow rate of the cryogenic solenoid valve with the LN_2 sizing orifice was of 6.2 g/s of liquid propane. Although the flow rate of liquid propane was greater than it was required of 1.6 g/s calculated in Section 5.2.3, a steady test was performed where both the injection frequency and duty cycle was varied and minimised to compensate for the larger flow rate. It is important to note that the solenoid valve exhibits a minimum Duration Of Injection (DOI) of approximately 25 ms – any shorter DOIs than this threshold would result in the valve failing to fully open.

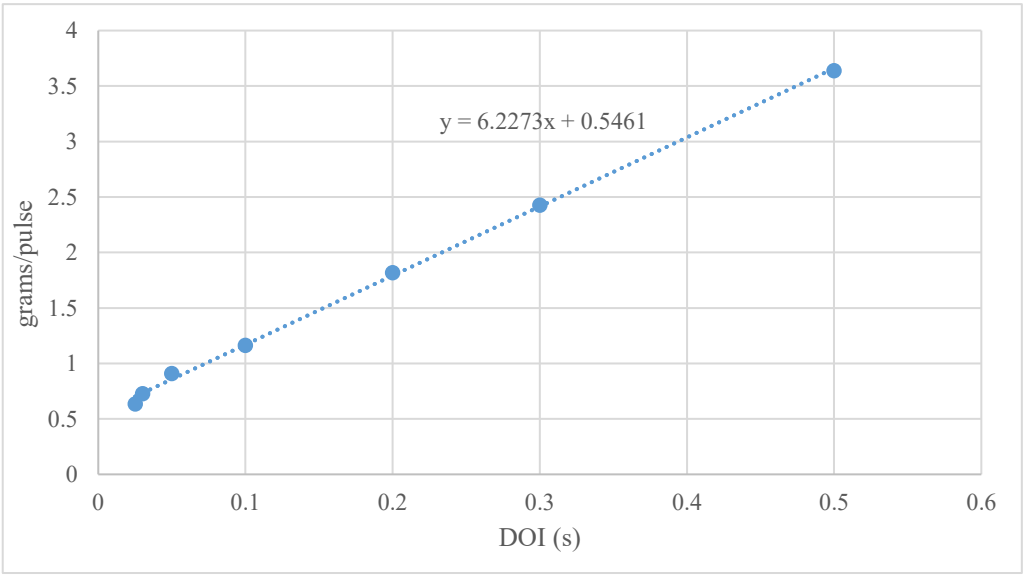

Figure 5-17: Flow rate of propane with LN_2 sized orifice.

The relationship between the DOI, injection frequency and duty cycle is given by:

$$DOI\ (s) = \%\ Duty\ cycle \times \frac{1}{f} \tag{5.10}$$

As illustrated in Figure 5-18 the in-cylinder pressure measurement reveal that the engine failed to maintain steady operation due to the cycle variation in peak in-cylinder pressure. This instability was primarily caused due to the slow frequency of the cryogenic solenoid valve (max 2.5 Hz) which caused inconsistent fuel delivery leading to cycle-to-cycle variations; some cycles failed to ignite due to insufficient delivery of gaseous propane.

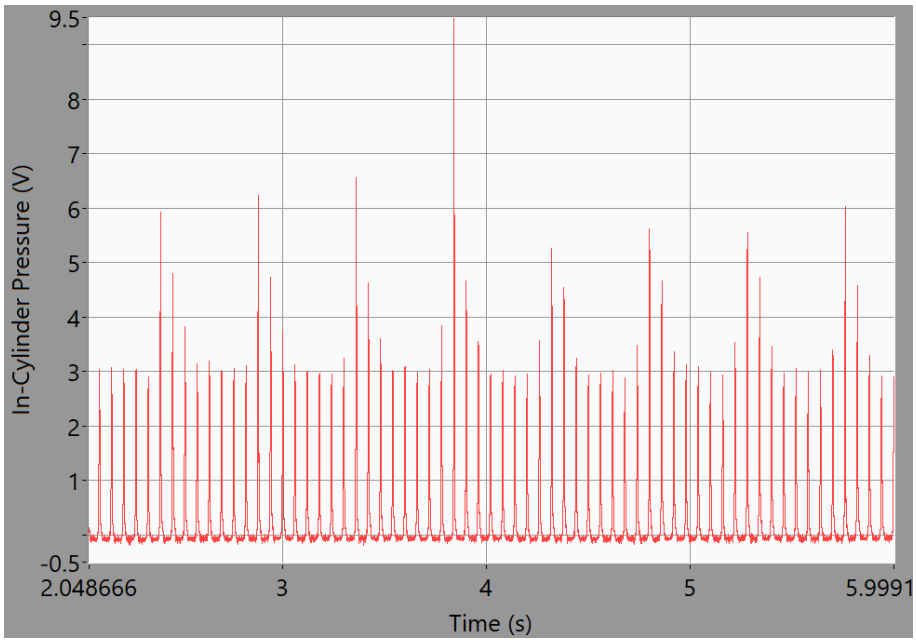

Figure 5-18: In-cylinder pressure variations.

Increasing the DOI alone was insufficient to resolve this issue without simultaneously increasing the injection frequency. Maintaining a low frequency while extending the DOI would lead to excessive fuel delivery during certain cycles, causing SRs to exceed the desired target values and further compromising combustion stability.

Therefore, the optimal solution involved reducing the orifice size and slightly increasing the solenoid valve frequency. Reducing the orifice size lowered the instantaneous flow rate, permitting the valve to operate at higher duty cycles and longer DOIs, ensuring reliable valve opening within its mechanical response limits. Increasing the frequency reduced the interval between injections, enhancing fuel distribution uniformity and combustion stability across engine cycles. This phenomenon can be explained by the valve's mechanical and electromagnetic limitations where the solenoid valve requires a

minimum pulse width to fully open, and operating at low frequencies with large orifices forces the system to use very low duty cycles to avoid over fuelling. Such low duty cycles correspond to injection durations below the valve's minimum response time, resulting in incomplete or failed injections.

Due to the large internal geometry of the cryogenic solenoid valve, the maximum achievable operating frequency was low; not more than 3.4 Hz. It is important to appreciate that such low frequency compared to the typical experimentation engine speed of 2000 RPM is relatively low and can only be used since this setup is port fuel injected. The frequency of the solenoid valve can only be reduced if the amount of fuel injected per cycle is increased to compensate for the lower frequency. Given this frequency constraint, it became necessary to optimise the orifice size to ensure that the minimum DOI of 25 ms could be reliably achieved across the range of duty cycles required to achieve the desired SRs and fuel mixtures. Hence, the orifice diameter (d_t) was determined accordingly by using (5.3) [133], where the saturation pressure and density of liquid propane at ambient conditions was taken to be approximately 8.1 bar and 500 kg/m^3.

$$A_t = \frac{\dot{m}_{propane}}{c_d\sqrt{2\rho\Delta p}} = \frac{0.0016}{0.65\sqrt{2 \times 500 \times 8.1 \times 10^5}} = 8.65 \times 10^{-8}\ m^2$$

$$d_t = \sqrt{\frac{4 \times 2.7 \times 10^{-6}}{\pi}} = \mathbf{0.32\ mm}$$

It was decided that a slightly larger orifice of 0.4 mm was used and from testing the frequency of the solenoid valve was set to 3.4 Hz. Operating at this injection frequency was found to have an improvement significantly improved the consistency of the maximum in-cylinder pressure between consecutive injections, thereby enhancing combustion stability. This was only possible due to correct sizing of the orifice which was adequate to operate within regimes requiring injection durations greater than the minimum DOI, thereby preventing injector opening failures associated with shorter pulses. As a result, this orifice size achieved a suitable compromise between maintaining sufficient instantaneous flow and ensuring reliable valve actuation at the specified

frequency. The corresponding flow characteristics for this orifice size are illustrated in Figure 5-19.

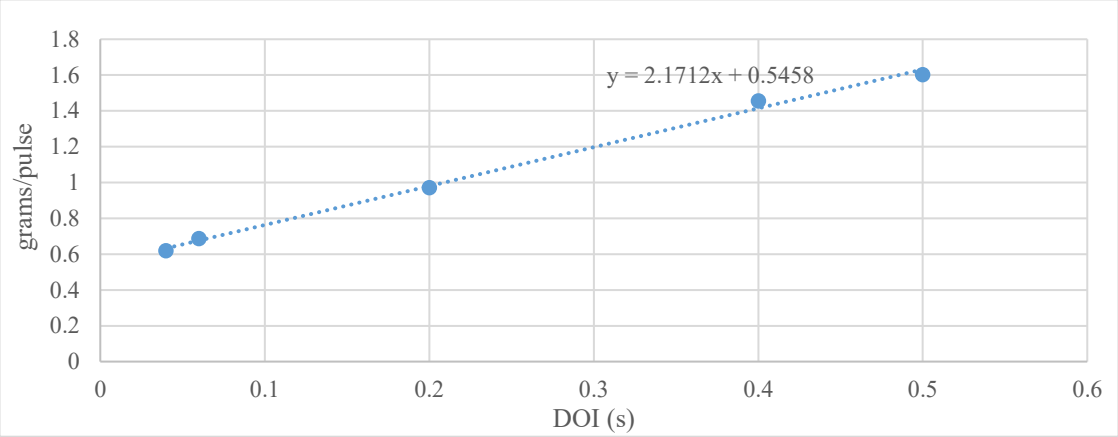

Figure 5-19: Liquid propane flow rate with 0.4 mm orifice.

5.2.5 MoTec knock signal calibration

The MoTec 53116 SKM knock signal DAQ system, previously installed and used by Azzopardi [91], was calibrated using measured in-cylinder pressure oscillations. These oscillations were from in-cylinder pressure measurements taken with the AVL GH14P pressure sensor. The AVL FI PIEZO amplifier (2P2G) was set to have the low pass filter to 50 kHz. The sensor was left installed in cylinder number 3 (instead of the glow plug), as preliminary tests by Azzopardi [91] determined this cylinder to be the most prone to knocking. The LabVIEW VI, previously prepared by Scicluna [92], was used to extract in-cylinder pressure segment where knocking occurred as depicted in Figure 5-20. A test exhibiting the highest recorded knock was selected for this calibration.

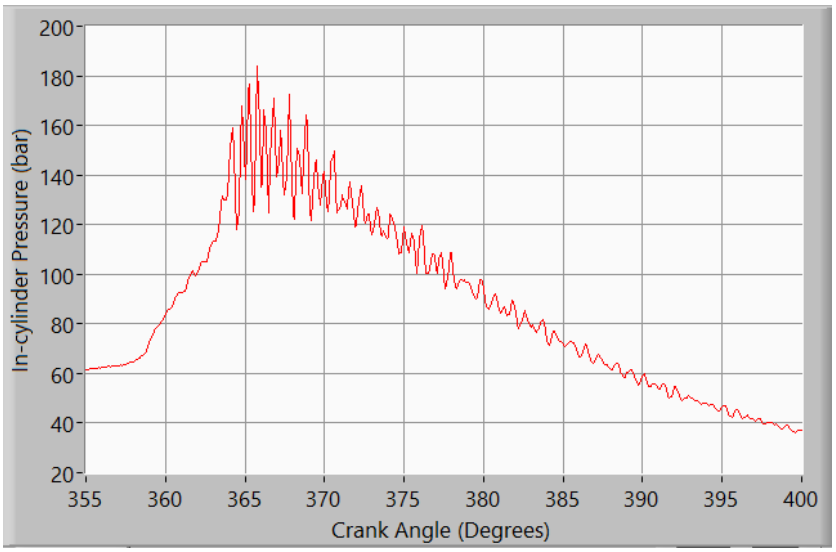

Figure 5-20: Segment of in-cylinder pressure measurement highlighting the occurrence of knock.

The Maximum Amplitude of Pressure Oscillation (MAPO) was subsequently calculated from the extracted portion of the pressure signal. The MAPO was found from the in-cylinder pressure signal after applying a band-pass filter set between 3 kHz and 10 kHz, as recommended by Sementa et al. [61]. The maximum amplitude of the resulting high-frequency signal was selected as illustrated in Figure 5-21. Since knock occurs randomly, MAPO was computed for each individual cycle, and the mean value was then derived over all cycles. The mean MAPO value obtained was of 9.6 bar with a Coefficient Of Variation (COV) of 0.3, which was calibrated against the measured MoTec knock mean signal of 40.1 with a COV of 0.1. The knock results presented in Table 7-1 and Table 7-2 in Section 7.3 are based on this calibration.

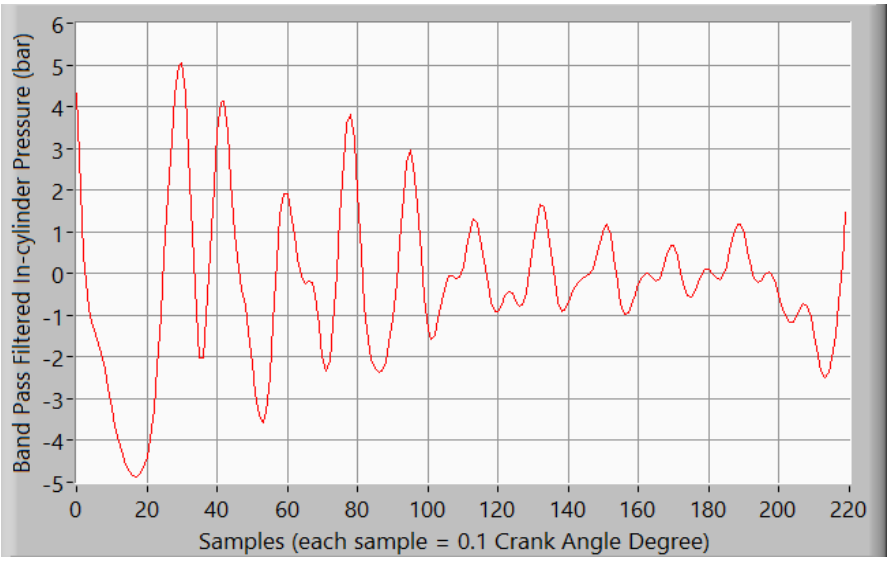

Figure 5-21: Band pass filter applied to the segment of the in-cylinder pressure signal.

5.3 Closing Remarks

Appropriate apparatus was procured to construct the cryogenic setup. This setup was primarily designed to support the injection of LNG into the intake manifold, however, due to safety concerns related to fuel storage, LNG injection was not possible. To assess the cryogenic performance of the whole setup, LN_2 was used and injected inside the intake manifold resulting in a consistent drop in temperature of approximately 45 °C. Additionally, an orifice size of 0.4 mm was decided for LN_2 injection and the solenoid frequency was set to 3.4 Hz. Finally the MAPO was calculated and used to calibrate the MoTec knock signal.

Chapter 6. H_2 Analysis Results

From the performed experiments listed in Table 4-2, Table 4-3 and Table 4-4 presented in Section 4.3, several combustion characteristics where studied and are presented in this chapter according to the chosen literature identified in Chapter 3. The COV of each parameter presented in this chapter are listed in the different fuel tables presented in Chapter 10. Each graph displays results from three fuels: petrol, represented by the colour blue; propane, represented by green; and H_2, represented by red and orange for λ values of 2 and 3 respectively, at different MAP values. The MAP is the widely accepted load parameter used in technical and academic literature where it represents the different loads which are a function of the throttle position This combustion characterisation is essential for understanding the differences between H_2 combustion and that of traditional fossil fuels. With this knowledge, the direct implementation of H_2 in DFEs can be facilitated more easily during the transition and integration of H_2 into existing infrastructure.

6.1 Measured Torque from Load Cell

Figure 6-1 depicts the variation of the measured torque from the load cell at different MAP values.

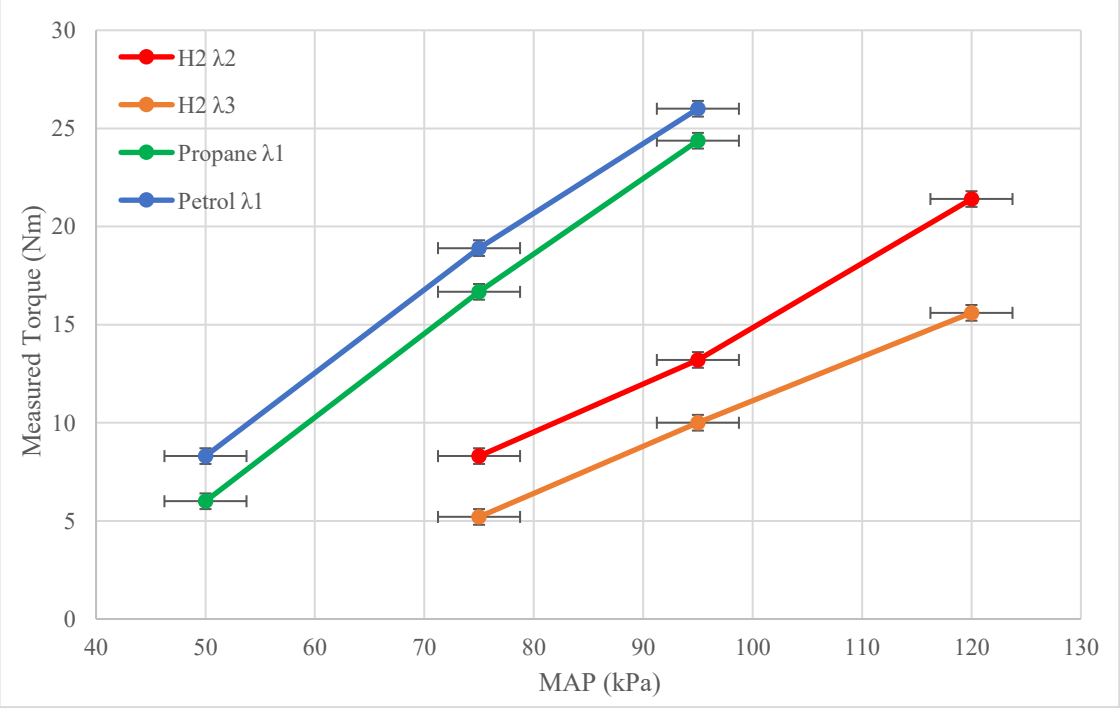

Figure 6-1: The variation of the measured torque with MAP.

The highest torque obtained was 26 Nm with petrol fuel at a MAP of 95 kPa with a spark timing of 20° CA BTDC. Although propane has a higher calorific value, it did not produce higher torque than petrol at any tested MAP and obtained a maximum torque of 24 Nm at a spark timing of 20° CA BTDC. In contrast to petrol, propane was injected in a vapour state, thereby eliminating the need for vaporisation and facilitating more effective mixing with the intake air. The observed slight difference in torque may be attributed to a minor decrease in MAF, potentially resulting from the volumetric displacement caused by the injected propane vapour within the intake manifold. This directly affects the volumetric efficiency of the engine, a phenomenon well documented by Hashem et al. [137] who reported a 4.65% reduction with the use of LPG compared to petrol. This reduction in the volumetric efficiency is also noted by Farrugia and Briffa [135] during a similar LPG conversion.

During testing, H_2 in both λ2 and λ3 mixtures produced less torque when compared to the stoichiometric mixtures of propane and petrol fuels. Despite performing boosted conditions of 120 kPa during H_2 testing, the maximum torque obtained during λ2 mixtures was approximately 22 Nm and 16 Nm for the leaner λ3 mixture. Similarly, despite H_2 having a higher calorific value, H_2 displaces large amounts of air due to its low density and diffusivity characteristics highly impacting the volumetric efficiency of the engine, as presented by Fenech [90]. The primary reason for the reduced torque output is attributed to the lean air/fuel ratio employed during the H_2 experimentation. If a stoichiometric H_2 mixture had been used, the torque generated would likely have been higher. However, tests involving H_2 stoichiometric mixtures were not conducted, since abnormal combustion is experienced as highlighted by Fenech [90].

6.2 Torque calculated from Indicated Work

The indicated work was calculated using the measured in-cylinder pressure using (4.8). Since the measured torque from the load cell results from the indicated work by the piston, the characteristics of the curves presented in Figure 6-2 are similar to those depicted in Figure 6-1. Additionally, the torque was calculated from the indicated work and compared to the measured torque as illustrated in Figure 6-3. As expected, the torque derived from the indicated work is higher than the torque measured from the load cell. This is due to frictional losses which act on the piston crank assembly and the friction work is deducted from the “gross available” work on the piston termed the indicated

work. However, the similar characteristics observed between Figure 6-1 and Figure 6-3, support the validity of the indicated work values obtained through post processing, since these curves were generated from two distinct methods.

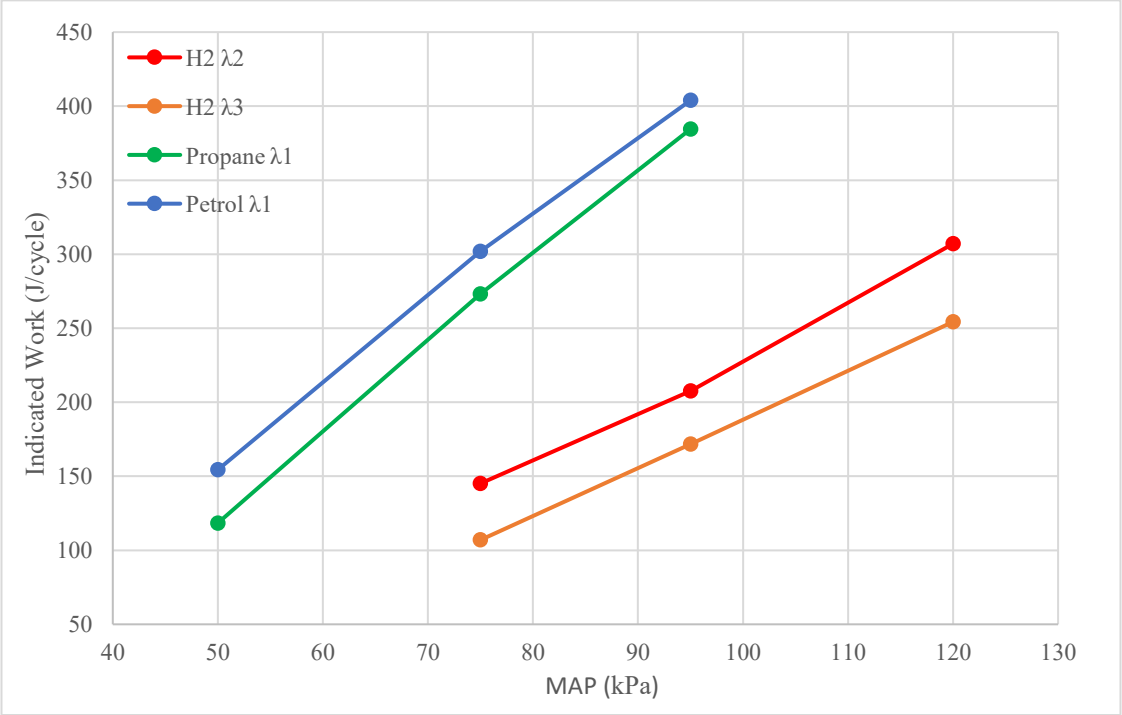

Figure 6-2: The variation of the indicated work with MAP.

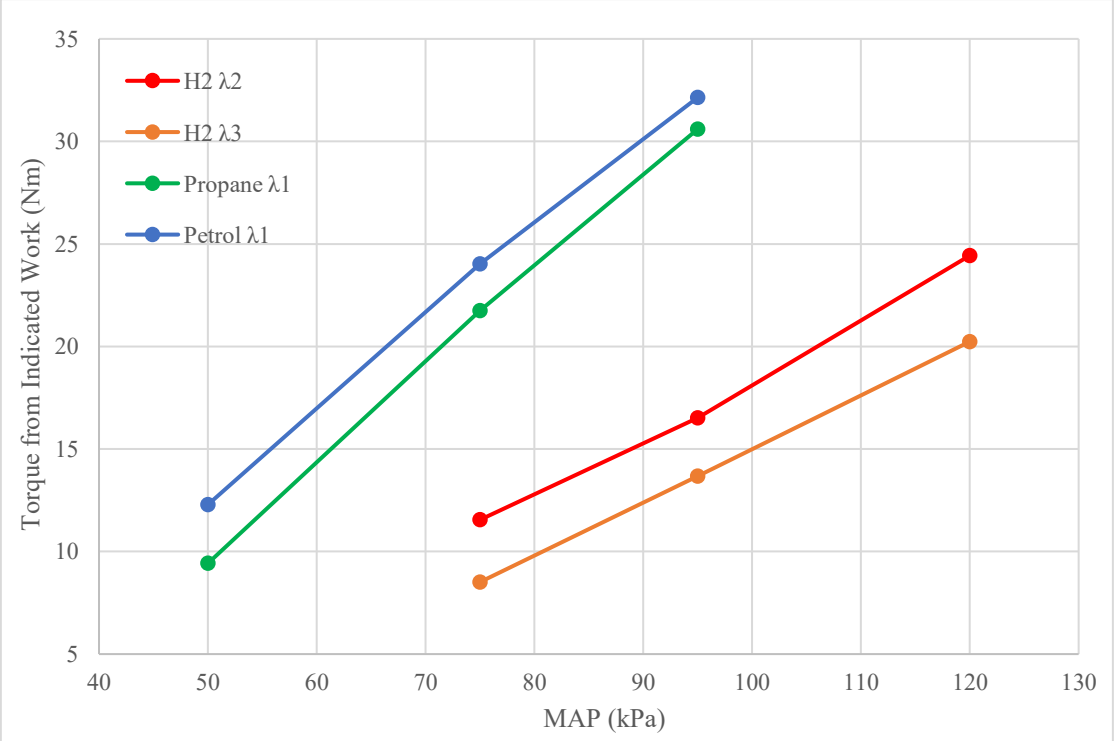

Figure 6-3: The variation of the torque with MAP calculated from the indicated work.

6.3 Brake Thermal Efficiency

The variation of the Brake Thermal Efficiency (BTE) with different MAP values is presented in Figure 6-4. Comparing the BTE of the three fuels shown in Figure 6-4, H_2 λ3 mixture yielded the lowest efficiency at a MAP of 75 kPa which may be attributed to the air displacement due to H_2 injection. However, H_2 during λ2 mixture, obtained the highest value of 23% during the λ3 mixtures, compared to 21% for petrol and propane fuels at wide open throttle. Despite producing less torque than petrol and propane, H_2 exhibited superior thermal efficiency. This indicates that H_2 converts a greater proportion of the fuel's energy into mechanical work, suggesting a more thermodynamically efficient combustion process. This is likely due to its higher calorific value and faster flame speed [64].

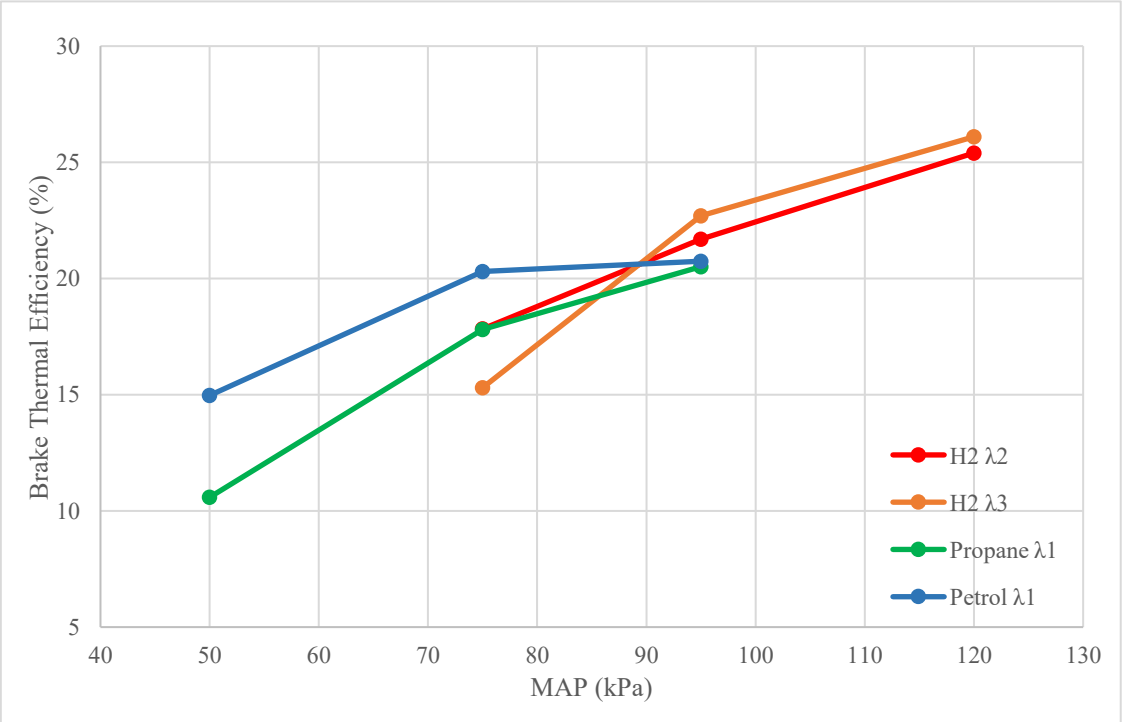

Figure 6-4: The variation of the BTE with MAP.

6.4 In-cylinder Pressure Values

All presented combustion characteristics were derived from in-cylinder pressure measurements. The in-cylinder pressure measurements for a MAP of 75 kPa are shown in Figure 6-5, while those for 95 kPa are presented in Figure 6-6. Since no 50 kPa test were conducted for H_2 and no 120 kPa tests were performed for petrol, these conditions were combined and presented in Figure 6-7.

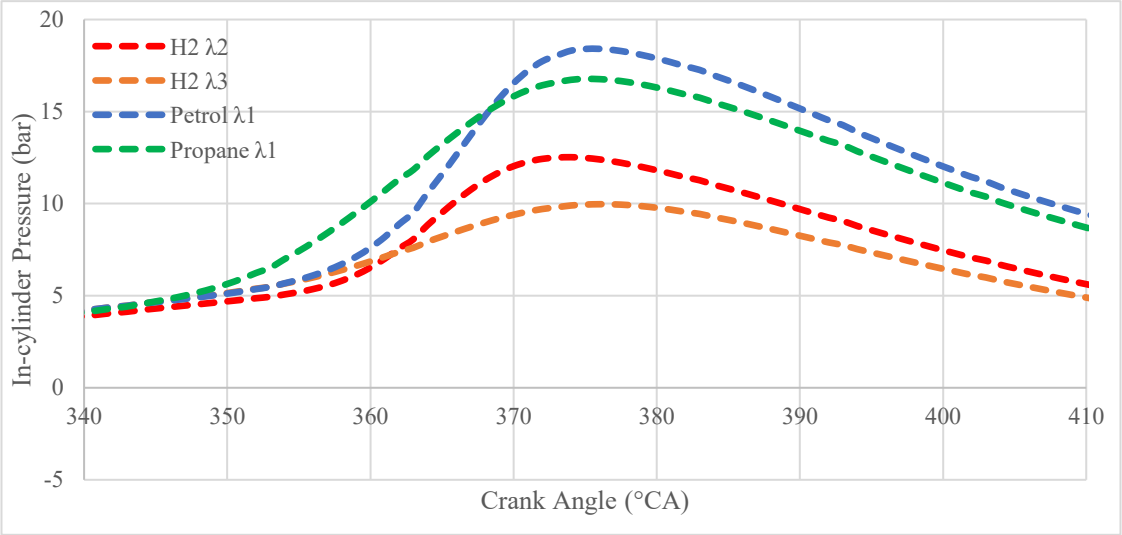

Figure 6-5: The variation of in-cylinder pressure with crank angle at a MAP of 75 kPa.

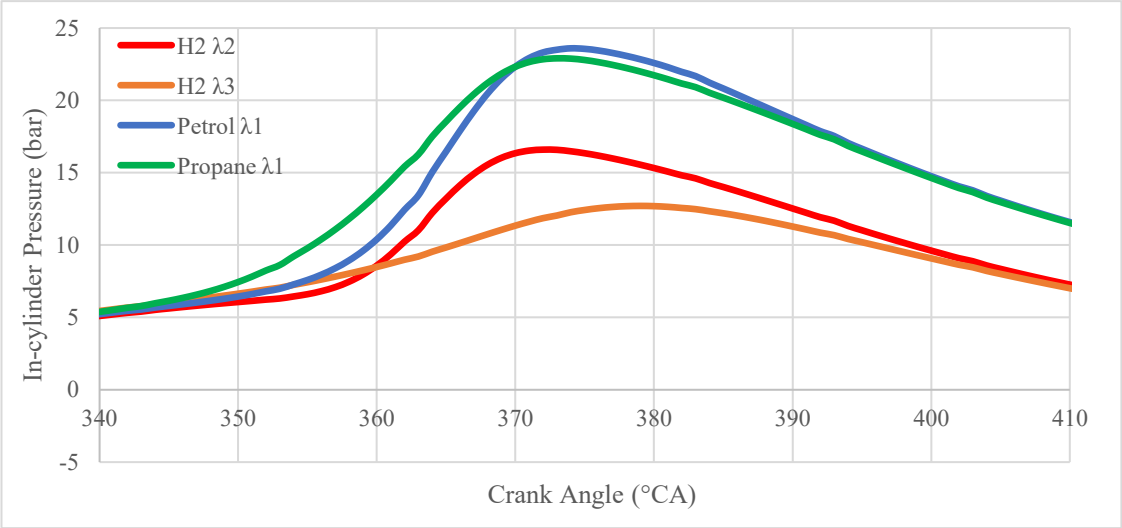

Figure 6-6: The variation of in-cylinder pressure with crank angle at a MAP of 95 kPa.

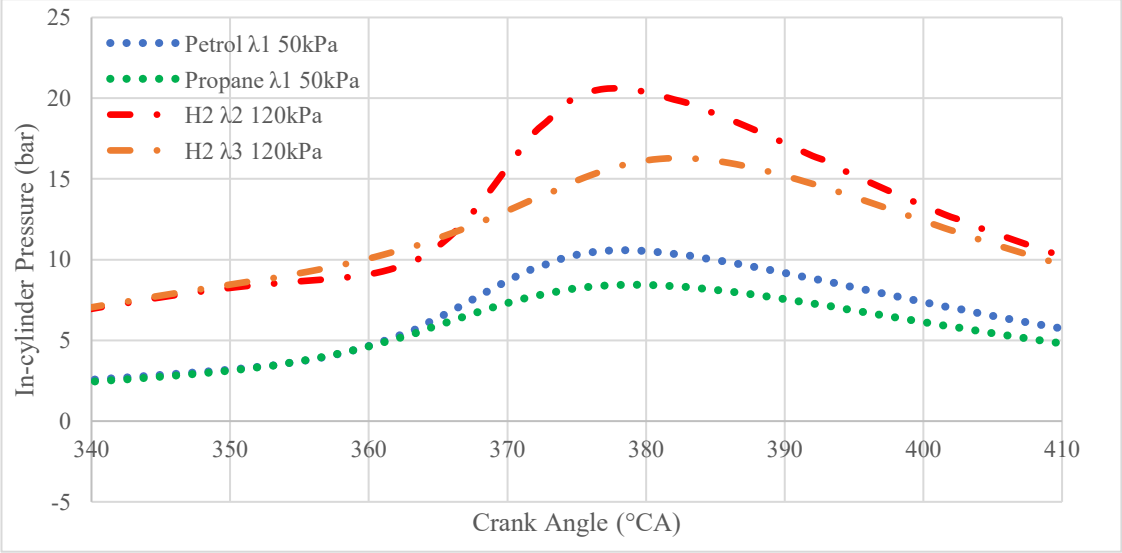

Figure 6-7: The variation of in-cylinder pressure with crank angle at MAPs of 50 kPa and 120 kPa.

By observing the shape characteristic of the in-cylinder pressure curves, several conclusions can be drawn. The most straightforward observation is that increasing the MAP results in higher in cylinder pressures. As noted by Molina et al. [59] and Sementa et al. [61], during dilute conditions the curves widen and flatten due to low in-cylinder pressures and longer burn durations. Additionally, the rate of pressure increase, which corresponds to the rate of heat release is lower for leaner mixtures. As clearly shown in Figure 6-11, petrol exhibits the highest rate of heat release, a conclusion that is supported by the steep gradients observed in the petrol pressure curves.

6.5 Mass Fraction Burned

As explained in Section 3.5, two MFB approaches were described and tend to yield different maximum MFB values which can evidently be seen through Figure 3-2. Hence, the MFB approach presented by Pipitone described in (3.16) had to be normalised to find the different combustion crank angles as presented in Section 6.8. The combustion characteristic which can be observed from these curves is the rate of heat released which will be discussed in Section 6.6. The Rassweiler and Withrow MFB curves for a MAP of 75 kPa are shown in Figure 6-8, while those for 95 kPa are presented in Figure 6-10. Since no 50 kPa test were conducted for H_2 and no 120 kPa tests were performed for petrol, these conditions were once again combined and presented in Figure 6-9.

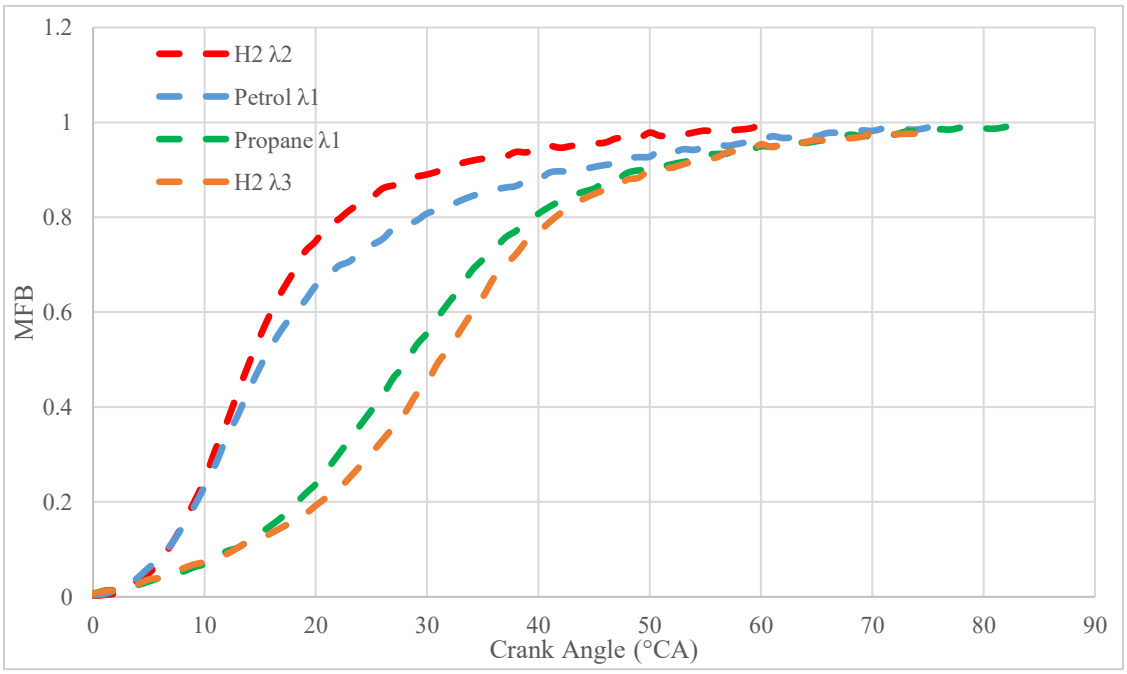

Figure 6-8: The variation of MFB with crank angle at MAPs of 75 kPa.

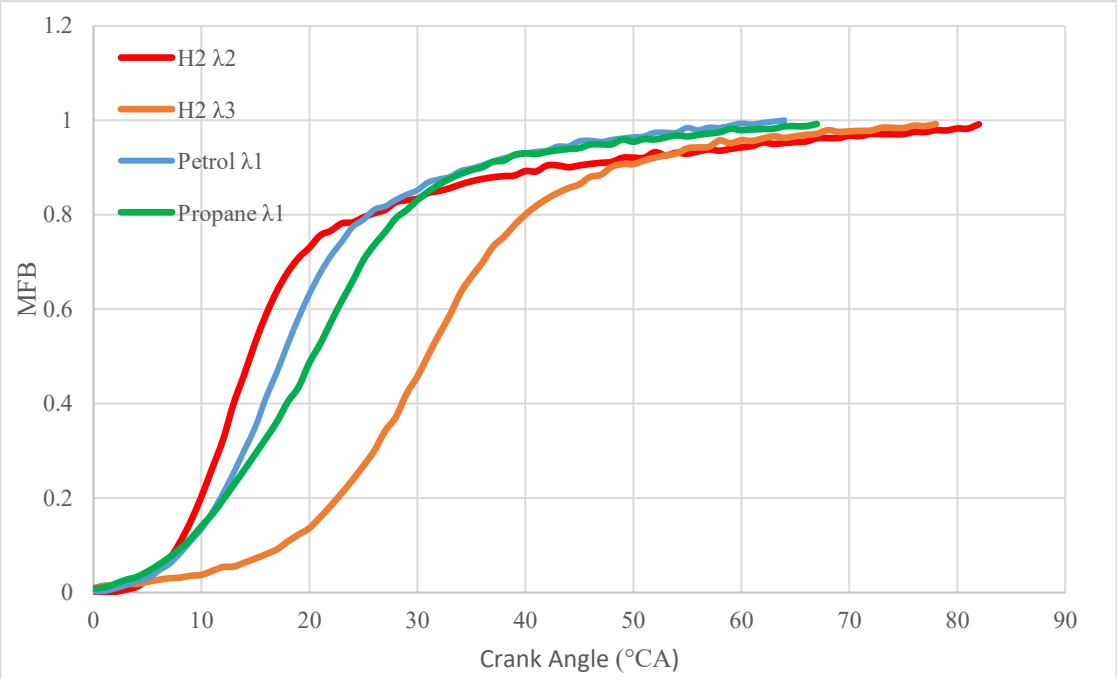

Figure 6-10: The variation of MFB with crank angle at MAPs of 95 kPa

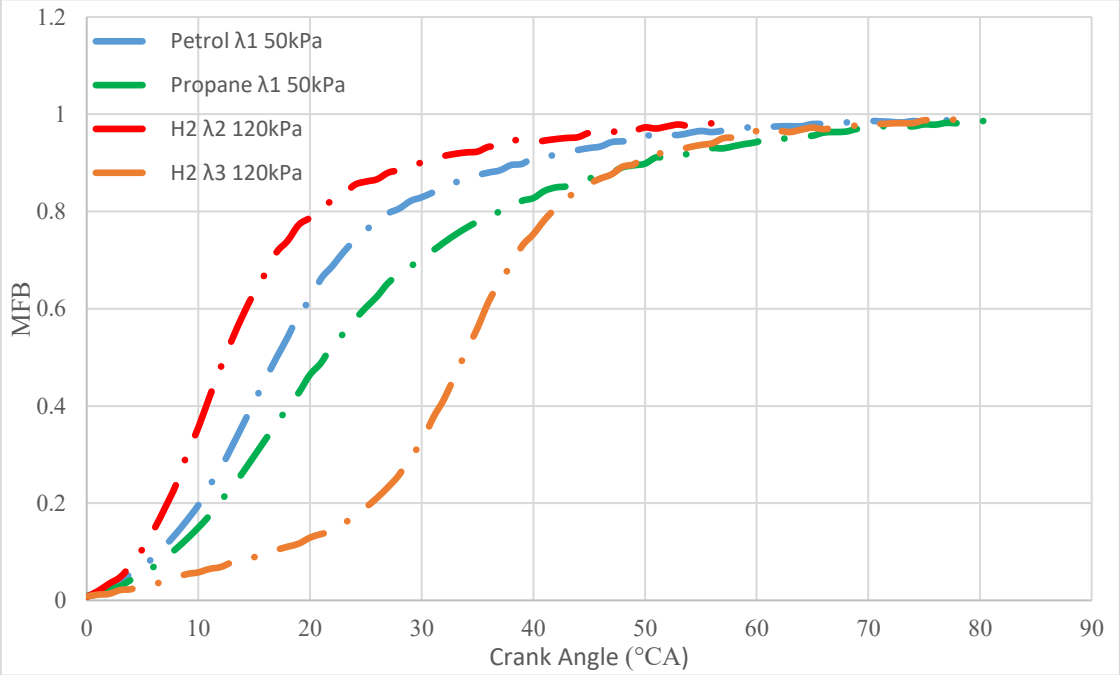

Figure 6-9: The variation of MFB with crank angle at MAPs of 50 kPa and 120 kPa

6.6 Peak Net Heat Release Rate

Among the two approaches for calculating the net HRR described in Section 3.1, the data calculated using (3.5) was plotted, as this method is an improved version over (3.1), as previously discussed. Figure 6-11 depicts the calculated peak net HRR variation against MAP.

The net HRR is directly correlated with the rate of change (gradient) of the MFB curves presented in the previous section. The highest peak net HRR obtained was observed during petrol testing where it developed the highest net HRR of 58 J/°CA. This elevated net HRR is one of the reasons for petrol to produce the highest torque.

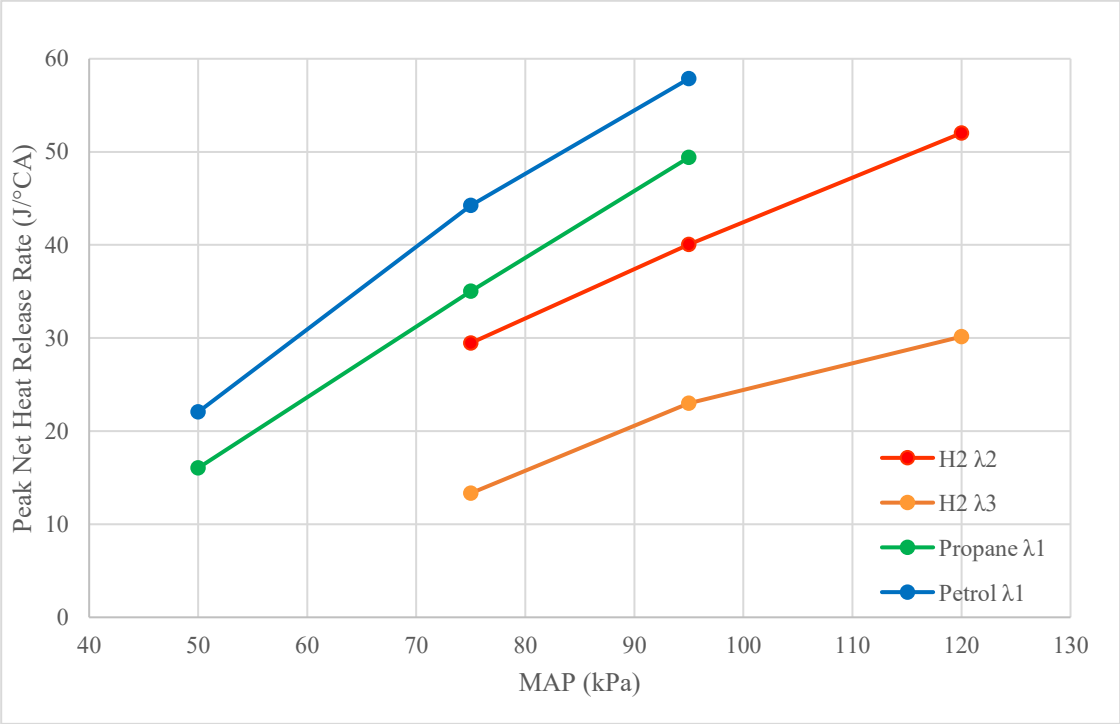

Figure 6-11: The variation of the peak net HRR with MAP using the (3.5) approach

It is important to recognise that H_2 appears to develop high net HRRs compared relative to the torque it produced. This high peak net HRR might be attributed to H_2's enhanced flame propagation which accelerates combustion [87]. Ma et al. [138] argued that the peak net HRR is influenced by the ignition timing, and a delayed ignition timing in certain instances can be beneficial for increasing the peak instantaneous net HRR, as combustion is improved due to additional allocated mixing time. Since, a late ignition advance of 10° CA BTDC was used during H_2 testing at a MAP of 95 kPa with a λ2 mixture , this may explain the observed high peak net HRR. However, as deduced from the spark sweeps shown in Figure 4-8, later spark timings beyond the MBT timing of 10° CA BTDC seem to have an insignificant effect on producing additional torque. This implies that torque is not solely determined by the peak net HRR caused by the fuel but rather by the cumulative heat release as explained in the following section.

6.7 Cumulative Net Heat Release Rate

The cumulative heat release for different MAP values is shown in Figure 6-12. Only the values obtained using Pipitone and Beccari's [72] approach, as presented in (3.5) were plotted because negligible differences were observed compared to Stone's [96] approach, presented in (3.1).

The cumulative heat release was primarily computed to evaluate the energy losses which is described in (3.9) in Section 3.2. The cumulative heat release represents the gross thermal energy released from the fuel combustion during the engine cycle. It is noted that from this thermal energy released into the gases, heat, pumping and friction losses reduce the energy converted into work. Therefore, the magnitude of the cumulative heat release is higher than that obtained from the indicated work depicted in Figure 6-2. According to Eastop and McConkey [139] and Heywood [49], approximately 35% of the total energy fuel inputted in an internal combustion engine is converted into actual shaft or brake work, commonly expressed as brake horsepower. Therefore, when friction is subtracted from the indicated work, similar percentage values are obtained were approximately 30% of the cumulative heat release is converted into usable torque.

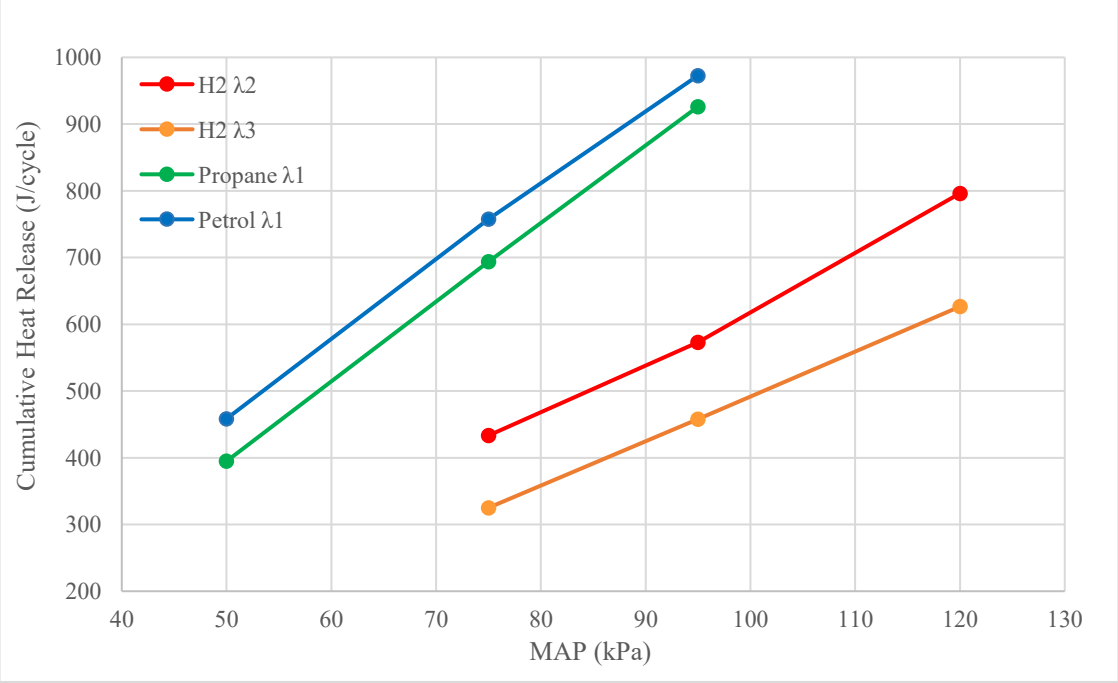

Figure 6-12: The variation of the cumulative heat release with MAP.

6.8 CA10, CA50 and CA90 Locations

The combustion locations CA10, CA50 and CA90 are presented in separate graphs. As explained in Section 3.5, two approaches were used to obtain the MFB profile and from which these combustion locations can be determined. Figure 6-13 presents the CA50 locations obtained with the Rassweiler and Withrow approach presented in (3.11), while Figure 6-14 presents the CA50 crank angles by utilisation of the Roger's approach presented in (3.16).

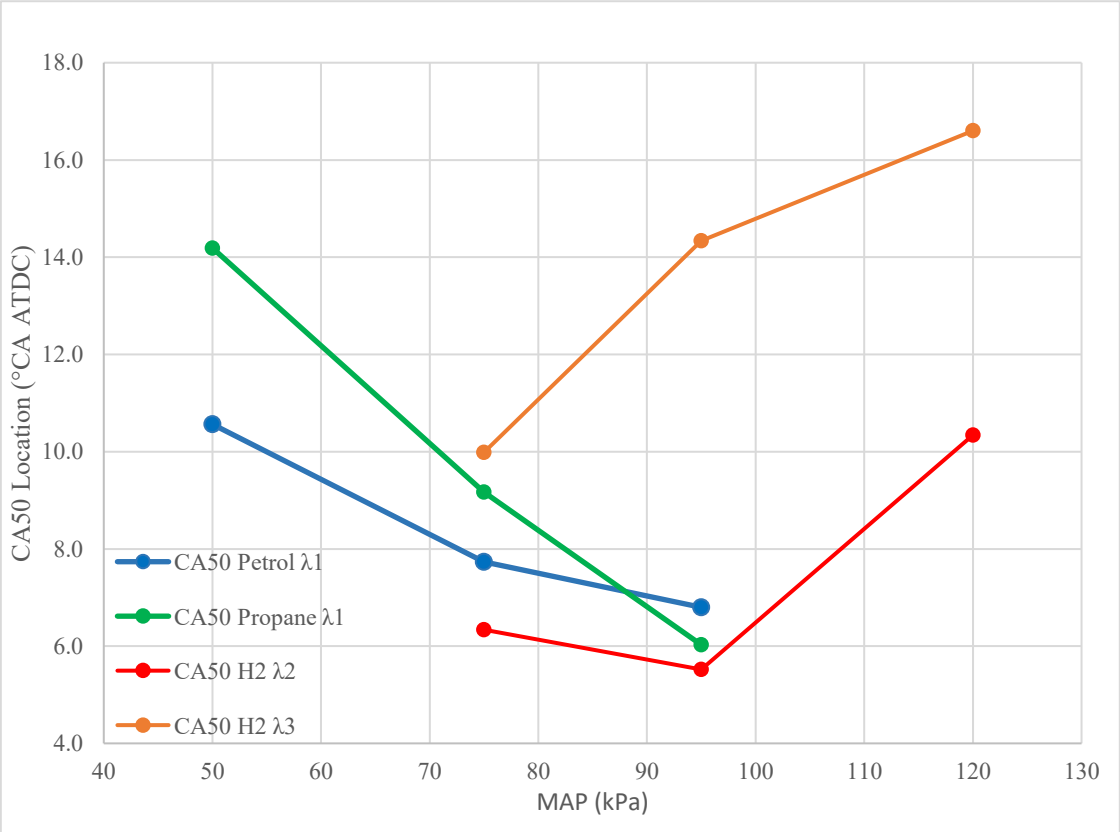

Figure 6-13: The variation of CA50 locations with MAP using the Rassweiler and Withrow approach presented in (3.11).

The CA50 positions for all fuels, as derived from both approaches, appear to be very similar. For tradional fuels, the main observation is that an increase in MAP corresponds to the CA50 position occuring earlier with respect to TDC. When analysing these combustion locations it is important to consider the ignition advance used, which as shown in Table 4-3 and Table 4-4 was earlier only during the test at the 50 kPa MAP. Morever, although the same ignition advance was used for MAPs of 75 and 95 kPa, the resulting CA50 positions differed.

Opposite behaviour was noticed from H_2 analysis in both mixtures, where the CA50 location appeared to occur later as MAP increased. As expected, the CA50 location for leaner mixtures occured later both due to the later ignition advance used and due to the slower combustion rate. However, during the MAP test of 95 kPa, as shown in Table 4-2, the same ignition advance of 10° CA BTDC was used. However, the CA50 position differed further highlighting the slower burn rate when a leaner mixture was used. Similarly, the CA50 locations observed align closely with those reported by Molina et al. [59] in Figure 2-9 during low load conditions.

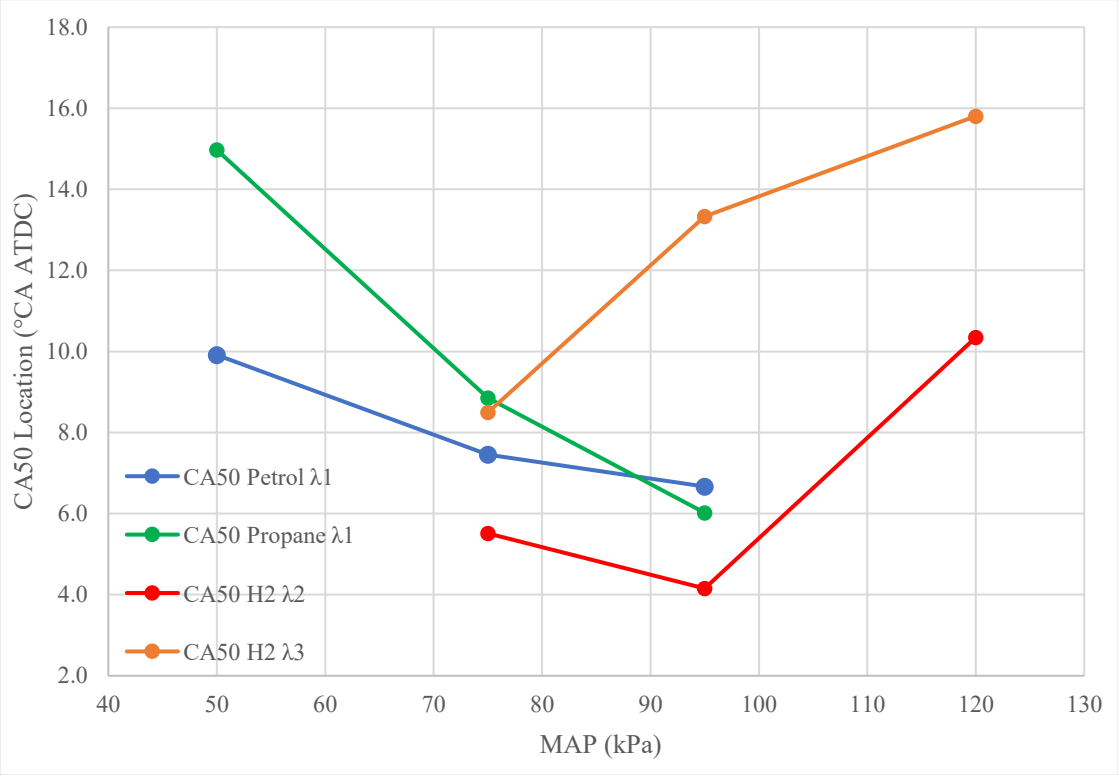

Figure 6-14: The variation of CA50 locations with MAP obtained using the Roger's approach presented in (3.16).

For higher loads, comparisons were made with results obtained by Rrustemi et al. [60] who reported a CA50 of 10° CA ATDC at a MAP of 95 kpa for λ2 mixtures. At a MAP of 120 kPa and λ2 mixture, a CA50 of 22° CA ATDC was reported, which differs from the values obtained during experimentation. Rrustemi et al. [60] did not perform investigations beyond λ2.6; therefore comparisons for λ3 values cannot be made. On the other hand, Sementa et al. [61] obtained CA50 locations similar to those depicted in Figure 6-13 and Figure 6-14 . At a MAP of 100 kPa for λ2 mixtures, a CA50 of 8° CA ATDC was reported and for λ3 mixtures, a CA50 of 11° CA ATDC was obtained.

The CA10 and CA90 locations were determined from the two approaches to compute the fast burn duration, as discussed in Section 6.9. As observed from the CA50 locations reported in Figure 6-13 and Figure 6-14, the two approaches yielded similar values; hence it was decided to present only the values calculated using the (3.16) approach for the burn duration. The fast burn duration was computed as described in Section 3.7 and the corresponding CA10 and CA90 positions used are depicted in Figure 6-15.

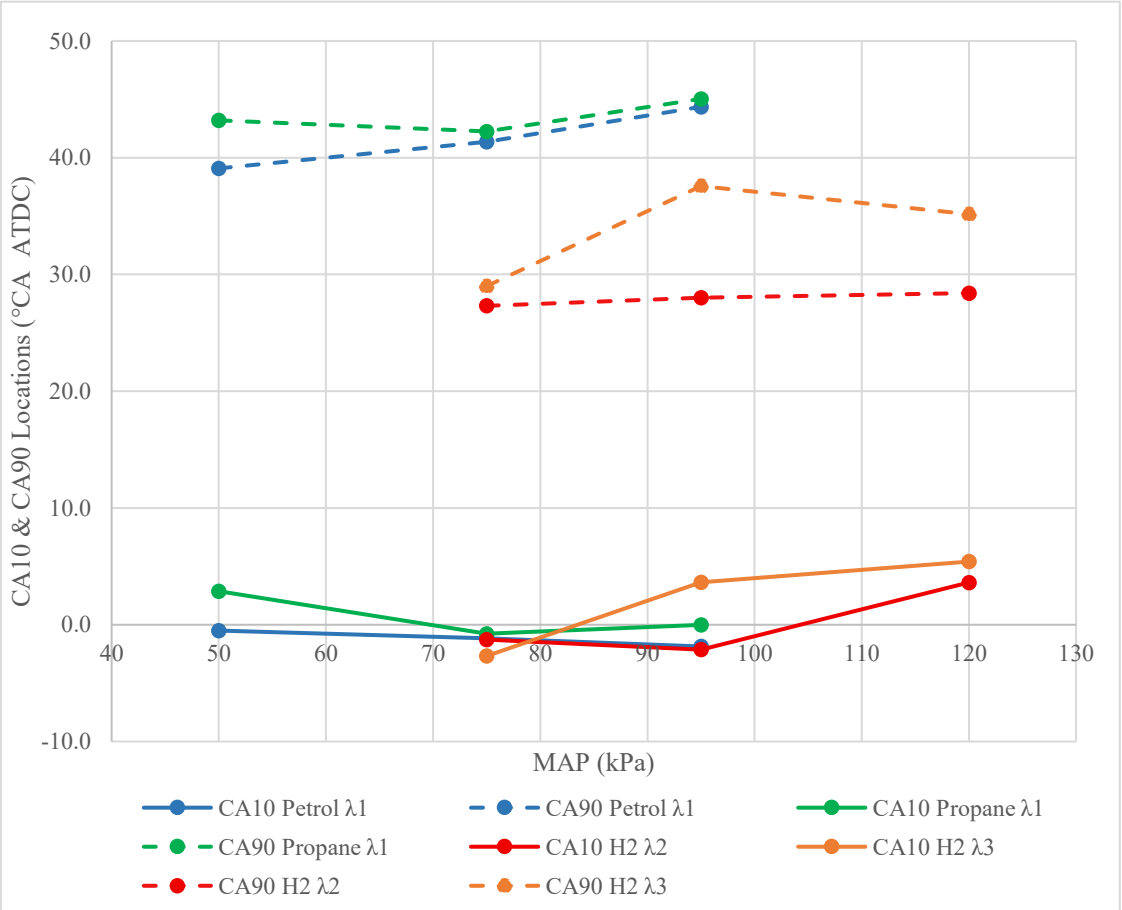

Figure 6-15: The variation of the CA10 & CA90 locations with MAP obtained using the Pipitone's approach presented in (3.16).

6.9 Fast Burn Duration

The variation in fast burn durations for all fuels with respect to MAP is illustrated in Figure 6-16. The most notable distinction is the longer burn duration exhibited by traditional fuels compared to that observed during H_2 testing. Additionally, the trends in the burn duration curves differ. While the burn duration of traditional fuels tends to

increase with MAP, H_2 testing shows a decrease in burn duration as MAP increases. It is important to note that even at lean λ3 mixtures, H_2 demonstrates a shorter burn duration than traditional fuels. This is an important point to observe, as it is widely accepted that, under leaner mixture conditions, the flame speed tends to decrease significantly, which is why earlier ignition advance is typically required. These results highlight the rapid flame speed characteristic that H_2 combustion possesses, a point emphasised by Al-Baghdadi [64].

Comparing these results to those reported by Negurescu et al. [69] in Figure 2-11, shorter burn durations of 21° CA at λ2 were reported, which align with those reported by Rrustemi [60] in Figure 2-13. This burn duration is slightly shorter to those depicted in Figure 6-16. For the λ3 mixture at wide open throttle conditions (100 kPa), Negurescu et al. [69] reported a burn duration of 34° CA, which is comparable to that depicted in Figure 6-16. For higher loads at λ2, Rrustemi et al. [69] reported a burn duration of approximately 29° CA which is slightly longer than that illustrated in Figure 6-16.

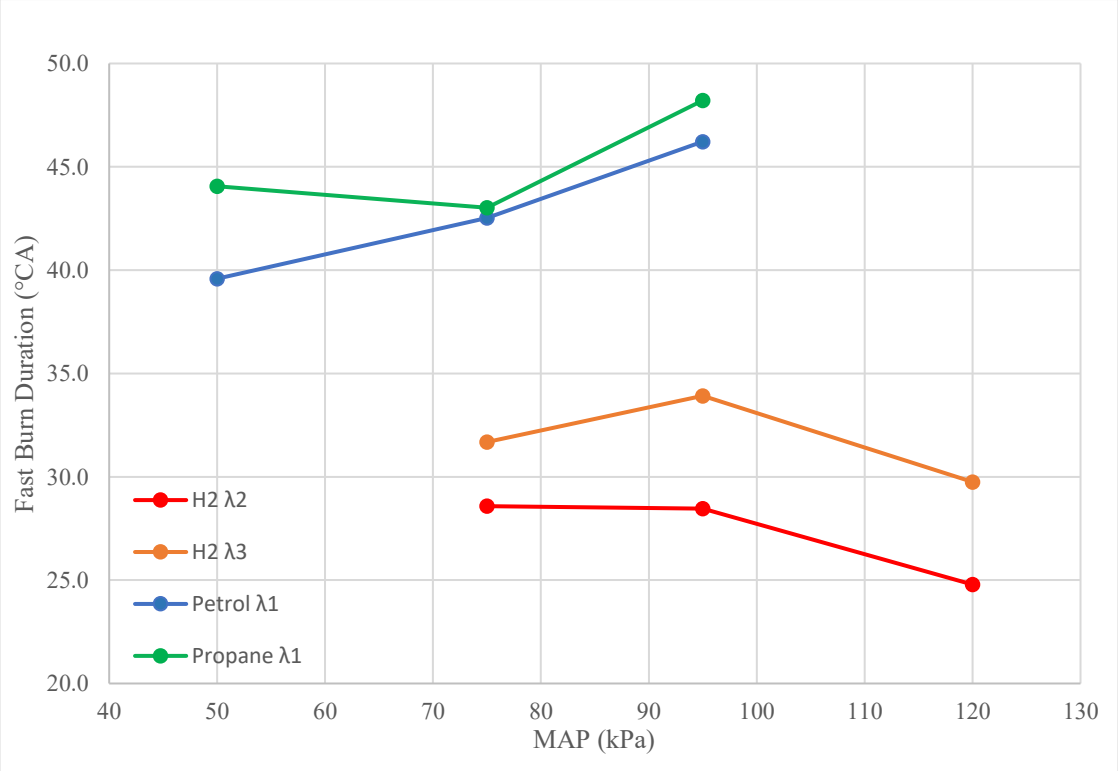

Figure 6-16: The variation of fast burn duration computed on values of CA10 and CA90 using the (3.16) approach.

6.10 Ignition Delay

Figure 6-17 depicts the variation of ignition delay with respect to MAP. As expected, H_2 λ3 mixtures exhibit a longer ignition delay compared to the richer λ2 mixture. The ignition delay for the H_2 λ2 mixture remains relatively constant across the range of MAP values tested. In contrast, for the leaner mixture, the ignition delay shows a slight increase with increasing MAP. On the contrary, during both propane and petrol testing, the ignition delay tends to decrease as MAP increases.

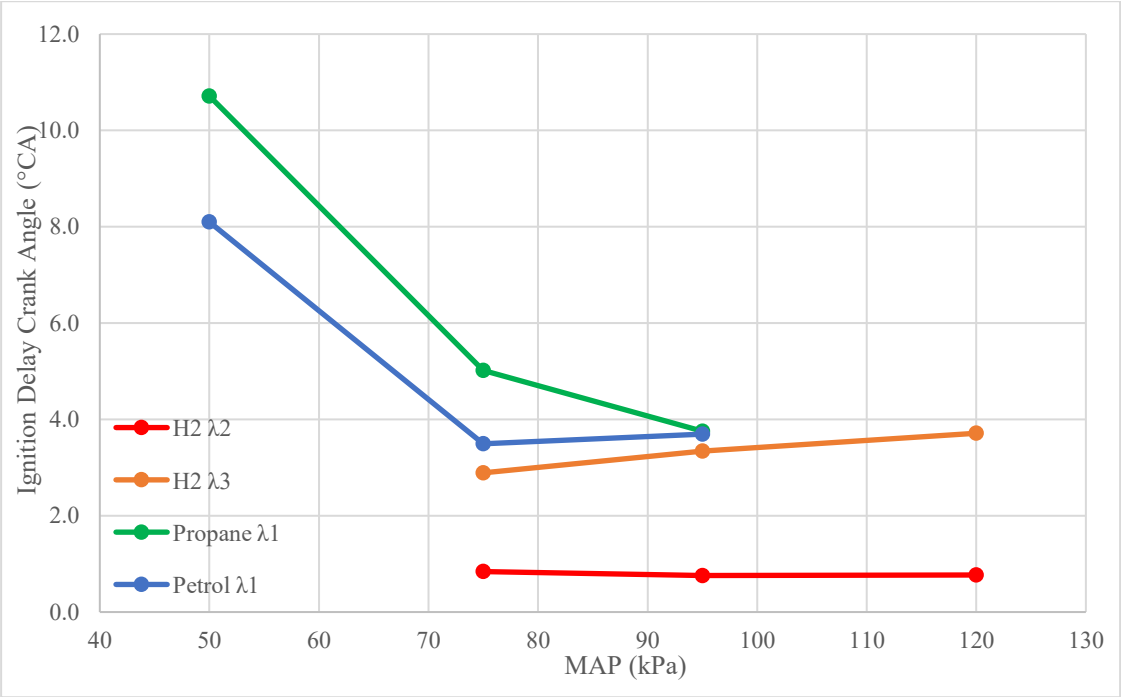

Figure 6-17: The variation of ignition delay with MAP.

Since petrol is injected in a liquid state, it would require time to vaporise. Despite this unavoidable time, it seems to have a lower ignition delay at lower MAP values compared to propane which is injected in a vapour form. Jet [100] comments on how ignition delay is observed to be attributed to multiple factors such as the physical injection timing, mixing delay and chemical reaction delay. The author [100] observed similar characteristics to those mentioned by Obert [101] on results from performing petrol testing where it is emphasised that with an increase in MAP the ignition delay is decreased. This might take place since higher intake manifold pressures have a higher gas density, which cause higher in-cylinder temperatures during compression shortening the ignition delay. As commented by Hires et al. [140] the ignition delay is mostly affected by the ignition timing where earlier timings cause higher ignition delays due to the low in-cylinder temperatures in the early compression phase.

6.11 Energy Losses

The energy losses were estimated through two approaches described in Section 3.2. The first approach, based on (3.8) is presented in Figure 6-18. The energy lost primarily represents the heat lost; however, it also includes contributions from friction, blow-by gases and unburnt fuel. The results of the second approach are presented in Figure 6-19 which were calculated through the (3.9) approach which makes use of Pipitone's net HRR presented in (3.5).

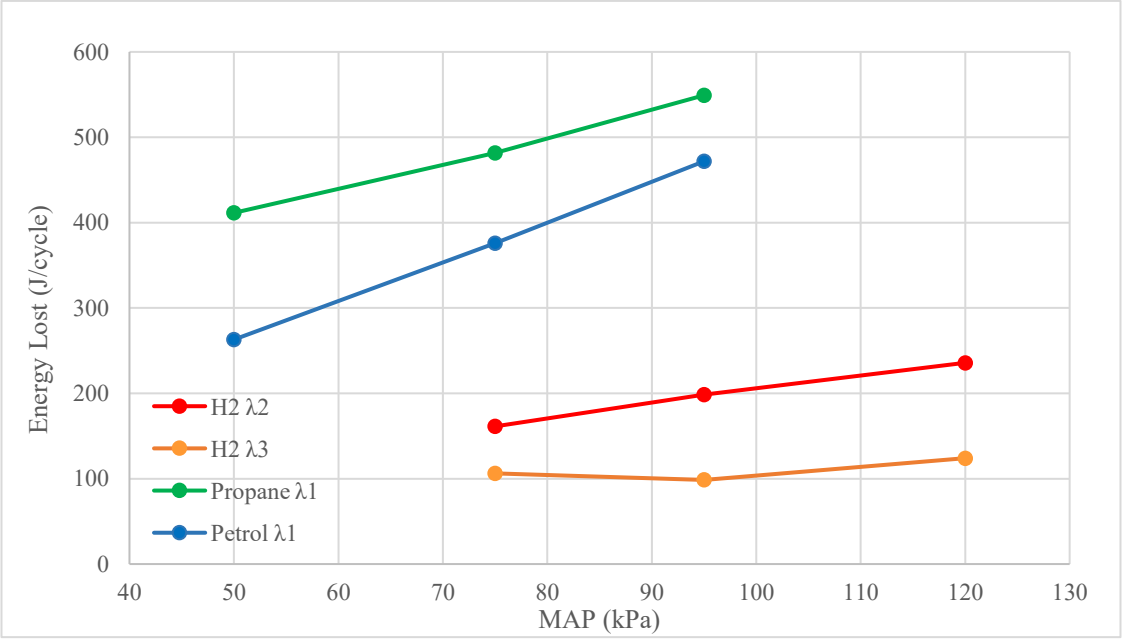

Figure 6-18: The variation of energy losses with MAP using the (3.8) approach.

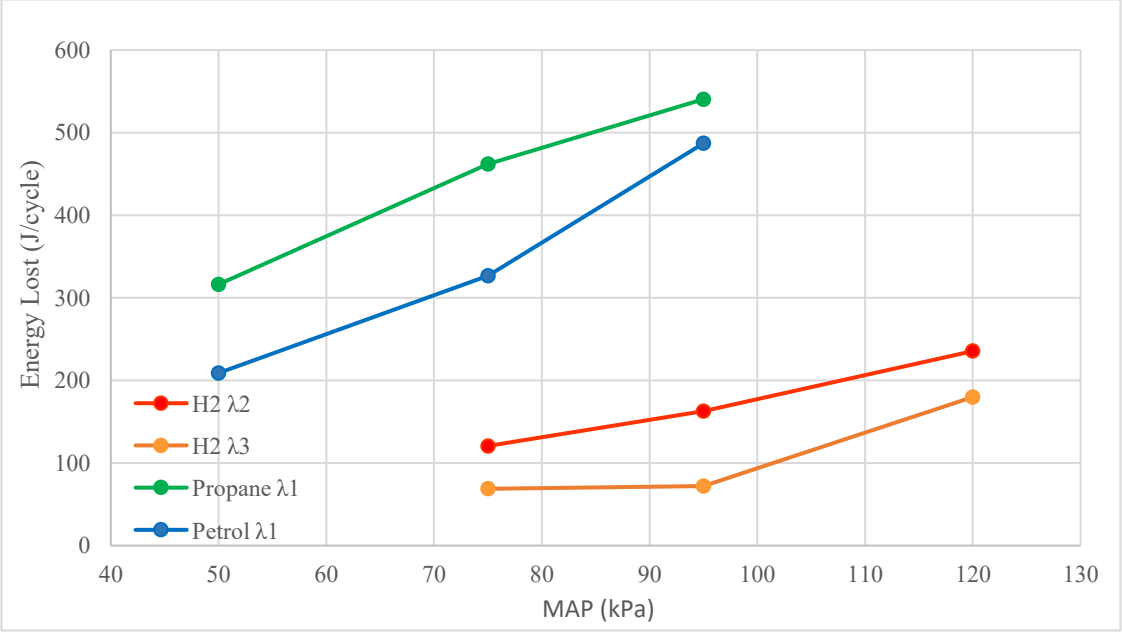

Figure 6-19: The variation of energy losses with MAP using the (3.9) approach.

As observed from Figure 6-18 and Figure 6-19 similarity in the obtained values and curve characteristics were noticed. It is important to appreciate that the two approaches used contain information which was obtained differently nevertheless the same conclusions were obtained. For all the fuels with the increase in MAP a higher heat loss was computed which directly correlates to the higher in-cylinder combustion temperatures achieved from the higher pressures. These conclusions are different to those reported by Demuynck et. al. [62] who through Figure 2-14 showed that heat flux reduced with the increase of the throttle position (i.e. increase in MAP). Subsequently, the authors [62] commented on how the heat flux of H_2 during lean mixtures seem to be equivalent to that reported during petrol testing. In contrast, as observed in Figure 6-18 and Figure 6-19 the heat losses of H_2 during both mixtures tend to be less than those of petrol. It is also important to mention that the heat losses during the lean H_2 λ3 mixture are less than those experienced during the richer H_2 λ2 mixture due to the decrease in combustion temperature during the leaner mixture.

6.12 Peak Blow-by Gases

Among the various terms considered in the energy loss analysis, blow-by gases are included. The peak blow-by gases shown in Figure 6-20 were calculated through the use of (3.6) discussed in Section 3.1.

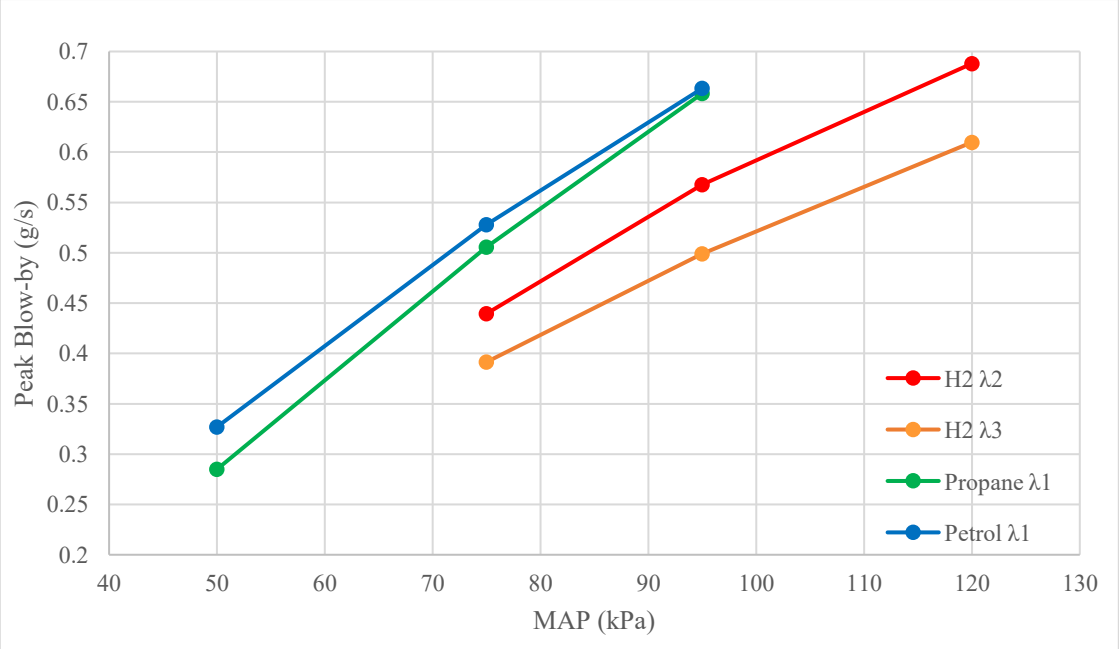

Figure 6-20: The variation of blow-by for different fuels with MAP.

As depicted in Figure 6-20, blow-by gases tend to increase with MAP for all fuels, as expected, due to the higher in-cylinder pressure. According to Figure 2-16, Rahmani et al. [74] reported a higher mass flow rate during petrol fuelled tests compared to H_2 tests. The authors commented that these tests were conducted at stoichiometric conditions with a DI fuel strategy. In contrast, the results shown in Figure 6-20 indicate that blow-by gases during petrol tests amounted to larger amounts than those calculated for H_2. This difference in blow-by between petrol and H_2 is primarily attributed to the lower pressures generated during H_2 lean mixtures, resulting in lower amounts of blow-by gases. A direct comparison can be made with the blow-by gases during stoichiometric petrol testing where Rahmani et al. [74] reported a mass flow rate of 1.5 g/s which is approximately twice than that depicted in Figure 6-20. One possible explanation for this difference might be the high CR of 11.5 utilised in the setup of Rahmani et al. [74] compared to the CR of 5.36 in this research.

6.13 Maximum Mass Fraction Burned

As previously mentioned in Section 6.10, the two MFB approaches described tend to yield different maximum MFB values. The maximum MFB obtained from the (3.16) approach was calculated and presented in Figure 6-21.

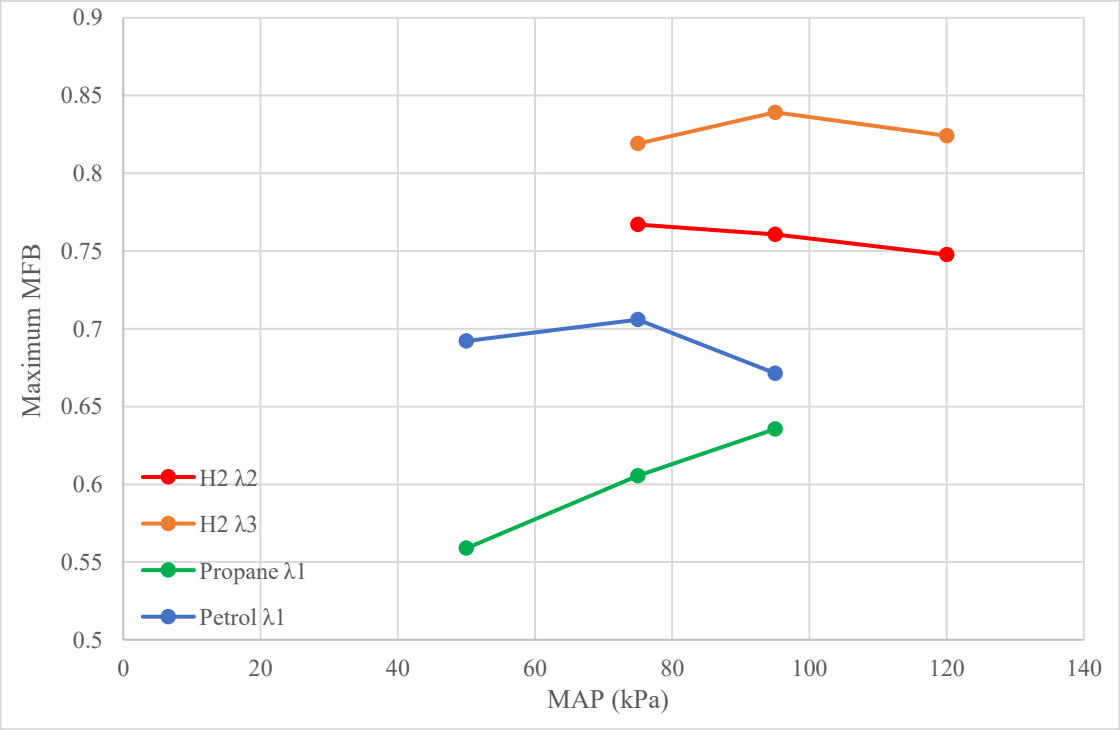

Figure 6-21: The variation of the maximum MFB value whilst using the (3.16) approach.

A portion of the values presented in Figure 6-21 can be attributed to the amount of fuel that remained unburned during the cycle. It can be observed that the highest maximum MFB values were obtained during H_2 λ3 testing. These results directly correlate with the lowest energy losses reported during the same tests. This implies that when energy losses are minimised (due to lower temperatures at λ3), more energy is manifested in the combustion process and further promotes complete fuel burning. The high MFB values obtained are primarily due to the extreme lean operating mixtures. When an abundant amount of air is present in the combustion chamber, the fuel will effortlessly react with it and combust. Conversely, under stoichiometric conditions, the fuel may face greater difficulty reacting with air which results in increased unburned fuel.

6.14 Energy Lost Ratio

To provide context and enable better comparison, the calculated energy lost values were normalised by dividing the values by the total energy input (i.e. the multiplication of the mass of fuel and LHV) as depicted in Figure 6-22. Due to the similarity in the energy loss values reported in Figure 6-18 and Figure 6-19, this ratio was calculated on the energy loss values obtained through the (3.9) approach.

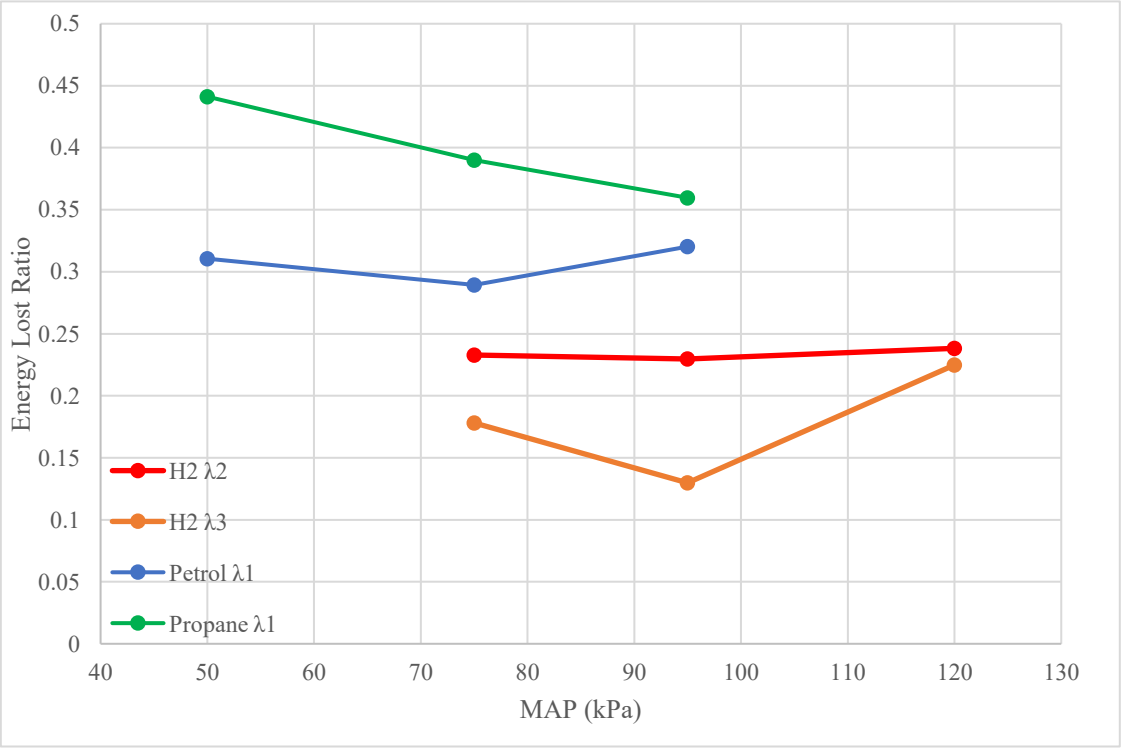

Figure 6-22: The variation of heat lost as a ratio to the inputted energy with MAP.

Figure 6-22 reveals conclusions like those presented in Section 6.11 where H_2, specifically the λ3 mixture, appears to have the lowest energy loss relative to the input energy. On the other hand, propane, specifically at low loads exhibits the highest energy loss. This might be attributed to the low manifold air pressure which likely causes incomplete combustion of the propane resulting in most of the injected fuel being classified as energy loss. This conclusion also agrees with the BTE findings depicted in Figure 6-4 where the highest values are obtained during the H_2 λ3 mixture operation.

6.15 Closing Remarks

In this chapter various combustion characteristics were analysed using the most appropriate methods identified in Chapter 3 according to the test points identified in Section 4.3 for H_2, propane and petrol. Through this combustion characterisation, distinctive combustion properties of H_2 were identified and systematically compared with existing literature. Amongst the multiple combustion characteristics analysed, H_2 seemed to have the shortest burn durations, ignition delays and specifically at a MAP of 95kPa both λ2 and λ3 mixtures recorded the highest BTEs when compared to the other fuels. Despite having higher calorific values, H_2 for both mixtures did not achieve the highest torque, mainly due to differences in the air-fuel ratio (AFR) and its low density, which also affects the engine's volumetric efficiency. This analysis provides valuable insights into key parameters required to optimise H_2 combustion performance. Consequently, it facilitates a smoother transition for integrating H_2 combustion into DFE systems.

Chapter 7. Dual-Fuel Results and Discussion

In this chapter all the results from the experimental investigation described in Chapter 5 are presented and discussed. All tests presented were carried out using propane and diesel fuels with either liquid propane injection or LN_2 injection. For liquid propane both cold (36 °C) and hot (74 °C) intake air tests were carried out; for LN_2 only hot air intake testing was performed – if not heated the resulting decreased intake air temperature would be below zero, causing icing which can lead to problems. Although preliminary calculations in Chapter 5 assumed 3000 RPM, solenoid valve delay limited frequency to 2.5 Hz, so tests used 2000 RPM instead. All the tests carried out were at a 150 kPa boosted conditions and DOI of the pilot fuel (diesel) set to a constant injection minimum of 0.3 ms.

7.1 LN_2 Steady State Testing

Steady state testing was performed at an air temperature of approximately 74 °C and the SOI was gradually varied to a maximum value of 22° CA BTDC before initiating LN_2 injection as shown in Figure 7-1. The SR was set to 60% and the λ=2.5.

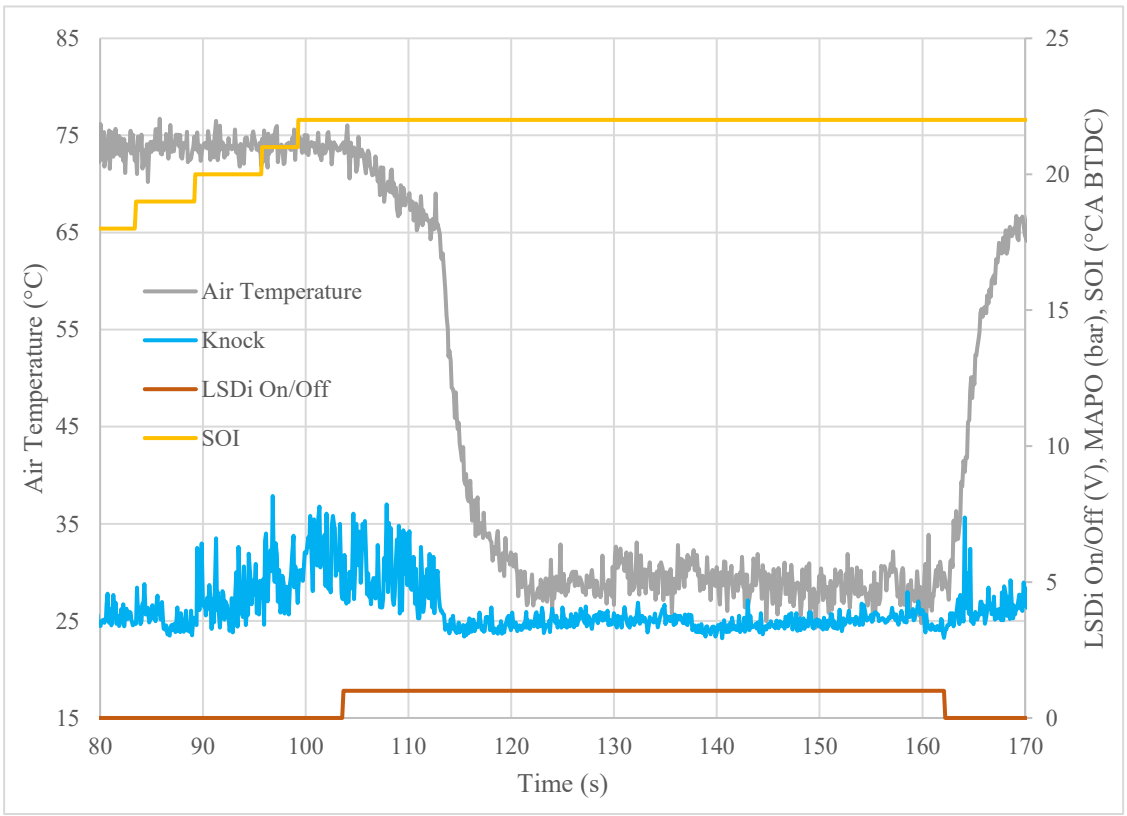

Figure 7-1: Steady state LN_2 injection.

Upon initiation of LN_2 injection the intake air temperature experienced a significant temperature drop of approximately 45 °C, maintaining this reduced temperature for about 40 seconds. This thermal reduction directly affected knock, corresponding to a decrease in MAPO, which was initially measured at around 8 bar and subsequently decreased drastically to typical operating levels of approximately 3 bar. It is important to note that a MAPO of 3 bar was recorded prior to LN_2 injection when the SOI timing was set at 18° CA BTDC. Under the cooling effect of LN_2, an equivalent MAPO of 3 bar was observed even with the SOI retarded to 22° CA BTDC. Termination of LN_2 injection (indicated by the LSDi On/Off control signal transitioning from 1 V to 0 V), the intake air temperature rapidly increased, ultimately returning to its initial value of 74 °C. Consequently, the MAPO increased in amplitude with the temperature rise, confirming the strong temperature dependence of MAPO.

7.2 Liquid Propane Steady State Testing

Steady state propane tests were performed at both cold and hot intake air temperatures since the drop in temperature caused by the phase change of liquid propane is less than that caused by LN_2. Moreover, cold intake air temperatures of around 33 °C will not allow any formation of ice inside the intake manifold. The hot intake air tests were performed at temperatures of around 70 °C. To validate the effect of liquid propane injection, vapour propane tests were performed for comparison reasons. All the tests were performed with a 60% SR at a λ=2.5 and with a 70% at a λ=1.7. Since different SRs were used during experimentation, different SOI values were set accordingly during cold and hot intake air temperatures, depending on the limits of MAPO observed during testing. Additionally, different rise in temperatures, (which are equivalent to the drop in temperatures) were noticed during the liquid propane injection as highlighted in Figure 7-3 and Figure 7-2. The increase in the measured air temperature during the 60% SR test was approximately 4 °C. As expected, the intake air temperature rise observed during the 70% SR test was higher reaching approximately 7 °C. This observed increase in temperature is of a similar magnitude to the temperature reduction induced by the liquid propane injection. Notably, the measured temperature rise during the 70% SR test closely aligned with the calculated temperature drop of 7.8 °C attributable to liquid propane injection, as detailed in Section 5.2.3. This close agreement validates the accuracy of the predicted temperature change under the specified operating conditions.

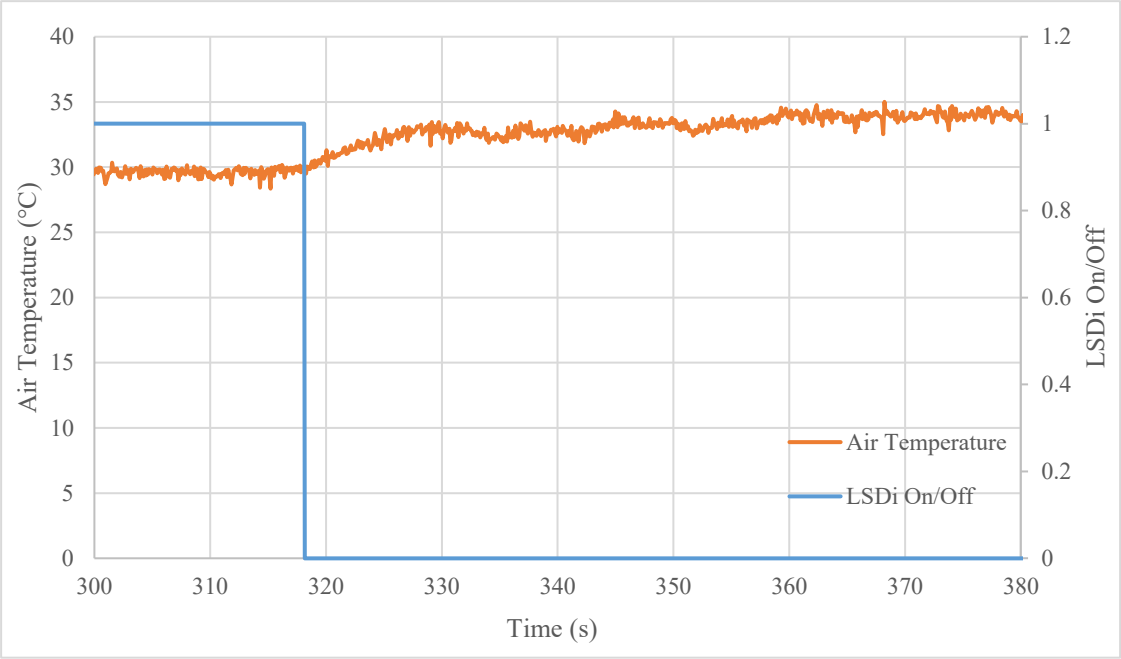

Figure 7-3: Increase in temperature observed after stopping of liquid propane injection with a 60% SR and 2.5λ.

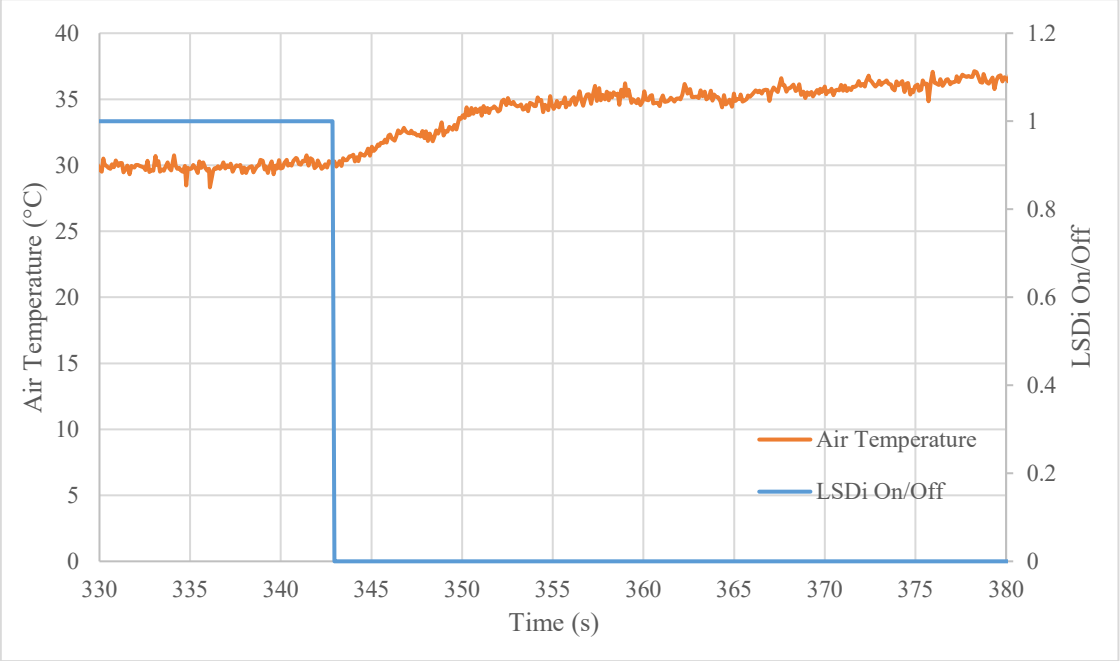

Figure 7-2: Increase in temperature observed after stopping of liquid propane injection with a 70% SR and 1.7λ.

The SOI variation in each experiment together with the MAPO for hot and cold intake temperatures are depicted in Table 7-1 and Table 7-2 respectively. All the MAPO values presented have a COV of 0.3%.

Table 7-1: MAPO during cold intake temperatures for liquid and vapour propane injection at 60 %SR and 70% SR.

	Cold									
	60 % SR at a λ=2.5						70 % SR at a λ=1.7			
	Vapour			LSDi			Vapour		LSDi	
SOI (°CA BTDC)	25	30	35	25	30	35	18	25	18	25
MAPO (bar)	4.8	5.5	6.0	4.1	4.3	4.5	4.1	7.2	3.8	4.3

Table 7-2: MAPO during hot intake temperatures for liquid and vapour propane injection at 60 %SR and 70% SR.

	Hot					
	60% SR at a λ=2.5				70% SR at a λ=1.7	
	Vapour		LSDi		Vapour	LSDi
SOI (°CA BTDC)	18	25	18	25	18	18
MAPO (bar)	4.1	6.2	3.8	4.3	7.2	4.2

The MAPO reported in Table 7-1 and Table 7-2 indicate that, under both cold and hot air temperature conditions the knock intensity levels decreased when LSDi was performed. As documented by Żółtowski [77] and Nwafor [75] the knock intensity levels in DFE is strongly dependent on the SR ratio. The highest MAPO recorded was of 7.2 bar observed with vapourised propane during cold intake temperatures at a SOI

timing of 25° CA BTDC. Equivalent MAPO values were also observed during vapour phase propane testing at hot intake temperatures with a SOI timing of 18° CA BTDC. It is important to note that SOI timings greater than 18° CA BTDC were not achievable at a 70% SR under hot intake conditions during both vapour and liquid propane testing. This was not feasible due to excessively high MAPO levels which pose a significant risk of engine damage. On the other hand, as expected for both fuel injection strategies, at a 60% SR, SOI timings up to 25° CA BTDC were achievable corresponding to lower measured MAPO intensities. Moreover, at the same 60% SR, SOI timings as advanced as 35° CA BTDC were possible during cold intake temperatures, illustrating the strong dependence of MAPO on intake air temperature as emphasised by Lakshmanan et al. [86]. This effect is further evidenced by MAPO values of approximately 3 bar recorded during LN_2 injection which were not attained with liquid propane injection, even at a SOI timing of 25° CA BTDC under cold intake conditions. It is important to emphasise that the intake air temperature reduction achieved by LN_2 injection is approximately six times greater than that produced by liquid propane injection

7.3 Effect of Knock on Torque

During steady state testing all input variables were held constant to maintain stable output parameters such as torque. However, it was observed that torque output varied with MAPO during the tests. This phenomenon is illustrated in Figure 7-4 and Figure 7-5, showing results from vapour and liquid propane injection during separate tests.

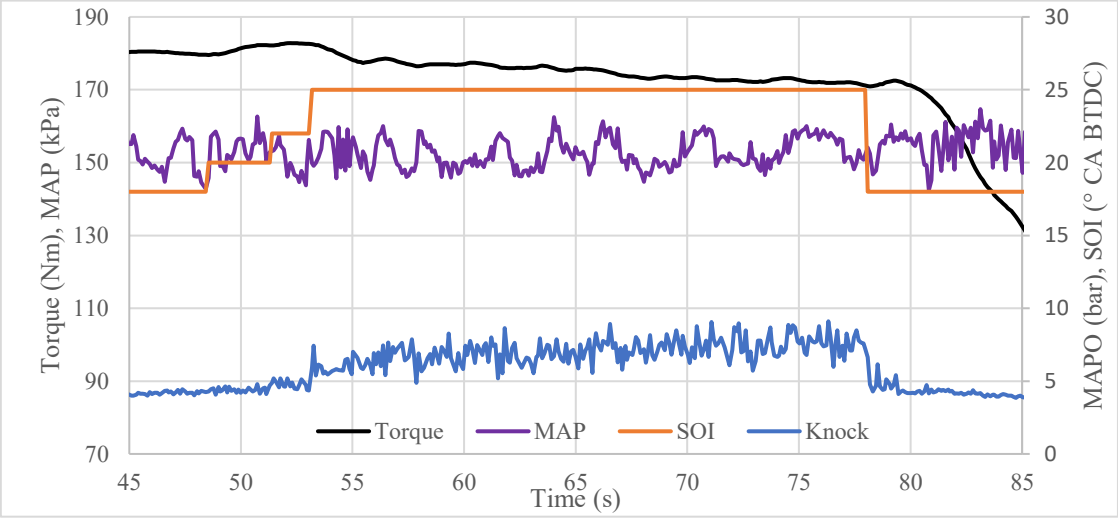

Figure 7-4: The variation of torque with time during steady state testing with vapour propane at cold intake air temperatures.

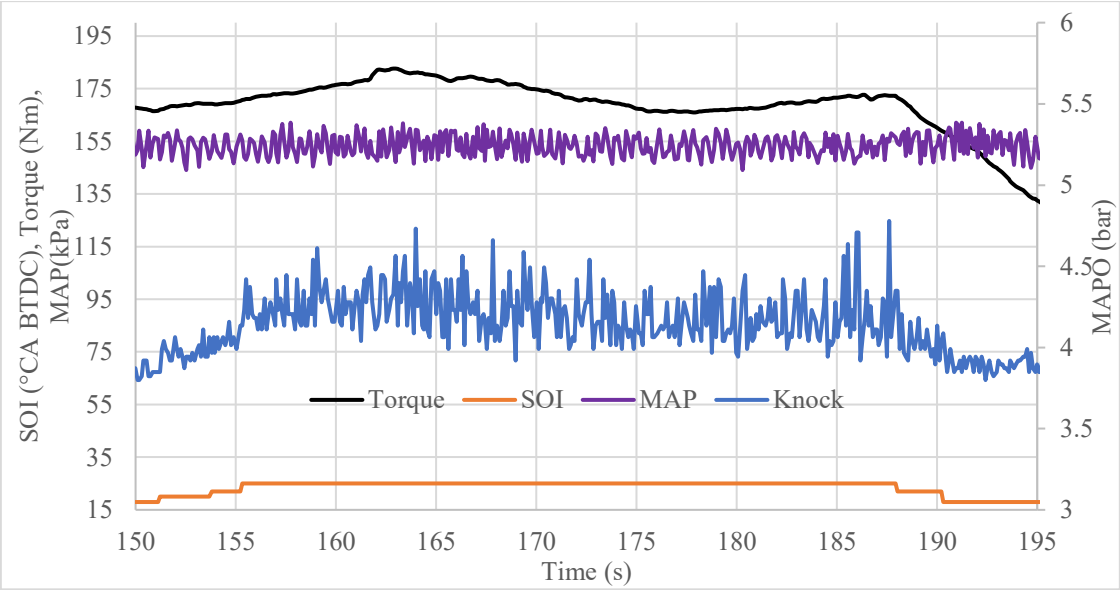

Figure 7-5: The variation of torque with time during steady state testing with liquid propane injection at cold intake air temperatures.

As outlined by Syrimis et al. [76] the random occurrence of knock and the linear variation of heat flux with knock intensity result in energy loss which is reflected in the torque output. This finding directly correlates to the "scouring" of the quenching boundary layer that Riccardo [13], mentioned which increases the energy loss. The MAPO profiles presented in Figure 7-4 and Figure 7-5 clearly illustrate an increase in knock magnitude during vapour-phase testing. Consequently, as previously discussed, a reduced MAPO is observed during liquid propane injection, which is attributed to the corresponding reduction in intake air temperature.

7.4 Closing Remarks

The results obtained from experimental investigations involving both liquid propane injection and vapour-phase propane testing, particularly through the analysis of the MAPO, indicate that liquid propane injection effectively mitigates knocking. This outcome is consistent with expectations due to the associated reduction in intake air temperature, a phenomenon well-documented in the literature. This conclusion was further validated through experiments involving LN_2 injection, where a temperature drop of approximately 45 °C significantly reduced the MAPO values, even at advanced SOI timings. These findings are critical for enhancing the performance and knock resistance of current DFE configurations, thereby facilitating a more seamless and effective integration of H_2 fuel into DFE systems.

Chapter 8. Summary and Conclusions

As technologies advance, renewable energy is becoming increasingly accessible. This progress and abundance in renewable energy creates a growing need for the development of advanced energy storage technologies to store energy for later use, thereby reducing dependency on the conventional technologies powered by fossil fuels. Among various energy storage options, the generation and storage of H_2 fuel represent a promising solution. H_2 has diverse applications, including use as a fuel in internal combustion engines. To gradually introduce H_2 as an alternative sustainable fuel, a smooth transition through application in DFE technology is essential. This transition requires a detailed analysis of H_2 combustion to identify differences from traditional fuels and to determine key operational parameters such as ignition timing for optimised combustion. Similar to how hybrid technologies played a crucial role in the advancement of electric vehicles, H_2 DFEs can serve as a vital bridging technology, supporting cleaner and more efficient transportation solutions for future generations. Nonetheless, during this transition period, fully utilising existing dual-fuel technology is both practical and beneficial.

To further advance the understanding of H_2 combustion, a comprehensive experimental investigation was conducted to determine its combustion characteristics. For comparison purposes, identical experiments were performed using traditional fuels. A key aspect of this investigation was the development of an improved mass airflow measurement system for the engine, which allowed the determination of the AFR during lean H_2 operation. This measurement system employed choked flow theory through the design and implementation of a critical flow orifice sized specifically to measure the engine's intake airflow. This technique was selected because the measurement is not affected by the pulsating airflow conditions intrinsically found in an engine. This improved measurement capability is essential for a more accurate combustion analysis, as precise determination of the fuel mixture is fundamental to studies focusing on fuel utilisability. Notable differences observed during H_2 operation included significantly shorter ignition delay and combustion duration compared to traditional fuels. The ignition delay and combustion duration of H_2 $\lambda 2$ was concluded to be 1 and 29° CA respectively, while for stoichiometric petrol operation were 4 and 46° CA. Since the main objective of this experimental investigation involved the exploration of lean mixtures, lower power output was noted. It was concluded that despite the reduced power, substantially a higher

brake thermal efficiency of 23% was achieved with H_2 λ3 mixture compared to the 21% achieved with petrol and propane testing at wide open throttle. This high efficiency obtained during H_2 testing further underscores its efficient combustion capabilities.

A major focus of the research was the enhancement of DFE performance through the concurrent exploration of LSDi technology. This technology involves the injection of fuel in its liquid phase to utilise the latent heat of vaporisation subsequently prompting intake air cooling. A cryogenic system, consisting of both storage and injection components, was assembled from commercially available parts with the original intent of using LNG as the liquid fuel. However, due to safety and handling concerns with LNG, experiments were redirected towards other cryogenic fluids. Testing with LN_2 successfully demonstrated an intake air temperature reduction of approximately 45 °C. Subsequent experiments made use of liquid propane as a substitute fuel, to investigate the effects at different substitution ratios. Liquid propane injection achieved temperature reductions of 7 °C and 4 °C for fuel SRs of 70% and 60% respectively, confirming the cooling effectiveness of liquid fuel vaporisation. The LSDi system was further validated by calculating the MAPO through comparison of data obtained from liquid phase injection and vapour phase testing. This comparison provided strong evidence of the effectiveness of the LSDi technology across different SRs and intake air temperatures. Therefore, it was concluded that this injection system significantly reduced the intake air temperature. As a result, this approach addressed the common operational limitation of engine knock experienced in gas-fuelled engines, thereby improving combustion stability and efficiency.

By combing the extensive research on the combustion characteristics of H_2 with liquid fuel injection strategies, this study presents an integrated approach for cleaner and more efficient fuel utilisation to produce mechanical work. This approach not only advances the understanding of these distinct combustion technologies but also proposes a viable pathway for optimising existing dual-fuel combustion systems. This contributes valuable knowledge to the ongoing development of H_2-powered internal combustion engines. The outcomes of this work have significant implications for accelerating the transition towards sustainable fuel use in the transportation section, as well in other industrial areas such as the power generation. The combined effect of these two investigations was intended to align the two separate technologies, thereby taking

existing research one step forward and ensuring that future generations benefit from a healthier and safer environment.

8.1 Limitations of Work

Liquid state injection limitations: One limitation of the built injection system in reducing the intake air temperature for the dual-fuel setup is the procured cryogenic solenoid valve. Testing revealed that it cannot operate at frequencies higher than 3.4 Hz. Consequently, testing at higher substitutional ratios cannot be reliably performed with this type of solenoid valve. Additionally, testing at higher engine speeds are also not feasible for the same reason. To conduct these tests, another cryogenic solenoid valve must be procured, which will likely be challenging due to the demanding cryogenic requirements involved.

H_2 combustion characterisation limitations: For the H_2 experiments, petrol and propane tests at 120 kPa MAP could not be conducted due to the risk of engine damage, preventing direct comparison with H_2 results. Similarly, stoichiometric H_2 tests could not be performed due to backfiring from the port fuel injection strategy. The available engine has a low compression ratio which did not enable high BTE efficiencies to be obtained during experiments. It would have been beneficial if a new engine with a higher compression ratio was procured.

8.2 Suggestions for Future Work

The procurement of an electrolyser to generate H_2 on-site would be ideal for performing further investigations with H_2. This apparatus would reduce dependency on compressed H_2 gas bottles and the associated delays experienced during this study. The electrolyser is necessary because the next step involves integrating H_2 into the dual-fuel engine setup, which is a 2-litre engine operating optimally at 2000 RPM. Consequently, the dual-fuel engine will consume approximately six times more H_2 than the single-cylinder J.A.P. 6 engine. Moreover, as deduced by Fenech [90], while carrying tests with H_2 on the J.A.P. 6 engine, a 200 bar, 8 Nm^3 tank would last approximately 30 minutes at an engine speed of 1500 RPM and a fuel line pressure of 3 bar. This operational time would reduce to about 5 minutes if the same H_2 tank was used for the dual-fuel H_2 experiments.

Chapter 9. Bibliography

[1] International Energy Agency, “Global EV Outlook 2024,” 2024. [Online]. Available: https://iea.blob.core.windows.net/assets/a9e3544b-0b12-4e15-b407-65f5c8ce1b5f/GlobalEVOutlook2024.pdf. [Accessed 30 October 2024].

[2] A. Isenstadt and P. Slowik, *Hybrid vehicle technology developments and opportunities in the 2025-2035 time frame,* The International Council on Clean Transportation , 2025.

[3] A. Kecebas and M. Kayfeci, “Hydrogen properties,” *Solar Hydrogen Production,* pp. 3-29, 2019.

[4] M. Segal, “ESG today,” 5 September 2024. [Online]. Available: https://www.esgtoday.com/bmw-to-launch-hydrogen-powered-fuel-cell-electric-vehicle-in-2028-in-partnership-with-toyota/. [Accessed 30 October 2024].

[5] A. Kovac, M. Paranos and D. Marcius, “Hydrogen in energy transition: A review,” *International Journal of Hydrogen Energy,* vol. 46, no. 16, pp. 10016-10035, 2021.

[6] World Meteorological Organization, “Global temperature is likely to exceed 1.5°C above pre-industrial level temporarily in next 5 years.,” 5 June 2024. [Online]. Available: https://wmo.int/news/media-centre/global-temperature-likely-exceed-15degc-above-pre-industrial-level-temporarily-next-5-years. [Accessed 2 November 2024].

[7] United States Envirionmental Protection Agency, “Greenhouse Gas Emissions Standards for Heavy-Duty Vehicles-Phase 3,” *Federal Register,* vol. 88, no. 81, pp. 26198-26261, 22 April 2024.

[8] G. A. Karim, Dual-Fuel Diesel Engines, Boca Raton, FL, USA: CRC Press, 2015.

[9] C. Mansour, A. Bounif, A. Aris and F. Gaillard, “Gas-Diesel (dual-fuel) modeling in diesel engine envirionment,” *Fuel Processing Technology,* vol. 75, pp. 81-93, 2002.

[10] Enemalta, “Delimara Power Station,” 30 August 2017. [Online]. Available: https://www.enemalta.com.mt/2017/08/30/last-heavy-fuel-oil/. [Accessed 13 November 2024].

[11] Wärtsilä, “Successful operating performance results in key Malta power plant renewing Wärtsilä service agreement for second time,” Wärtsilä Corporation, 8 June 2021. [Online]. Available: https://www.wartsila.com/media/news/08-06-2021-successful-operating-performance-results-in-key-malta-power-plant-renewing-wartsila-service-agreement-for-second-time-2928522.

[12] A. Arefin, N. Nabi, A. Washim, M. Towhidul Islam and W. Chowdhury, “A review on liquified natural gas as fuels for dual fuel engines: Opportunities, challenges and responses,” *Energies,* vol. 13, no. 22, 2020.

[13] Sir Harry R. Riccardo, LL.D., F.R.S, “The High-Speed Internal-Combustion Engine,” Blackie & Son Limited, London and Glasgow, 1923.

[14] M. Djermouni and A. Quadha, “Comparative assessment of LNG and LPG engines,” *Energy Procedia,* vol. 139, pp. 254-259, 2017.

[15] S. Kumar, H. T. Kwon, K. H. Choi, W. Lim, J. Hyun Cho, K. Tak and I. Moon, "LNG: An eco-friendly cryogenic fuel for sustainable development," *Applied Energy,* vol. 88, no. 12, pp. 4264-4273, 2011.

[16] R. Verbeek, G. Kadijk, P. van Mensch, C. Wulffers, B. van den Beemt and F. Fraga, "Envirionmental and Economic aspects of using LNG as a fuel for shippping in The Netherlands," TNO, Delft, 2011.

[17] G. Erbach and L. Jensen, "EU hydrogen policy - Hydrogen as an energy carrier for a climate-neutral economy," 2021 April 12. [Online]. Available: https://www.europarl.europa.eu/thinktank/en/document/EPRS_BRI(2021)689332. [Accessed 2 September 2025].

[18] B. Shively, "Hydrogen Gas Injection into the Natural Gas Grid Has Begun in the U.K.," Enerdynamics The Energy Education Experts, [Online]. Available: https://www.enerdynamics.com/Energy-Currents_Blog/Hydrogen-Gas-Injection-into-the-Natural-Gas-Grid-Has-Begun-in-the-UK.aspx. [Accessed 2025 September 5].

[19] M. G. Galal, M. M. Abdel and M. A. El Kady, "A comparative study between diesel and dual-fuel engines," *Combustion Science and Technology,* vol. 174, pp. 241-256, 2002.

[20] T. Park, *Dual Fuel Conversion of a Direct-Injection Diesel Engine Dissertation,* Morgantown, US: West Virginia University, 1999.

[21] Z. Jia, "Dual-Fuel Combustion in a Heavy-Duty Engine Dissertation," Chalmers University of Technology, Gothenburg, 2018.

[22] K. Bhavani and S. Murugesan, “Diesel to Dual Fuel Conversion Process Development,” *International Journal of Engineering & Technology,* vol. 7, no. 3.6, p. 306, 2018.

[23] A. G. Karim, *The Dual Fuel Engine of the Compression Ignition Type - Prospects, Problems and Solutions - A Review,* SAE International Paper 831073, 1983.

[24] M. J. B. Kabeyi and O. A. Olanrewaju, “Conversion from Diesel to Dual Fuel Power Generation and Implications on the Transition,” in *Proceedings of the 7th North American International Conference on Industrial Engineering and Operations Management*, Orlando, FL, USA, 2022.

[25] S. Kundu, J. Zanganeh and B. Moghtaderi, “A review on understanding explosions from methane-air mixture,” *Journal of Loss Prevention in the Process Industries,* vol. 40, pp. 507-523, 2016.

[26] R. T. Jones and R. W. Bolz, CRC Handbook of Tables for Applied Engineering Science, Cleveland, OH, USA: CRC Press, 1970.

[27] S. Kumar, H.-T. Kwon, K.-H. Choi, W. Lim, J. H. Cho, K. Tak and I. Moon, “LNG: An eco-friendly cryogenic fuel for sustainable development,” *Applied Energy,* vol. 88, no. 11, pp. 4141-4152, 2011.

[28] C. S. Weaver, *Natural Gas Vehicles - A review of the State of the Art,* SAE Technical Paper 892133, 1989.

[29] U. T. Institute, “CNG vs. LPG vs. LNG Fuel: Understanding the Differences,” 30 January 2020. [Online]. Available: https://www.uti.edu/blog/diesel/cng-lpg-lng-fuel. [Accessed 24 November 2024].

[30] T. Abdallah, “Sustainable elements of bus networks,” in *Sustainable Mass Transit: Challenges and Opportunities in Urban Public Transportation*, Amsterdam, Elsevier, 2023, pp. 187-216.

[31] G. A. Chamberlain, “Management of Large LNG Hazards,” in *23 rd World Gas Conference*, Amsterdam, 2006.

[32] W. H. Sutton, “Liquid Natural Gas as a Transportation Fuel in the Heavy Trucking Industry,” U.S. Department of Energy office, Washington, DC, 1997.

[33] W. L. Litzke and J. Wegrzyn, *Natural Gas as a Future Fuel for Heavy-Duty Vehicles,* SAE Technical Paper 2001-01-2067, 2001.

[34] Unitrove, “Compressed Natural Gas (CNG),” [Online]. Available: https://www.unitrove.com/engineering/gas-technology/compressed-natural-gas. [Accessed 2 December 2024].

[35] B. Chehroudi, “Use of Natural Gas in Internal Combustion Engines,” in *International Non-renewable Energy Sources Congress*, Tehran, Iran, 1993.

[36] ASTForgeTech, “Compressed Natural Gas CNG Storage Options,” Advanced Structural Technologies, [Online]. Available: https://astforgetech.com/compressed-natural-gas-cng-storage-options-ultimate-guide/. [Accessed 10 Decmber 2024].

[37] C. Industries, “HLNG: Horizontal LNG Storage Tanks - Technical Bulletin,” [Online]. Available: https://files.chartindustries.com/HLNGUS.pdf. [Accessed 13 December 2024].

[38] M. A. DeLuchi, R. A. Johnston and D. Sperling, *Methanol vs. Natural Gas Vehicles: A Comparison of Resource Supply, Performance, Emissions, Fuel Storage, Safety, Costs, and Transitions.,* SAE Technical Paper 881656, 1988.

[39] M. B. J. Kabeyi and O. A. Olanrewaju, "Cogeneration potential of an operating diesel engine power plant," *Energy Reports,* vol. 8, no. 16, pp. 744-754, 2022.

[40] T. Bogdan, "High Pressure Direct Injection of Natural Gas and Hydrogen Fuel in a Diesel Engine Dissertation," The University of British Columbia, Vancouver, 2001.

[41] G. A. Karim, "A Review Of Combustion Processes In The Dual Fuel Engine - The Gas Diesel Engine," *Progress in Energy and Combustion Science,* vol. 6, no. 3, pp. 277-285, 1980.

[42] N. Alhstrom, *Technical Specifications for Wartsila Gas Conversion Portfolio,* Finland: Vaasa University of Applied Sciences, 2021.

[43] Z. Wołczyński and M. Żak, "SI engine fuel mixture type indicator and an assessment of its suitability of an economic driving style," *Combustion Engines,* vol. 187, no. 4, pp. 69-76, 2021.

[44] F. Duronio, A. De Vita, A. Montanaro and C. Villante, "Gasoline direct injection engines - A review of latest technologies and trends.," *Fuel,* vol. 265, 2020.

[45] M. S. Mansour, A. M. Elbaz and M. F. Zayed, "Flame Kernel Generation and Propogation in Turbulent Partially Premixed Hydrocarbon Jet," *Combustion Science and Technology,* vol. 186, no. 4-5, pp. 698-711, 2014.

[46] Y. Wang, J. Tian, Y. Xiong, L. Wang, S. Ji and Y. Cheng, “Optimisation Study on Fuel Injection Characteristics of Gasoline Direct Injection (GDI) Engine Fuel System,” *Fuel,* vol. 381, 2025.

[47] A. N. Emmanuel, “Energy Efficiency Via Engine Improvements: A review of Dual Fuel Engine Development,” in *Shipping in changing Climates Conference*, Glasgow, 2015.

[48] T. L. Brown, H. E. LeMay, B. E. Bursten, C. J. Murphy, P. M. Woodward and M. E. Stoltzfus, Chemistry The Central Science, United States of America: Pearson Education, 2012.

[49] J. B. Heywood, Internal Combustion Engine Fundamentals, Cambridge: McGraw-Hill Education, 1988.

[50] Y. Oishi, R. S. Situmorang, R. A. Semibiring, H. Kawai and H. Ambarita, “Performance, rate of heat release, and combustion stability of dual-fuel mode in a small diesel engine,” *Energy Science & Engineering,* vol. 7, no. 4, pp. 1333-1351, 2019.

[51] M. Karczewski, G. Szamrej and J. Chojnowski, “Experimental Assessment of the Impact of Replacing Diesel Fuel with CNG on the Concentration of Harmful Substances in Exhaust Gases in a Dual Fuel Diesel Engine,” *Energies,* vol. 15, 2022.

[52] A. M. Namasivayam, R. J. Crookes and T. Korakianitis, *Combustion Characterisitcs of Dual-Fuel Diesel Engine Using Emulsified Bio-Fuel for Pilot Ignition,* Warrendale, US: SAE Technical Paper 2009-01-0490, 2009.

[53] S. Binjuwair and A. Alkudsi, “The effects of varying spark timing on the performance and emission characteristics of a gaosline enigne: A study on Saudi Arabian RON91 and RON95,” *Fuel,* vol. 180, pp. 558-564, 2016.

[54] W. Shi, X. Yu, H. Zhang and H. Li, “Effect of spark timing on combustion and emissions of a hydrogen direct injection stratified gasoline engine,” *International Journal of Hydrogen Energy,* vol. 42, no. 8, pp. 5619-5626, 2017.

[55] J. Zareei and A. Kakaee, “Study and the effects of ignition timing on gasoline engine performance and emissions,” *European Transport Research Review,* vol. 5, no. 2, pp. 109-116, 2013.

[56] L. Tunka and A. Polcar, “Effect of Various Ignition Timings on Combustion Process and Performance of Gasoline Engine,” *Acta Universitatis Agriculturae et Silviculturae Mendelianae Brunensis,* vol. 65, no. 2, pp. 545-554, 2017.

[57] H. Hailin and G. A. Kharim, “Hydrogen Fueled Spark-Ignition Engines Predictive and Experimental Performance,” *Journal of Engineering for Gas Turbines and Power,* vol. 128, no. 1, pp. 230-236, 2006.

[58] S. T. P. Purayil, S. A. B. Al-Omari and E. Elnajjar, “Experimental investigation of spark timing on extension of hydrogen knock limit and performance of a hydrogen-gasoline dual-fuel engine,” *International Journal of Hydrogen Energy,* vol. 49, pp. 910-922, 2024.

[59] S. Molina, R. Novella, J. G. Soriano and M. O. Girona, “Experimental Activities on a Hydrogen-Fueled Spark-Ignition Engine for Light-Duty Applications,” *Energies,* vol. 14, no. 20, 2021.

[60] D. Rrustemi, L. Ganippa and C. Axon, “Investigation of boost pressure and spark timing on combustion and NO emissions under lean mixture operation in hydrogen engines,” *Fuel,* vol. 353, 2023.

[61] P. Sementa, J. Vargas Antolini, C. Tornatore, F. Catapano, B. M. Vaglieco and ,. J. L. J. Sanchez, “Exploring the potentials of lean-burn hydrogen SI engine compared to methane operation,” *International Journal of Hydrogen Energy,* vol. 47, pp. 25044-25056, 2022.

[62] J. Demuynck, M. D. Paepe, I. Verhaert and S. Verhelst, “Heat Loss Comparison Between Hydrogen, Methane, Gasoline and Methanol in a Spark-Ignition Internal Combustion Engine,” *Energia Procedia,* vol. 29, pp. 138-146, 2012.

[63] H. Lindqvist and P. Overby, *A Literature Review of Hydrogen Internal Combustion Engines,* Gothenburg, Sweden: Chalmers University of Technology, 2024.

[64] M. S. Al-Baghdadi, “Effect of compression ratio, equivalence ratio and engine speed on the performance and emission characteristics of a spark ignition engine using hydrogen as a fuel,” *Renewable Energy,* vol. 29, no. 15, pp. 2245-2260, 2004.

[65] S. Verma, “Spark Advance Modelling of Hydrogen-Fuelled Spark Ignition Engines using Combustion Descriptors,” *Journal of Engineering for Gas Turbines and Power,* vol. 140, no. 8, 2018.

[66] B. A. Ceper, “Experimental investigation of the effect of spark plug gap on a hydrogen fueled SI engine,” *International Journal of Hydrogen,* vol. 37, no. 22, pp. 17310-17320, 2012.

[67] Denso, “Spark Plug Catalog,” Denso, 2022.

[68] J. K. Unni, P. Govindappa and L. M. Das, "Development of hydrogen fuelled transport engine and field tests on vehicles," *International Journal of Hydrogen Energy,* vol. 42, no. 1, pp. 643-651, 2017.

[69] N. Negurescu, C. Pana and A. Cernat, "Aspects of using hydrogen in SI engine," *Scientific Bulletin of the Politehnica University of Bucharest,* vol. 74, no. 1, pp. 11-20, 2012.

[70] H. Aljabri, M. Silva, M. B. Houidi, X. Liu, M. Allehaibi, F. Almatrafi, A. R. AlRamadan, B. Mohan and E. I. H. G. Cenker, "Comparative Study of Spark-Ignited and Pre-Chamber Hydrogen-Fueled Engine: A Computational Approach," *energies,* vol. 15, no. 23, 2022.

[71] A. Taha, T. A. Salam and M. Vellakal, "Alternative Fuels for Internal Combustion Engines: An Overview of the Current Research," *Journal of Engineering and Applied Sciences,* 2013.

[72] E. Pipitone and A. Beccari, "Determination of TDC In Internal Combustion Engines By A Newly Developed Thermodynamic Approach," *Applied Thermal Engineering,* vol. 30, no. 14-15, pp. 1914-1926, 2010.

[73] C. Caruana, *In-Cylinder Heat Transfer and Friction Analysis In Pressurised Motored Compression Ignition Engine,* PhD dissertation, Malta: University of Malta, 2020.

[74] R. Rahmani, N. Dolatabadi and H. Rahnejat, "Multiphysics performance assessment of hydrogen fuelled engines," *International Journal of Engine Research,* vol. 24, no. 9, 2023.

[75] O. I. M. Nwafor, “Knock characteristics of dual-fuel combustion in diesel engines using natural gas as primary fuel,” *Sādhanā – Academy Proceedings in Engineering Sciences,* vol. 27, no. 3, pp. 375-382, 2002.

[76] M. M. Syrimis and D. N. Assanis, “Knocking Cylinder Pressure Data Characterisitcs in a Spark-Ignition Engine,” *Journal of Engineering for Gas Turbines and Power,* vol. 125, no. 2, pp. 494-499, 2003.

[77] A. Żółtowski, “Knock Combustion in Dual Fuel Diesel Engine,” *Journal of KONES Powertrain and Transport,* vol. 21, no. 4, pp. 547-553, 2014.

[78] J. R. Encinar and M. Moldovan, “Lead,” *Encyclopedia of Analytical Science,* pp. 56-63, 2005.

[79] Federal Aviation Administration, “Leaded Aviation Fuel and the Environment,” Wedensday November 2019. [Online]. Available: https://www.faa.gov/newsroom/leaded-aviation-fuel-and-environment. [Accessed 23 August 2025].

[80] Y. Zhuang, Y. Qian and G. Hong, “The effect of ethanol direct injection on knock mitigation in a gasoline port injection engine,” *Fuel,* vol. 210, pp. 187-197, 2017.

[81] A. T. Alisaraei and A. R. Asl, “The effect of added ethanol to diesel fuel on performance, vibration, combustion and knocking of a CI engine,” *Fuel,* vol. 185, pp. 718-733, 2016.

[82] E. Kasseris and J. B. Heywood, *Charge Cooling Effects on Knock Limits in SI DI Engines Using Gasoline/Ethanol Blends: Part 2-Effective Octane Numbers,* vol. 5, SAE Technical Paper 2012-01-1284, 2012.

[83] T. Yao and W. Pan, “The impact of intake air temperature on performance and exhaust emissions of a diesel methanol dual fuel engine,” *Fuel,* vol. 162, pp. 101-110, 2015.

[84] R. L. McCormick and R. Parish, “Advanced Petroleum Based Fuels Program and Renewable Diesel Program,” National Renewable Energy Laboratory, Colorado, US, 2001.

[85] H. Arruga, “Effect of intake manifold water injection on a natural gas spark ignition engine: an experimental study,” in *Materials Science and Engineering*, 2017.

[86] T. Lakshmanan, N. Govindan and A. K. Ahmed, “Effect of Water Injection in Acetylene-Diesel Dual Fuel DI Diesel engine,” in *ASME 2012 Internal Combustion Engine Division Fall Technical Conference*, Vancouver, Canada, 2012.

[87] H. O. Ghazal, “Combustion analysis of hydrogen-diesel dual fuel engine with water injection technique,” *Case Studies in Thermal Engineering,* vol. 13, 2019.

[88] R. Adnan, H. H. Masjuki and T. M. I. Mahlia, “Performance and emission analysis of hydrogen fueled compression ignition engine with variable water injection timing,” *Energy,* vol. 43, no. 1, pp. 416-426, 2012.

[89] S. Portelli, *Setting up of a Hydrogen Spark Ignition Engine with In-cylinder Pressure Measurement for Combustion Characterisation, M.Sc Dissertation,* Malta: University of Malta, 2022.

[90] A. Fenech, “Improvements of the Hydrogen Engine Setup and Continuation of the Experimental Investigation, B.Eng dissertation,” University of Malta, Malta, 2024.

[91] A. J. Azzopardi, *Investigation of Boosting and Knock on Dual Fuel, LPG-Diesel Engines, M.Sc Dissertation,* Malta: University of Malta, 2025.

[92] T. Scicluna, *Investigating AdBlue as both an Emissions Reductant and Combustion Stabiliser in Dual-Fuel C.I. Engines, M.Sc Dissertation,* Malta: University of Malta, 2025.

[93] WÄRTSILÄ, "World's first ethane-powered marine vessels," [Online]. Available: https://www.wartsila.com/insights/article/worlds-first-ethane-powered-marine-vessels.

[94] ElectroGas Malta, "About Delimara Power Plant," [Online]. Available: https://www.electrogas.com.mt/about-delimara-power-plant/. [Accessed 15 August 2025].

[95] R. Procházka, A. Dittrich, T. Zvolský and D. Nguyen Phu, "The Knocking in the Gas Dual-fuel Engine with Liquid LPG Injection into the Intake Manifold," *International Journal of Mechanical Engineering and Robotics Research ,* vol. 10, no. 12, 2021.

[96] R. Stone, Introduction To Internal Combustion Engines, Hampshire: Palgrave Macmillan, 2012.

[97] D. R. Rogers, Engine Combustion: Pressure Measurement and Analysis, Warrendale, US: SAE International R-514, 2021.

[98] M. Farrugia, *MEC 4011 Powerplant Module Notes, Internal Combustion,* Malta.

[99] AVL, AVL Engine Indicating Handbook, Graz, Austria: AVL, 2002.

[100] T. W. Jet, *A Study of the Ignition Delay Characteristics of Combustion in a Compression Ignition Engine Operating on Blended Mixtures of Diesel and Gasoline B.Eng Dissertation,* Nottingham: The University of Nottingham, 2016.

[101] E. Obert, *Internal Combustion Engines third edition,* Pennsylvania: International Textbook Company, 1968.

[102] G. M. Rassweiler and L. Withrow, *Motion Picturesof Engine Flames Correlated with Pressure Cards,* vol. 42, SAE Technical Paper 380139, 1938, pp. 185-204.

[103] M. Mittal, G. Zhu and H. Schock, "Fast mass fraction burned calculation using the net pressure method for real-time applications," *Journal of Automobile Engineering ,* vol. 223, no. 4, pp. 389-394, 2009.

[104] A. F. Matekunas, *Modes and Measures of Cylic Variability,* Warrandale US: SAE Technical Paper 830337, 1983.

[105] A. Douaud, G. de Soete and C. Henault, *Experimental Analysis of the Initiation and Development of Part-Load Combustions in Spark-Ignition Engines,* Warrandale, US: SAE Technical Paper 830338, 1983.

[106] C. Clark and B. Challen, *Examining High Speed Data during Engine Transients,* Warrandale, US: SAE Technical Paper 850402, 1985.

[107] A. Beccari, S. Beccari and E. Pipitone, "An Analytical Approach for the Evaluation of the Optimal Combustion Phase in Spark Ignition Engines," *Journal of Engineering for Gas Turbines and Power,* vol. 132, no. 3, 2018.

[108] W. M. Wiseman, *Spark Ignition Engine Combustion Process Analysis, B.Sc Dissertation,* Nottingham: University of Nottingham, 1990.

[109] H. Bayraktar and O. Durgun, “Development of an empirical correlation for combustion durations in spark ignition engines,” *Energy Conversion and Management,* vol. 45, pp. 1419-1431, 2004.

[110] T. Yamamoto, K. Hiraoko, N. Mori, Y. Oda, A. Yuuki and K. Isono, “Engine Transient Characteristics Simulation Technology using Zero-dimensional Combustion Model,” *Mitsubishi Heavy Industries Technical Review,* vol. 53, no. 3, 2016.

[111] R. Rezaei, P. Eckert, S. Joern and K. Behnk, *Zero-Dimensional Modeling of Combustion and Heat Release Rate in DI Diesel Engines,* Sae Technical Paper 2012-01-1065, 2012.

[112] V. Hariram and R. Bharathwaaj, “Application of zero-dimensional thermodynamic model for predicting combustion parameters of CI engine fuelled with biodiesel-diesel blends,” *Alexandria Engineering Journal,* vol. 55, no. 4, pp. 3345-3354, 2016.

[113] C. W. Vigild, *The Internal Combustion Engine Modelling, Modelling, Estimation and Control Issues, Ph.D Dissertation,* Lyngdby: Technical University of Denmark, 2002.

[114] R. W. Schefer, C. White and J. Keller, “Lean Hydrogen Combustion,” *Lean Combustion Technology and Control,* vol. 8, pp. 213-254, 2008.

[115] J.A.P, “J.A.P Industrial Engines General Description,” [Online]. Available: https://oldlawnmowerclub.co.uk/sites/default/files/opmanual/JAP%20Model%204-5-6%20Type%201.pdf. [Accessed 20 July 2025].

[116] E. Ower and R. C. Pankhurst, The measurement of air flow, Oxford: Pergamon Press, 1977.

[117] E. Rathakrishnan, Instrumentation, Measurements and Experiments in Fluids, Boca Raton: CRC Press, 2017.

[118] F. Laurantzon, *Flow measuring Techniques in Steady and pulsating compressible Flows, Ph.d dissertation,* Stockholm: University of Stockholm, 2010.

[119] L. J. Kastner, T. Williams and R. Sowden, "Critical-Flow Nozzle Meter and its Application to the Measurement of Mass Flow rate in Steady and Pulsating Streams of Gas," *Journal of Mechnical Engineering Science,* vol. 6, no. 1, pp. 88-98, 1964.

[120] A. Martyr and M. Plint, *Engine Testing Theory and Practise,* Oxford: Elsevier Ltd., 2007.

[121] International Organization for Standardization, *Measurement of fluid flow by means of pressure differential devices inserted in circular-cross section conduits running full-Nozzles and Venturi nozzles ISO 5167-3,* Switzerland: ISO, 2003.

[122] J. Krishnanunni, D. Bhatia and L. M. Das, "Experimental and modelling investigations on the performance and emission characteristics of a single cylinder hydrogen engine," *International Journal of Hydrogen Energy,* vol. 42, pp. 29574-29584, 2017.

[123] S. Chen and P. Flynn, *Development of a Single Cylinder Compression Ignition Research Engine,* SAE Technical Paper 650733, 1965.

[124] C. Caruana, M. Farrugia, G. Sammut and E. Pipitone, "One-dimensional simulation of the pressurized motoring method: friction, blow-by, temperatures

and heat transfer analysis," in *International combustion engines and powertrain systems for future transport*, Birmingham , 2022.

[125] Ricardo, *WAVE User Manual,* Ricardo, 2017.

[126] National Institute of Standards and Technology , *NIST Chemistry WebBook,* United States: NIST, 1991.

[127] S. Mifsud, *LPG Dual-Fuel Implementation and Simulation on a Common Rail Diesel Engine B.Eng Dissertation,* Malta: Univeristy of Malta, 2020.

[128] M. Schembri, *Experimental Investigation of the Combustion Behaviour and NOx Emissions of LPG-Diesel, Dual-Fuel, Engine B.Eng Dissertation,* Malta: University of Malta, 2022.

[129] M. Schembri, *Experimental Investigation of the Combustion Behaviour and NOx Emissions of LPG-Diesel, Dual-Fuel, Engine, M.Sc Dissertation,* Malta: University of Malta, 2022.

[130] T. Castiglione, L. Falbo, D. Perrone and S. Bova, "Cooling on-demand for knock prevention in spark-ignition engines: An experimental analysis," *Applied Thermal Engineering,* vol. 195, 2021.

[131] D. E, "Materials for Cryogenic Applications," in *Applied Mechanics and Materials Engineering*, Valcea, 2003.

[132] E. G. Kendall, "Metals and Alloys for Cryogenic Applications - A Review (SSR-63-371)," Materials Sciences Labratory, Aerospace Corporation, California, 1964.

[133] F. M. White, Fluid Mechanics, New York: McGraw-Hill Education, 2011.

[134] J. P. Azzopardi, J. P. Farrugia, C. Caruana, N. Grech, N. Farrugia, M. Chircop and M. Farrugia, *Testing and Implementation of a Turbocharged Formula SAE Vehicle,* SAE Technical Paper 2018-01-0967, 2018.

[135] M. Farrugia and A. Briffa, *Liquid State LPG Conversion of an Older Vehicle,* SAE Technical Paper 2014-01-2613, 2014.

[136] M. Farrugia, A. Briffa, A. T. Saliba and A. Fenech, "Liquefied Petroleum Gas (LPG) Transferring Unit," in *Word Conference on Sustainability, Energy and Envirionment*, Prague, 2025.

[137] G. T. Hashem, A.-D. Mohamed and J. Sarris, "The characteristics of gasoline engines with the use of LPG: An experimental and numerical study," *International Journal of Thermofluids,* vol. 56, 2023.

[138] F. Ma, W. Yang, J. Xu, Y. Li, Z. Zhao, Z. Zhang and Y. Wang, "Experimental Investigation of Combustion Characteristics on Opposed Piston Two-Stroke Gasoline Direct Injection Engine," *Energies,* vol. 14, 2021.

[139] T. Eastop and A. McConkey, *Applied Thermodynamics for Engineering Technologists fifth Edition,* Delhi: Dorling Kindersley, 2009.

[140] S. Hires, R. Tabaczynski and J. Novak, *The Prediction of Ignition Delay and Combustion Intervals for a Homogeneous Carge, Spark Ignition Engine,* SAE Technical Paper 780232, 1978.

[141] National Research Council, Verifying Greenhouse Gas Emissions: Methods to Support International Climate Agreements, Washington, DC: The National Academies Press, 2010.

[142] M. wild, A. Ohmura and K. Makowski, “Geophysical Research Abstracts,” *Impact of global dimming and brightening on global warming,* vol. 34, no. 4, p. 4, 2007.

[143] S. Pfoser, G. Aschauer, L. Simmer and O. Schauer, “Facilitating the implementation of LNG as an alternative fuel technology in landlocked Europe; A study from Austra,” *Research inTransportation Business and Management,* vol. 18, pp. 77-84, 2016.

[144] J. Winter, S. Dobson, K. Fellows, D. Lam and P. Craig, “An overview of global liquefied natural gas markets and implications for Canada,” Oxford Institute for Energy Studies, Oxford, 2019.

[145] B. Merci, E. Mastorakos and A. Mura, “Modelling of Turbulent Combustion,” *Handbook of Combustion,* vol. 1, pp. 175-203, 2010.

[146] A. Arora and A. Bachle, “Storage of Natural Gas by Adsorption Process,” in *SPE/IATMI Asia Pacific Oil & Gas Conference and Exhibition*, Bali, Indonesia, 2015.

[147] J. Rouquerol, F. Rouquerol, P. M. G. M. Llewellyn and K. Sing, Adsorbtion by Powders and Porous Solids, Oxford: Academic Press, 2014.

[148] E. Mattarelli, C. A. Rinaldini and V. I. Golovitchev, “CFD-3D analysis of a light duty Dual Fuel (Diesel/Natural Gas) combustion engine,” *Italian Journal of Engineering Science,* vol. 63, no. 2-4, pp. 381-385, 2019.

[149] G. A. Karim, “Combustion in Gas-fueled Compression Ignition Engines of the Dual Fuel Type,” *Handbook of Combustion,* vol. 3, no. 6, 2015.

[150] H. S. Hosseini, A. Tsolakis, A. Alagumalai, O. Mahian, S. S. Lam, J. Pan, W. Peng, M. Tabatabaei and M. Aghbashlo, “Use of hydrogen in dual-fuel diesel engines,” *Progress in Energy in dual-fuel diesel enignes,* vol. 98, 2023.

[151] C. Sui, P. de Vos, D. Stapersma, K. Visser and Y. Ding, “Fuel Consumption and Emissions of Ocean-Going Cargo Ship with Hybrid Propulsion and Different Fuels over Voyage,” *Journal of Marine Science and Engineering,* vol. 8, no. 8, 2020.

[152] A. T. Saliba, E. Agius, K. Scerri and M. Farrugia, “Simulation of operation and control of LNG and diesel dual fuel engine for marine application,” in *Offshore Energy & Storage Symposium*, Malta, 2023.

Chapter 10. Appendix

The Tables in this chapter contain all the values obtained both from the slow and fast data values presented in all the figures in Chapter 6. Additionally, for each parameter the corresponding COV values are presented. It is important to note that the MBT spark timing, CA10, CA50 and CA90 values are presented with reference to After Bottom Dead Centre (ABDC).

Table 10-1: The mean and COV values of slow and fast data collected during the petrol fuel tests.

Petrol																		
Load	**Statistical Parameter**	**MBT Spark Timing (CA ABDC)**	**Measured Torque (Nm)**	**Peak Work (J/cycle)**	**Brake Thermal Efficiency (%)**	**Peak In-cylinder Pressure (bar)**	**Peak Net HRR (J/CA)**	**Cumulative Net HRR (J/cycle)**	**CA10 (CA ABDC)**	**CA50 (CA ABDC)**	**CA90 (CA ABDC)**	**Fast Burn Duration (CA)**	**Ignition Delay (CA)**	**Energy Losses Eq. (3.8) (J/cycle)**	**Energy Losses Eq. (3.9) (J/cycle)**	**Peak Blow-by Gases (g/s)**	**Peak Mass Fraction Burned (3.16)**	**Energy Lost Ratio**
50kPa	**Mean**	155	8.3	154.4	15	11.7	22.1	458.5	180.3	190.6	218.1	37.8	8.1	263.0	208.9	0.32	0.67	0.31
	COV (%)	0.001	0.8	1.3	1.2	3.7	8.7	1.0	1.2	1.3	1.3	8	19.7	1.6	2.2	3.2	1.0	2.2
75kPa	**Mean**	160	18.9	302.0	20.3	19.8	44.2	757.6	179.5	187.7	211.6	40.3	3.5	376.1	326.9	0.53	0.71	0.29
	COV (%)	0.001	0.4	0.6	0.7	0.8	8.0	0.7	1.1	0.7	1.1	7.4	14.4	1.6	1.5	1.7	0.7	1.5
95kPa	**Mean**	160	26	403.9	20.7	25.1	57.9	972.8	178.6	186.8	212.1	41.1	3.7	471.8	487.0	0.66	0.69	0.32
	COV (%)	0.01	2.3	0.6	2.4	1.8	7.7	0.7	0.9	0.7	0.8	5.8	12.5	7.5	1.3	1.5	0.7	1.3

Table 10-2: The mean and COV values of slow and fast data collected during the propane fuel tests.

Propane																		
Load	**Statistical Parameter**	**MBT Spark Timing (CA ABDC)**	**Measured Torque (Nm)**	**Work (J)**	**Brake Thermal Efficiency (%)**	**Peak In-cylinder Pressure (bar)**	**Peak Net HRR (J/CA)**	**Cumulative Net HRR (J/cycle)**	**CA10 (CA ABDC)**	**CA50 (CA ABDC)**	**CA90 (CA ABDC)**	**Fast Burn Duration (CA)**	**Ignition Delay (CA)**	**Energy Losses Eq. (3.8) (J/cycle)**	**Energy Losses Eq. (3.9) (J/cycle)**	**Peak Blow-by Gases (g/s)**	**Peak Mass Fraction Burned (3.16)**	**Energy Lost Ratio**
50kPa	**Mean**	155	6.0	118.4	10.6	9.4	16.3	394.8	182.5	194.2	218.1	34.3	10.7	411.5	316.3	0.28	0.64	0.44
	COV (%)	2.1	1.9	16.3	2.6	15.6	21.4	7.7	2.8	3.8	5.7	31.6	34.7	2.4	9.6	10.7	7.7	9.6
75kPa	**Mean**	160	16.7	273.2	17.8	17.9	36.5	693.7	179.8	189.2	214.6	34.8	5.0	481.6	461.8	0.51	0.61	0.39
	COV (%)	2.1	0.9	3.5	0.5	5.9	14.1	2.9	1.2	1.3	3.0	19.6	39.1	2.2	4.3	5.2	2.9	4.3
95kPa	**Mean**	160	24.4	384.5	20.5	24.3	50.0	926.2	177.2	186.0	212	34.8	3.8	549.2	540.5	0.65	0.56	0.36
	COV (%)	0.6	2.3	1.6	1.5	3.1	10.2	1.7	0.9	0.9	2.7	17.7	24.8	2.5	2.9	2.6	1.7	2.9

Table 10-3: The mean and COV values of slow and fast data collected during the H2 λ2 fuel tests.

H_2 λ2																		
Load	**Statistical Parameter**	**MBT Spark Timing (CA ABDC)**	**Measured Torque (Nm)**	**Work (J)**	**Brake Thermal Efficiency (%)**	**Peak In-cylinder Pressure (bar)**	**Peak Net HRR (J/CA)**	**Cumulative Net HRR (J/cycle)**	**CA10 (CA ABDC)**	**CA50 (CA ABDC)**	**CA90 (CA ABDC)**	**Fast Burn Duration (CA)**	**Ignition Delay (CA)**	**Energy Losses Eq. (3.8) (J/cycle)**	**Energy Losses Eq. (3.9) (J/cycle)**	**Peak Blow-by Gases (g/s)**	**Peak Mass Fraction Burned (3.16)**	**Energy Lost Ratio**
75kPa	**Mean**	170	8.8	145.1	17.8	13.8	29.4	397.7	179.9	186.3	203.8	28.6	1.9	161.3	120.7	0.44	0.75	0.23
	COV (%)	0.08	0.8	1.7	1.9	2.3	8.5	2.0	0.08	1.0	3.1	22.6	50.5	4.4	4.5	1.7	2.0	4.5
95kPa	**Mean**	170	12.4	207.5	21.7	18.1	40.0	522.3	179.1	185.5	207.0	28.5	1.4	198.6	162.6	0.57	0.76	0.23
	COV (%)	2.4	7.4	1.7	3.5	4.7	6.9	1.4	0.08	0.4	1.0	11.6	56.7	14.5	4.4	1.7	1.4	4.4
120kPa	**Mean**	170	20.6	307.0	25.4	22.3	52.1	697.6	184.8	190.3	208.4	24.8	1.0	235.8	235.5	0.69	0.77	0.24
	COV (%)	0.01	2.3	1.2	2.9	3.0	7.1	1.0	1.6	3.0	0.6	5.5	55.3	6.7	3.4	5.4	1.0	3.4

Table 10-4: The mean and COV values of slow and fast data collected during the H2 λ3 fuel tests.

H_2 λ3																		
Load	**Statistical Parameter**	**MBT Spark Timing (CA ABDC)**	**Measured Torque (Nm)**	**Work (J)**	**Brake Thermal Efficiency (%)**	**Peak In-cylinder Pressure (bar)**	**Peak Net HRR (J/CA)**	**Cumulative Net HRR (J/cycle)**	**CA10 (CA ABDC)**	**CA50 (CA ABDC)**	**CA90 (CA ABDC)**	**Fast Burn Duration (CA)**	**Ignition Delay (CA)**	**Energy Losses Eq. (3.8) (J/cycle)**	**Energy Losses Eq. (3.9) (J/cycle)**	**Peak Blow-by Gases (g/s)**	**Peak Mass Fraction Burned (3.16)**	**Energy Lost Ratio**
75kPa	**Mean**	160	6.7	107.0	15.3	11.2	13.3	311.4	178.8	190	214	31.7	3.9	106.3	68.8	0.39	0.82	0.18
	COV (%)	0.01	2.9	8.3	4.6	4.7	13.9	6.2	0.2	4.1	1.5	30.4	64.0	5.4	19.8	2.6	6.2	19.8
95kPa	**Mean**	170	10.0	171.8	22.7	14.3	23.4	457.7	184.8	194.3	216.3	33.9	3.3	98.6	72.2	0.50	0.84	0.13
	COV (%)	0.05	1.3	5.1	1.9	6.2	10.5	4.4	1.6	1.8	1.3	28.9	28.5	7.2	27.8	6.9	4.3	27.8
120kPa	**Mean**	170	15.6	254.3	26.1	18.0	30.7	626.5	186.4	196.6	213.7	29.8	3.7	124.1	179.9	0.61	0.82	0.22
	COV (%)	0.08	0.7	2.5	2.5	5.4	8.2	2.2	1.2	1.4	1.3	11.7	17.1	10.0	7.7	6.8	2.2	7.7